UNIVERSITY OF CALIFORNIA SAN DIEGO

What makes an Atmospheric River dusty? Spatio-temporal characteristics and drivers of dust in the vicinity of Atmospheric Rivers along the U.S. west coast

A dissertation submitted in partial satisfaction of the
requirements for the degree
Doctor of Philosophy

in

Oceanography

by

Kara Voss

Committee in charge:

Amato Evan, Chair
Jennifer Burney
Mark Jacobsen
Mark Merrifield
Martin Ralph
Katherine Ricke

2020

The dissertation of Kara Voss is approved, and it is acceptable in quality and form for publication on microfilm and electronically:

_____

_____

_____

_____

_____

_____
Chair

University of California San Diego

2020

TABLE OF CONTENTS

LIST OF FIGURES

LIST OF TABLES

ACKNOWLEDGEMENTS

I am incredibly grateful for the multitudes of people who have supported me throughout this endeavour.

I would like to express my deepest gratitude to my family for their comfort and guidance. I'm grateful to my parents, Ken Voss and Kay Kilpatrick, for fostering my curiosity for the natural world and to my brother, Nick Voss, for commiserating on the difficulties of graduate school. I'm thankful for the loving support of my fiance, Dan Flanigan, and his intuition for when to make me set my laptop aside and take a trip to the mountains.

I owe a great deal of thanks to the mentors I have had prior to and during my Ph.D. work. My sincerest gratitude goes to my Ph.D. advisor Amato Evan, not only for his consult on my science, but for consistently advocating for me. I would like to express my deepest gratitude to Paty Matrai, who has provided infinite support and mentorship in so many forms and so many stages of my life. I would like to thank Marty Ralph for his consult on science and on my career, and for providing so many unique opportunities to see how science informs policy and engage in the process. I'm grateful to Jennifer Burney and Katherine Ricke, for their support as committee members, collaborators, and advisors within the GPS Science Policy Fellows Program. I'm grateful to Mark Merrifield and Peter Franks for their advice during some of my most challenging times in graduate school, and to Mark Jacobsen for supporting me as a thesis committee member. I'm also very grateful to Kimberly Prather for her support during my first two years of this Ph.D. program.

I could not have completed this program without the incredible network of friends within and outside of San Diego who consistently have supported me. I'm also so grateful to all of the students, post-docs, staff, and faculty in the Center for Western Weather and Water Extremes who I've relied upon in so many ways.

Chapter 2, in full, is a reprint of the material as it appears in Journal of Applied Meteorology and Climatology. Kara K. Voss and Amato T. Evan, (2020). A new satellite-based global climatology of dust aerosol optical depth, Journal of Applied Meteorology and Climatology, doi:10.1175/JAMC-D-19-0194.1. The dissertation

author was the primary author of this paper.

Chapter 3, in full, is a reprint of the material as it was submitted to Journal of Climate. K. K. Voss, A. T. Evan, K. A. Prather, F. M. Ralph, (In Press). Dusty Atmospheric Rivers: Characteristics and Origins, Journal of Climate. The dissertation author was the primary author of this paper.

Chapter 4, in part is currently being prepared for submission for publication of the material. K. K. Voss; A. T. Evan; F. M. Ralph. The dissertation author was the primary investigator and author of this material.

VITA

2015	B. S. in Atmospheric and Oceanic Science, University of Miami, Rosenstiel School of Marine and Atmospheric Science
2017	M. S. in Oceanography, University of California, San Diego
2020	Ph. D. in Oceanography, University of California, San Diego

PUBLICATIONS

Voss & Evan, "A new satellite-based global climatology of dust optical depth", *J. Applied Meteorology and Climatology*, X, 2019.

Voss, K. K; Evan, A. T.; Prather, K. A.; Ralph, M. F.; "Dusty Atmospheric Rivers: Characteristics and Origins", *In Review, J. Clim*

ABSTRACT OF THE DISSERTATION

What makes an Atmospheric River dusty? Spatio-temporal characteristics and drivers of dust in the vicinity of Atmospheric Rivers along the U.S. west coast

by

Kara Voss
Doctor of Philosophy in Oceanography
University of California San Diego, 2020
Amato Evan, Chair

Trans-Pacific dust is thought to increase precipitation from atmospheric rivers (ARs) by enhancing ice formation in mixed-phase clouds. However, constraints on measurements of dust have limited our understanding of the magnitude of this effect.

In this dissertation, we utilize satellite-retrievals, ground-based observations, and reanalysis to: 1. Develop global, daily, observation-based datasets of dust aerosol optical depth extending from 2001 through 2018, 2. Develop a dust score to characterize the dust-content of the environment surrounding ARs that made landfall along the U.S. west coast between 2001 and 2018 and characterize the year-to-year variability of the dust content of the surroundings of ARs, and 3. Analyze the meteorological conditions associated with the presence of dust in the vicinity of ARs. We show that dusty ARs occur primarily in March, at the confluence of the end of the AR season and the beginning of the trans-Pacific dust season. We show that dust is preferentially found within the warm sector of the extra-tropical cyclones associated with ARs making landfall along the U.S. but dust is also enhanced in the cold sector. Our results suggest that the year-to-year variability in the dust score is primarily the result of variability of the dust content of the eastern North Pacific and correlated variability of the frequency of ARs and

the dust content of surrounding area. Finally, we investigate the meteorological conditions that lead to the presence of dust in the vicinity of an AR by analyzing the conditions over trans-Pacific dust source regions and over the North Pacific in the days prior to an AR. Dusty ARs are associated with enhanced upper- and mid-level westerly winds over Asia, an extended North Pacific Jet, and eastward migrating extra-tropical cyclones. In contrast, pristine ARs are associated with a persistent ridge over the North Pacific.

The research presented here addresses gaps in our understanding of how often and why dust is present in the vicinity of an AR, a critical step in constraining the influence of dust on precipitation from ARs.

Chapter 1

Introduction

Mineral dust aerosols are ubiquitous in the earth's atmosphere (Textor et al., 2006), and can be transported thousands of miles from source regions, remaining lofted for weeks at a time (Prospero, 1999; Duce et al., 1980; Uematsu et al., 1983). Dust has the ability to impact weather by interacting with short-wave and long-wave radiation (Miller and Tegen, 1998) or by altering the micro-physical properties of clouds (Twomey, 1977). Scattering or absorbing solar radiation and absorbing and emitting outgoing long-wave radiation allows dust to change the temperature structure of the atmosphere (Miller and Tegen, 1998).

The indirect effects of dust on weather and climate generally refer to the complex interactions between dust and clouds. These effects are particularly dependent on the temperature, pressure, and humidity of the surrounding atmosphere. Under saturated conditions, dust is known to act as an ice nucleating particle (INP), forming ice at temperatures well above the homogeneous freezing point (Isono et al., 1959; DeMott et al., 2003). As ice crystals grow much more efficiently than liquid droplets, due to the low vapor pressure surrounding the crystalline surface and through riming, they are quicker to overcome updrafts to produce precipitation (Hosler et al., 1957; Pinsky et al., 1998; Korolev, 2007). For this reason, it is hypothesized that small amounts of dust may enhance precipitation under cold, saturated conditions. Precipitation residues from in-flight measurements over the Sierra Nevada Mountain Range and precipitation residues collected during the CalWater field campaigns support this link between the presence of dust in clouds

and enhancement of precipitation (Ault et al., 2011; Creamean et al., 2013, 2016; Fan et al., 2014). In contrast, in shallow, low clouds that are warmer than the temperature for INP activation, case studies have found that dust acts as cloud condensation nuclei and can decrease precipitation by reducing water droplet effective radius, therefore increasing the persistence of this cloud type (Rosenfeld et al., 2001; Kaufman et al., 2005). As clouds are a major component in the Earth's radiative balance, dust then indirectly impacts global temperature through the same mechanisms (Twomey, 1977).

Dust is also known to impact the development of tropical cyclones, again in ways that are dependent on the surrounding conditions. It is thought to inhibit tropical cyclone development off of Africa by enhancing atmospheric stability though direct radiative mechanisms that suppress deep convection (Evan et al., 2006; Dunion and Velden, 2004). However, some modeling experiments have shown that through release of latent heat of freezing when activated as INP, dust may actually intensify a hurricane and control its spatial structure in a process termed *convective invigoration* (Lynn et al., 2016).

It was not until the mid-2000s that researchers became interested in the impact of dust on storms impacting the west coast of North America called Atmospheric Rivers (ARs). ARs, defined in the American Meteorological Society glossary as "long, narrow, transient corridors of strong horizontal water vapor transport typically associated with a low-level jet stream ahead of the cold front of an extratropical cyclone" (Ralph et al., 2018), cause extreme precipitation in the western U.S. when forced upward by steep orography (Waliser and Guan, 2017). These ribbons of high wind speeds bring moisture from the tropics towards the mid-latitudes but can also transport moisture from other parts of the Pacific. The landfall position and orientation of an AR along the U.S. west coast is typically controlled by a dipole pattern of a trough and ridge to the north or south situated along the coast. These storms are responsible for a very large portion of water resources in the western U.S., up to 50% in California in most years (Dettinger et al., 2011), but are relatively infrequent with only a few events per year in a given location (Lamjiri et al., 2017). In addition to providing water resources ARs can lead to

damaging floods, particularly when soils are saturated prior to the AR landfall (Corringham et al., 2019).

Accurate forecasts of precipitation from ARs allow water managers the opportunity to anticipate flood risk or maximize water storage (Ralph et al., 2014). Despite case-based evidence that dust could increase precipitation from ARs by up to 40% (Ault et al., 2011), aerosol-cloud-precipitation interactions are, in general, not represented in operational numerical weather prediction models (Jiang et al., 2017). This is partially due to the high computational cost of representing small scale, highly complex interactions. It is also because our understanding of these interactions is limited and there are very few measurements to constrain parameterizations (Benedetti et al., 2018). These aerosol-cloud-precipitation interactions are a potential source of error in forecasts (Jiang et al., 2017), including forecasts of ARs. However, the lack of quantitative constraints on how much and how often aerosols are present and able to influence precipitation make the scale of these errors unknown.

Trans-Pacific dust, aeolian mineral dust from sources west of the Pacific Ocean that travels eastward towards North America, dominates over concentrations of local dust in many locations along the North American coast (Creamean et al., 2015; Yu et al., 2019). While it disperses as it travels across the Pacific Ocean such that it is greatly reduced in concentration if it reaches North America, it has the potential to change the micro-physical properties of clouds. Trans-Pacific dust was first identified within Atmospheric Rivers during the CalWater Field campaign (Ralph et al., 2016; Ault et al., 2011). In-flight and on-the ground measurements of aerosols during this campaign, in which measurements were taken from ARs that occurred during the cool season from 2011 to 2015, allowed for detailed case studies on aerosol composition and cloud micro-physical characteristics during ARs. In some of these cases, dust layers were found coincident with enhanced ice fraction (Creamean et al., 2013), suggesting ice nucleation, and when two meteorologically similar storms were compared it was found that the storm with dust produced up to 40% more precipitation (Ault et al., 2011).

While these studies suggest that dust may play a large role in modulating

precipitation from ARs, the temporally and spatially limited nature of aircraft and in-situ measurements makes it difficult to draw generalizable conclusions from these findings. These case studies utilized air mass back trajectory modeling to infer dust provenance and its transport path but they did not specifically analyze the meteorological drivers that led to the presence of dust in some storms, but not others.

A key step in understanding the extent to which dust influences precipitation from Atmospheric Rivers is understanding how often, and why, dust is present in and around these storms. In order to address this, a long record of dust is necessary. In Chapter II, a new, daily, satellite-based observational dataset of dust is introduced that is global, such that it may be used to investigate dust in the vicinity of ARs making landfall along the U.S. but also to investigate the source regions and transport path of this dust. In Chapter III, the dust dataset described in Chapter II is used to create a "dust score", a metric for characterizing the dust-content of the environment surrounding an AR, for ARs that made landfall along the U.S. west coast between 2001 and 2018. This dust score is then used to describe the annual cycle and year-to-year variability of high dust score ARs and to infer the characteristic location of dust within AR-associated extra-tropical cyclones. In Chapter IV, an evaluation of the synoptic meteorological conditions that lead to the presence of dust in the environment surrounding the AR is performed. The conclusions of this synoptic evaluation have implications for predictability and may be informative for future field observation-based investigation of dust-cloud-precipitation interactions under AR conditions.

Chapter 2

A new satellite-based global climatology of dust optical depth

2.1 Chapter Abstract

By mass, dust is the largest contributor to global aerosol burden. Yet long term observational records of dust, particularly over the ocean, are limited. Here, two nearly-global observational datasets of dust aerosol optical depth (τ_d) are created based primarily on optical measurements of the aerosol column from 1) the MODerate resolution Imaging Spectroradiometer (MODIS) aboard the Terra satellite spanning from 2001 to 2018 and 2) the Advanced Very High-Resolution Radiometer (AVHRR) from 1981 to 2018. The quality of the new data is assessed by comparison with existing dust datasets that are spatially more limited. Between 2001 and 2018, τ_d decreased over Asia, and increased significantly over the Sahara, Middle East, and parts of eastern Europe, with the largest increase found over the Aral Sea where emissive playa surfaces have been exposed. These daily, observational, and nearly-global records of dust will allow for improvement in understanding the role of dust in climate variability.

2.2 Introduction

Aeolian dust makes up the largest mass fraction of the global aerosol burden (Textor et al., 2006) and produces profound impacts on natural (Rosenfeld et al., 2001; Swap et al., 1992; Mahowald, 2011; Miller et al., 2004; Ault et al., 2011; Evan et al., 2006; Strong et al., 2018) and anthropological systems (Tong et al., 2017; Griffin, 2007; Shao, 2008; Mani and Pillai, 2010; Ai and Polenske, 2008; Brown, 2002). A major limiting factor in understanding the global distribution of dust, how it will change in the future, and its complex interactions with Earth's climate, is the limited availability of measurements especially over the ocean (Prospero and Mayol-Bracero, 2013). Airborne campaigns have provided measurements for select places and times (Ralph et al., 2016; Formenti, 2003; Chen et al., 2011; Formenti et al., 2008; Stith et al., 2009; Ryder et al., 2013; Klaver et al., 2011) and ground based networks have provided long term measurements for specific regions (Malm et al., 1994; Prospero and Nees, 1986; Prospero, 1999; Holben et al., 1998). Most satellite sensors do not isolate the dust contribution to aerosol optical depth (AOD) at the point of retrieval, so several methods have been proposed and utilized for studying spatial and temporal variations of dust using satellite measurements and models. These methods have mostly used optical properties of the aerosol column related to particle size (Ginoux et al., 2012; Kaufman, 2005), color, and single scattering albedo (Ginoux et al., 2012), or have used the Ultraviolet (UV) absorptive property of dust for identification (Ginoux, 2003). Several studies have used satellite-based products to study dust aerosol optical depth (τ_d) over either the ocean or land in select locations. Over the Atlantic Ocean, Kaufman (2005) analyzed τ_d using the MODerate Imaging Spectroradiometer (MODIS) retrievals of AOD and Evan and Mukhopadhyay (2010) used a similar method to create a record of τ_d based on retrievals by the Advanced Very High Resolution Radiometer (AVHRR). In addition, Ginoux et al. (2012) used τ_d over bright land surfaces based on MODIS Deep Blue AOD to identify dust source regions. Monthly τ_d has also been used in evaluation of the dust emission schemes of global climate models (Pu and Ginoux, 2018b).

More recently, studies have used a combination of satellite observations and

models to investigate the distribution of dust globally and trends in dust for select regions. Ridley et al. (2016) produced a long-term mean dataset of τ_d between 2004 and 2008 using AOD retrievals from multiple satellite platforms and dust estimates from several global models and Chin et al. (2014) used satellite AOD from several sensors alongside the Goddard Chemistry Aerosol Radiation and Transport (GOCART) model to investigate multi-decadal regional trends in aerosol species, including dust. These merged approaches have value in allowing for elucidation of aerosol sources and the ability to distinguish anthropogenic from natural dust. However, they are susceptible to model biases in dust emission and transport. Climate models display a large diversity in dust aerosol optical depth and dust emission, mostly underestimating dust emission from major sources, and do not consistently agree with observations (Evan et al., 2014; Huneeus et al., 2011; Pu and Ginoux, 2018a; Kok et al., 2017; Kok, 2010; Ryder et al., 2018). Therefore, it is valuable to have complimentary extensive observational records of dust for comparison.

Here, we expand on the work of Evan and Mukhopadhyay (2010) by using the extended record of satellite retrievals to produce two nearly-global τ_d datasets developed using MODIS (2001-2018) and AVHRR (1981-2017) at daily and monthly resolution, respectively, with the former dataset extended to cover both land and ocean regions. Although dust transport happens on a temporal scale of days to weeks, the previously mentioned efforts have focused on estimating monthly mean τ_d. This work provides the longest record of observed daily τ_d to date, at a temporal resolution suitable for analysis of daily transport events (daily) and $1^{\circ}x1^{\circ}$ spatial resolution.

In the next section we describe the data and methods used in the estimation of global τ_d and provide an estimation of the associated uncertainty. Our results in Section 3 include identification of climatological seasonal patterns in τ_d, a comparison of our τ_d estimates as derived from two different sensors, and a comparison of the MODIS-derrived dataset to pre-existing ground based measurements of dust aerosol from several locations. We then identify regional trends in τ_d for the period of each record.

2.3 Methodology

Two datasets of τ_d were created. The first, which hereafter will be referred to as τ_d^M, is based primarily on AOD (τ) retrievals from the MODIS instrument on the Terra platform, with a companion set of estimates created for the same instrument aboard the Aqua platform, (both accessed at https://ladsweb.modaps.eosdis.nasa.gov) and extends from 2001–2018 for the case of Terra, and 2003–2018 for Aqua. τ_d^M includes estimates over both land and water-covered surfaces. τ_d^A is based on aerosol optical thickness (AOT) retrievals from the AVHRR instruments aboard the NOAA series of satellites (Heidinger et al., 2014; Zhao et al., 2008, 2002; Zhao and Program, 2017), and covers the period 1981–2018. AVHRR AOT retrievals are not made over land, and thus τ_d^A is an over-water only product.

2.3.1 Datasets used

MODIS level 3, Collection 6.1 (C061) daily Dark Target AOD is derived from the measured 500m resolution reflectance from all visible MODIS bands by taking the average of the measured radiance over all scenes that are cloud-free and glint-free over the ocean within a 10km grid box, and fitting these values to a lookup table. Level 3 MODIS Dark target AOD is calculated using the QAC screened Level 2 (L2) pixel level data. MODIS 550nm fine mode fraction (f) is calculated from ratio of the small mode AOD to the total AOD. MODIS C006 AOD over ocean has been shown to have an expected error of $+(0.04 + 10\%) - (0.02 + 10\%)$ (Levy et al., 2013). For dust-dominated regions, it has been shown that there is a bias of +5% (Kaufman, 2005). There has been no systematic program for evaluation of MODIS f because its definition is somewhat ambiguous, making evaluations against other estimates difficult (Kleidman et al., 2005). At this time, there is no envelope of error for C061 f. However, Collection 5 (C005) f over ocean was found to agree with AEROsol RObotic NETwork (AERONET) retrieved sky radiance fine mode fraction within approximately ±0.20 (Kleidman et al., 2005), and Bréon et al. (2011) found agreement between MODIS ($\tau^{f,MODIS}$) and AERONET ($\tau^{f,AERONET}$) fine mode AOD, as evidenced by a correlation r-value of

0.76, RMSE of 0.08, bias of 0.01, and 53% of retrievals within the C005 envelope of error, $\delta\tau = 0.03 + 0.05\tau^{AERONET}$, which describes a confidence envelope containing one standard deviation (i.e.,68%) of $\tau^{f,MODIS}/\tau^{f,AERONET}$ matchups. In our estimate of the known uncertainty in τ_d, we assume that the C061 f uncertainty has not changed from the C005 values. Although a Quality Assured (QA) dataset does exist for $\tau^{f,MODIS}$, we chose to use the standard dataset in order to retain additional coverage.

The equivalent set of estimates for τ_d^M from the Aqua platform extends from 2003 to 2018. The Aqua platform passes the equator at 1:30pm in the afternoon while Terra passes near 10:30am local time. AOD from MODIS Terra and Aqua have been shown to agree very well (Ichoku, 2005). However, globally, Terra monthly mean AOD over ocean has been shown to be higher than Aqua by +0.015 (Levy et al., 2018; Remer et al., 2008). This is partially explained by diurnal cycles in cloud fraction (King et al., 2013), which may create differences in sampling between these sensors, and partially explained by issues with the total infrared radiation measured by Terra (Levy et al., 2018). This paper will focus largely on τ_d^M from the Terra platform, as it is a longer record. However, we will discuss decadal trends in τ_d^M derived from Aqua in Section 2.52.5.1.

Table 2.1: Summary of variables and data types used in equations 1, 2, and 3. f_d, f_m, and f_a represent characteristic AERONET fine mode fractions for dust, marine, and anthropogenic or biomass burning -dominated AERONET stations, respectively. τ and f represent the total AOD and fine mode fraction, and τ_m represents the marine aerosol contribution to the total AOD.

Var.	*Platform*	*Instrument*	*Retrieval Wavelength*
τ	Terra/NOAA	MODIS/AVHRR	550 nm or 630 nm
f	Terra	MODIS	N/A
f_d	AERONET	Sun Photometer (O'Neill method)	500 nm
f_m	AERONET	Sun Photometer (O'Neill method)	500 nm
f_a	AERONET	Sun Photometer (O'Neill method)	500 nm
τ_m	MERRA-2	Parameterized from surface winds	N/A

As our τ_d estimate is built upon AOD, it carries with it the known limitations

of the sensors from which it is derived. MODIS AOD retrievals are limited to cloud-free pixels and errors in cloud screening will impact the AOD estimate. The MODIS aerosol cloud mask uses the standard deviation of reflectance in sets of pixels to remove cloudy pixels, which increase spatial variability. Absolute reflectance at 1380 nm and the ratio of reflectances at 1380 nm and 1240 nm, as well as several infrared tests are used for additional screening of thin cirrus. Over ocean, the brightest and darkest 25% of the remaining pixels are arbitrarily removed and the average reflectance in each channel is calculated from the remaining pixels. Over land, the brightest 50% and darkest 30% of pixels are discarded before the averaging step (Remer et al., 2012). While this usually produces a reasonable result, in the case that unscreened clouds remain before the discarding of the brightest and darkest retrievals, this can produce AOD estimates that are biased high (Kahn et al., 2007). It is known that MODIS AOD is biased very high in the southern hemisphere mid to high latitudes over the Southern Ocean due to extensive broken stratocumulus and cirrus cloud contamination (Toth et al., 2013). We have thusly limited these datasets to extend from $60°N$ to $50°S$.

Level 2 (L2) Version 3 AOD and fine mode fraction from select sites, as will be discussed in Section 2.32.3.2, retrieved from AERONET (Holben et al., 1998, 2001) sunphotometers using the Spectral Deconvolution Algorithm (SDA) Version 4.1 (ONeill, 2003) accessed at https://aeronet.gsfc.nasa.gov are used to estimate τ_d^M and τ_d^A over the ocean. In the determination of AERONET fine mode fraction, two spectral modes of AOD are defined based on the premise that the coarse mode spectral variation is approximately neutral while the derivative of the fine mode spectral variation is an approximate function of the fine mode angstrom exponent (ONeill, 2003). From this, the ratio of fine mode to total AOD is determined at a reference wavelength of 500nm from a second order polynomial fit of the natural logarithm of AOD and wavelength applied to each AOD spectrum across six bands. This definition of fine mode fraction is different from that used in the MODIS dataset and may result in some disagreement. MODIS f has been shown to slightly overestimate the fine mode fraction in dust or salt dominated regions by 0.1 - 0.2 relative to AERONET fine mode fraction as generated from the O'Neill

algorithm (Kleidman et al., 2005), which has the potential to introduce a small positive bias in our estimated τ_d.

MODIS C061 L3 Deep Blue products (AOD, single scattering albedo (SSA), angstrom exponent (AE) accessed at https://ladsweb.modaps.eosdis.nasa.gov) were used in the estimation of τ_d^M over land (Hsu et al., 2013). These products use the blue channels of MODIS where surface reflectance is very low. Pixel level retrievals are averaged over 10km x 10km grids and data are then aggregated into granules. The L3 products are provided at 1° x 1° resolution. SSA at 412nm and at 660nm were used in addition to AE, which is inversely proportional to particle size (Angstrom, 1929). Deep Blue AOD was used as the basis for estimation of τ_d^M over land and is reported to have an expected error of +(0.04 + 10%) - (0.02+10%) (Hsu et al., 2014). The C061 Deep Blue AOD release extended coverage to all non-snow land surfaces, while C005 only included bright land surfaces.

The AVHRR AOT at 630 nm climate data record (CDR) (Zhao and Program (2017); accessed at https://www.ncei.noaa.gov/data/) was used in the estimation of τ_d^A (Zhao and Program, 2017; Chan et al., 2013). The CDR was created using the NOAA AVHRR PATMOS-x Level-2B product (Zhao et al., 2008, 2002; Zhao and Program, 2017). While there is no difference between AOD and AOT, we refer to the MODIS data as AOD and the AVHRR data as AOT as this is how each is referenced in their documentation. It combines retrievals from 17 different sensors, and the overpass time and number of observations per day (4-8 obs/day) varied between sensors. Large data gaps occur for years before 1985. AVHRR AOT was re-gridded from its native resolution of 0.1°x0.1° to a resolution of 1°x1° using inverse distance weighted interpolation. Aerosol retrievals are only available over ocean and require clear-sky conditions (Heidinger et al., 2014). The CDR AVHRR AOT dataset has a systematic error (positive bias) of 0.03 ± 0.006 and a random error of ± 0.113 (Zhao and Program, 2017). The error budget of AVHRR AOT CDR is based on AERONET validation. While another product of AVHRR aerosol loading is available, derived using algorithms from modern sensors (Hsu et al., 2017; Sayer et al., 2017), it is limited to several years. Therefore, we did not use this product.

Table 2.2: AERONET stations used for calculation of f_a, f_d, and f_m with the years of data used from each station in this calculation.

Variable	*Mean*	*AERONET Stations*
f_a	0.79	Alta Floresta (1993-2018), GSFC (1993-2018), Campo Grande (1995), Mongu (1995-2010), Mainz (1997-2018), Abracos Hill (1999-2005), BelTerra (1999-2005), Cordoba CETT (1999-2010), CEILAP BA (1999-2018), Palaiseau (1999-2018), Skukuza Aeroport (2000), UCLA (2000-2018), Hamburg (2000-2018), Rio Branco (2000-2018), Philadelphia (2001), CCNY (2001-2018), Cuiaba Miranda (2001-2018), Rome Tor Vergata (2001-2018), Fresno (2002-2012), Billerica (2002-2018), Halifax (2002-2018), New Delhi (2004-2010), Petrolina Sonda(2004-2017), Hong Kong PolyU (2005-2018), HongKong Hok Tsui (2007-2010), Dayton (2008-2018), Hong Kong Sheung (2012-2018).
f_d	0.35	Solar Village (1999-2015), Hamim (2000-2007), Tamanrasset INM(2006-2018), Tamanrasset TMP(2006), Eilat (2007-2018)
f_m	0.34	Midway Island (2001-2015), Nauru (1999-2013), Amsterdam Island (2002-2018), Crozet Island (2003-2013), ARM Graciosa (2013-2018), American Samoa (2014-2017)

Daily mean surface wind speed from the second Modern-Era Retrospective Analysis for Research and Applications (MERRA-2) (Gelaro et al., 2017) one hour time-averaged surface flux assimilation product (accessed at https://disc.gsfc.nasa.gov/) was used in the estimation of marine AOD. This was re-gridded from its native resolution of 0.625°longitude x 0.5°latitude to a resolution of 1° x 1° using bilinear interpolation. MERRA-2 surface wind patterns have been shown to be similar to other datasets, but greater in magnitude in most regions than MERRA and ERA-Interim and weaker in magnitude than NCEP-R2 (Bosilovich et al., 2015). Similar to most reanalysis products, MERRA-2 winds are weaker than 93% of observations considered in Bosilovich et al. (2015).

2.3.2 MODIS dust optical depth over ocean

Our method for estimating τ_d^M over ocean surfaces is based on Kaufman (2005). Underlying this method is the assumption that the major contributions to total AOD are anthropogenic and biomass burning aerosol, marine aerosol, and dust aerosol, and thus one can deduce τ_d by estimating the contributions from the other aerosol types. As anthropogenic and biomass burning aerosols are generally dominated by submicron particles with AE greater than 1 (Dubovik et al., 2002; Schmeisser et al., 2017), f can be used to discriminate these types from the contributions by coarse mode-dominant aerosol types.

The total aerosol optical depth (τ) is

$$\tau = \tau_d + \tau_m + \tau_a \tag{2.1}$$

where τ_m and τ_a are the marine, and anthropogenic or biomass burning contributions to τ, respectively. Here we have combined the biomass burning and anthropogenic aerosols for convenience, as they both have a dominant fine mode and will thus be isolated and removed from τ simultaneously. The fine mode aerosol optical depth is given by $f\tau$, and can be expressed as a function of the fine mode optical depth contributions from the individual aerosol species,

$$f\tau = f_d\tau_d + f_m\tau_m + f_a\tau_a \tag{2.2}$$

where f, f_d, f_m, and f_a are the total, dust, marine, and anthropogenic or biomass burning contributions to f, respectively. Equations 1 and 2 can be combined and rearranged to yield τ_d,

$$\tau_d = \frac{\tau(f_a - f) - \tau_m(f_a - f_m)}{f_a - f_d} \tag{2.3}$$

Data sources for each of these variables can be found in Table 1. Characteristic values of f_m, f_a, and f_d were determined using the average of fine mode fraction from AERONET stations dominated by each aerosol type, weighted by the total τ (Table 2). This weighting was performed for each station according to:

$$f = \frac{\sum_{i=1}^{N} f_i * AOD_i}{\sum_{i=1}^{N} AOD_i} \tag{2.4}$$

Where f is f_a, f_d, or f_m. For f_a and f_d, AERONET stations were chosen based on Cazorla et al. (2013). For f_m, marine aerosol-dominated AERONET island stations were selected based on Lehahn et al. (2010) and Chaubey et al. (2011) and through visual selection of additional remote island sites. MODIS retrievals were not used for determining these coefficients since f is only distinguishable over the ocean with this instrument. This makes it likely that all MODIS f estimates contain some significant contribution from sea spray and as such represents a deviation from the methods of Kaufman (2005).

Marine aerosol contribution

Kaufman (2005) parameterized marine aerosol based on NCEP surface (1000hPa) wind speed at 2.5° x 2.5° resolution. This parameterization was based on the relationship between surface wind speed from a National Climatic Data Center (NCDC) meteorological station and an AERONET station on Midway Island from 14 months of data, excluding the dust season (February through May) (Smirnov et al., 2003).

Here we consider that the total marine aerosol optical depth is given by

$$\tau_m = \tau_{m,c} + \tau_{m,f} \tag{2.5}$$

where $\tau_{m,c}$ and $\tau_{m,f}$ are the coarse and fine mode contributions to marine aerosol. We make the assumption that $\tau_{m,f}$ is weakly dependent on wind speed (Satheesh et al., 2006), and that the dependence of τ_m on surface wind speed is primarily from $\tau_{m,c}$ (Lehahn et al., 2010). We identified a region dominated by marine aerosols (0-25°S, 178-130°W), and set $\tau_{m,f}$ equal to the long-term MODIS fine mode aerosol optical depth,

$$\tau_{m,f} = 0.05(\pm 0.03) \tag{2.6}$$

where ± 0.03 is the standard deviation of the daily MODIS fine mode aerosol optical depth at 0-25°S, 178-130°W from 2001 to 2017 (Figure 2.1c). Assuming the linear relationship,

$$\tau_{m,c} = \alpha w \tag{2.7}$$

where w denotes surface wind speed and it is implied that $\tau_{m,c} = 0$ in the absence of surface winds, the proportionality term α was calculated via regression of MODIS Terra coarse mode AOD onto MERRA-2 surface wind speeds, both interpolated to a 1°x1° horizontal resolution, and over the same region used to calculate $\tau_{m,f}$. Via the linear regression (Figure 2.1b),

$$\tau_{m,c} = 0.008(\pm 0.0001)w \tag{2.8}$$

which is consistent with Lehahn et al. (2010), who found $\tau_{m,c}$ to be linearly related to surface wind speed with a slope of $0.009 \pm 0.002 m/s$. We tested three other parameterizations for marine aerosol and found that this parameterization resulted in the lowest bias (+0.02) and lowest root mean squared error (RMSE) (0.04) when compared with AERONET AOD at Nauru, a remote island station, from 2001 to 2014 for days on which there were clear-sky measurements from both instruments. These other parameterizations are described in the Supplementary Information.

Sea salt aerosol has been parameterized previously using linear (Lehahn et al., 2010; Smirnov et al., 2003; Mulcahy et al., 2008; Glantz et al., 2009; Huang et al., 2010), power-law (Mulcahy et al., 2008; Glantz et al., 2009), and exponential (Moorthy and Satheesh, 2000) relationships to 10m or surface wind speeds from in-situ and remote sensing measurements. It is well known that, to first order, sea salt emission is primarily dependent on wind speed (Jaeglé et al., 2011). However, other factors including sea surface temperature (SST), organic material, vertical mixing, advection, wet and dry deposition, and relative humidity could impact sea salt emission to a lesser extent. The second most commonly used predictor, after wind speed, is SST (Jaeglé et al., 2011; Gong, 2003). However, laboratory and in-situ investigations of the SST dependence of marine aerosol have had contradictory results, indicating that we do not yet fully understand how temperature impacts SSA (Grythe et al., 2014; Mårtensson et al., 2003; Zábori et al., 2012). Therefore, we have chosen to retain a parameterization that is only based upon surface winds.

2.3.3 τ_d^M over land

τ_d^M over land for the time period between 2001 and 2018 was estimated based on the methods of Ginoux et al. (2012) with minor modifications. Ginoux et al. (2012) used collection 5 (C005) MODIS Deep Blue AOD to identify pixels over land that contained dust by their column optical characteristics including AOD greater than 0.1, AE less than 0, SSA at 412 nm less than 0.95, and SSA at 412nm less than or equal to SSA at 660nm. The AE criteria selects for pixels with a dominant coarse mode to the aerosol size distribution (Ginoux et al., 2012), which should primarily be dust and marine aerosol (Dubovik et al., 2002). The criteria for SSA at 412nm is related to absorption of solar radiation in the green channel, characteristic of dust, and is effective at removing influences of marine aerosol. The difference in SSA between 660nm and 412nm is used because an optical property of dust is a positive spectra variation of SSA with wavelength, which manifests as a sharp decrease in absorption from the red (660nm) to blue (412nm) channels. This criteria is effective at removing any additional influence of biomass burning, as biomass burning particles have spectral variation with the opposite slope. If a retrieval met all of these criteria, its Deep Blue AOD contributed to the long-term mean of τ_d at that grid cell. In order to test the thresholds used in Ginoux et al. (2012), we collected these same data within three over-land regions where the aerosol signal is dominated by dust, and one over-land region where mineral aerosols are unlikely to be present, and binned the pixels of this data for each location by their optical properties using the time period 2006 to 2010. The boundaries of these regions were chosen visually, selecting for either desert surface boundaries or for vegetation cover (Figure S8). The dust-dominated locations included a region over the Sahara desert (10-30°E, 19-30°N) (Figure 2.2a), a region over the Arabian desert (40-50°E, 23-35°N) (Figure 2.2b), and a region over the Taklamakan desert (77-88°E, 36-40°N) (Figure 2.2c). The non-dust dominated location chosen was over equatorial Africa (10-32°E, 10°S-5°N) (Figure 2.2d).

In all three dust-dominated regions, 97-100% of pixels meet the criteria for SSA at 412nm less than 0.95 while in the region dominated by other aerosol types, less than 26% of pixels meet this criteria. Similarly, in each dust-dominated region,

greater than 99% of pixels meet the criteria of SSA at 412nm exceeding or equal to SSA at 660nm, while only 40% meet this criteria for the non-dust region. The criteria used in Ginoux et al. (2012) of AOD greater than 0.1 was not used in the creation of τ_d^M here, as we were concerned that this threshold would systematically bias our results.

Ginoux et al. (2012) used a conservative requirement of AE less than 0 to identify dust. However, the updated algorithm used to create the C006 Deep Blue AE product now limits the valid range of values to $0 \geq \text{AE} \leq 1.8$ (Sayer et al., 2013; Hsu et al., 2013). Therefore, we chose a new threshold based on the distribution of AE in our three desert regions. When this threshold was replaced with a criteria of AE less than 1, 90% of pixels in the Sahara desert region, 91% of pixels in the Arabian desert region, and 73% of pixels in the Taklamakan desert region met the new threshold while only 5% met it in the non-dust region. The new threshold of 1 we have used here is within the values of AE reported for dust regimes in Dubovik et al. (2002). In summary, daily estimates of τ_d^M over land grid cells are comprised of the Deep Blue AOD if that pixel met the following criteria,

- MODIS C061 AE 470nm-670nm, which is inversely proportional to particle size, less than 1
- MODIS C061 SSA at 412 nm, the ratio of aerosol scattering to extinction coefficients at that wavelength, less than 0.95
- MODIS C061 SSA at 412 nm less than or equal to SSA at 660 nm

If a pixel did not meet these criteria its τ_d was set equal to zero. An analysis of the accuracy of this method, through comparison with AERONET, is presented in the supplementary materials.

2.3.4 τ_d^A (1981 - 2018)

$\tau_{d,AVHRR}$ over the ocean from 1981 to 2018 was derived similarly to what was previously described for MODIS. However, AOT from AVHRR was used rather than MODIS AOD, and the climatological seasonal mean f from the MODIS

period, calculated from the MODIS small mode 660nm AOD divided by the total 660nm AOD, was used in Equation 2.3 as there is a spectral dependence of f. Evan and Mukhopadhyay (2010) showed that over the tropical North Atlantic, a dusty region, the seasonal cycle in f is far larger than the inter-annual variability, such that monthly climatological mean f can be used in place of monthly-mean f without introducing significant biases. Here we also assume that the use of monthly climatological f can be used in place of daily f. We tested this assumption by calculating the τ_d^M using climatological f. The results were similar to τ_d^M calculated using daily f with a bias of 0.00 in the long-term global mean over the ocean for the period 2001-2017 (RMSE: 0.03). The characteristic fine mode fractions, f_m, f_d, and f_{an}, were the same as those used in the calculation of τ_d^M.

Following Evan and Mukhopadhyay (2010), a time series of zonal mean stratospheric aerosol optical thickness (τ_s) as estimated in Sato et al. (1993) was removed from AVHRR AOT before calculation of τ_d^A for years prior to 1999 and was assumed to be zero in subsequent years. This was done to remove the impact of large volcanic eruptions, including Pinatubo (June 1991) and El Chicon (March, April 1982), on τ_d^A. τ_s was not removed in years following 1999 as there have been no volcanic eruptions of the scale of Pinatubo or El Chicon since 1999. While the total column AOT peaks immediately following these major erruptions, τ_s does not peak until 1-3 months later (Figure 2.3). This offset results in a remaining peak in the τ_s-corrected AOT, which leads to a coincident peak in τ_d^A. In our analysis of trends in τ_d^A, we exclude the years 1982 and 1991 in order to avoid the impact of these events.

Our resultant global mean time series of τ_d^A exhibits fluctuations in years prior to 1995 that are associated with satellite drift, a known issue with the pre-KLM NOAA satellites, which has been investigated with respect to long-term variability in cloud cover (Foster and Heidinger, 2013; Norris and Evan, 2015). Satellite drift, or orbital decay, results in a progressively later equatorial crossing time. Thus, biases in optical depth retrievals may be due to retrieval errors associated with larger solar zenith angles (Figure 2.3), or sampling of the diurnal cycle (Norris and Evan, 2015). We remove the signal associated with satellite drift via linear

regression, following the methods of Norris and Evan (2015). Consequently, at each location, the resultant τ_d^A values are anomalies relative to the global mean.

2.4 Results

The primary results of this work are two nearly-global, daily, observational datasets of τ_d at a 1° horizontal resolution that can be used for studies of the global dust cycle. The long-term mean global τ_d^M over the ocean was found to be 0.03 ± 0.06 where ± 0.06 is the $\pm 1\sigma$ error estimate. For comparison, Ridley et al. (2016) found global dust AOD at 550nm to be 0.03 ± 0.005 using in-situ and satellite observations combined with global models. The long-term mean global τ_d^M over land was foumd to be 0.1. The remainder of this section will be used to present 2.4.1) a comparison of τ_d^A and τ_d^M, 2.4.2) verification of τ_d^M against ground-based measurements of dust, and 2.4.3) a description of seasonal climatological mean τ_d.

2.4.1 Comparison of τ_d^M and τ_d^A

Globally, monthly mean estimates of τ_d^M and τ_d^A agree well, as evidenced by a high correlation coefficient between the two data ($r^2 = 0.41$), a linear least squares regression slope near unity ($y = 0.90(\pm 0.001)x$), a low RMSE (0.07), and a low offset (-0.01) (Figure 2.4b). Much of the disagreement between the two occurs in locations where there are few days on which both AVHRR and MODIS have retrievals (Figure 2.6). This is often the case in latitudes above $30°N$ and below 30° as well as in characteristically cloudy regions such as the ITCZ ($0 - 10°N$), the southeast Atlantic ($10 - 20°S, 10°W - 10°E$), and the southeastern boundary of the Pacific. In dust-dominated regions,τ_d^M and τ_d^A are very well correlated, but with a slope that is greater than one. For example, in the tropical North Atlantic, the only ocean region where mean τ_d^M is greater than 0.3 in all seasons (Figure 2.10), they are linearly related with a form $y = 1.21(\pm 0.005)x - 0.03$ ($r^2 = 0.76$, RMSE:0.08, Offset: -0.00) (Figure 2.4d). Monthly mean τ_d^A is offset low (Bias:-0.18) compared to τ_d^M for τ_d^M greater than one. We hypothesize that the low offset in τ_d^A is an artifact of misclassification of optically thick dust layers as clouds in the

AVHRR AOT cloud clearing algorithm (Xuepeng Zhao, personal communication, April 18, 2018), although it is also contributed to by the difference wavelengths between MODIS AOD retrievals and AVHRR AOT retrievals (Zhao et al., 2008). In order to determine boundaries around the potential contribution to the offset by the difference in wavelength of AOD retrieval, we perform a back-of-the-envelope calculation. The largest percentage difference in AOD at each wavelength should occur when the AE is large. We use AERONET 500nm and 675nm AOD at the (dust-dominated) Tamanrassett station to calculate the mean, upper, and lower quartile of AE for these wavelengths, using only days that met the criteria used for ground-truth validation of dust (see supplemental materials). In the absence of a 550nm-630nm AE from MODIS, we assume that this 500nm-675nm AE from AERONET is similar enough to approximate the influence of wavelength differences on the offset between MODIS and AVHRR. Using the lower quartile AE at Tamaransett, 0.12, we find that the wavelength difference would contribute a 1.6% offset with τ_d^M greater than τ_d^A. Using the mean AE at Tamaransett, we find a potential offset of 3.5%, and using the upper quartile, 5.8%.

We also calculated the linear least squares best-fit between the daily τ_d^M and daily τ_d^A, including only dates and pixels where both sensors retrieved AOD (Figure 2.4d). We expect that if the low offset of τ_d^A relative to τ_d^M is contributed to by missing data in regions of optically thick dust, the slope of the regression between these datasets will be significantly less steep for the daily data than for the monthly data in the tropical North Atlantic (Figure 2.4d). This is because for the monthly mean, MODIS would incorporate high τ_d days that AVHRR 'missed'. Indeed, we found that the daily τ_d^M and daily τ_d^A are related by the relationship $y = 0.95(\pm 0.0002x - 0.01$ ($r^2 = 0.54$, RMSE:0.13, Offset: -0.01) in the tropical North Atlantic. Globally, daily daily τ_d^M and daily τ_d^A are related by the relationship $y = 0.70(\pm 0.0003)x + 0.01$ ($r^2 = 0.26$, RMSE:0.09, Offset: -0.01) (Figure 2.4c).

The discrepancy in retrievals over large dust plumes can be easily visualized in the case of June 27th, 2014, over the tropical Atlantic (Figure 2.5). In this case, τ_d^M indicates an optically thick dust plume, centered near 15°N, 30°W, that has been advected over the tropical Atlantic from the Sahara (Figure 2.5a). This

particularly strong event allowed for dust to be measured in-situ as far as Colombia (Bedoya et al., 2016). In Figure 2.5, grid cells that are missing estimates of τ_d or AOD, or grid cells over land, are masked in grey. For the same day, the τ_d^A (Figure 2.5b) is largely missing estimates in the region of optically thick dust. This is a result of missing retrievals of AVHRR AOT (Figure 2.5d), which occur due to a combination of sun glint and because of the cloud-screening algorithm classifying optically thick dust as cloud.

2.4.2 Comparison with existing datasets

It is informative to compare our τ_d to previously published estimates of atmospheric dust. Here, we compare τ_d^M with two recently published time series of dust concentrations over the western U.S. (Tong et al., 2017; Hand et al., 2016) and one over the Caribbean (Prospero and Nees, 1986; Prospero et al., 1996). The measurements of dust over the western U.S. are based on surface concentrations of aerosol species. In Hand et al. (2016), Fe from IMPROVE stations was used as a proxy for fine dust concentrations and τ_d^M compares well with these annual mean fine dust concentrations (r-value = 0.61, p-value < 0.01) (Figure 2.7). In Tong et al. (2017) several criteria from ground-based IMPROVE data were used to confirm dust events that had been detected in satellite imagery. The criteria included: high PM_{10} and $PM_{2.5}$ concentrations, a low ratio of $PM_{2.5}$ and PM_{10}, high concentrations of crustal elements (SI, CA, K, Fe, and Ti), low concentration of anthropogenic components, and low enrichment factors of pollution elements. Annual mean τ_d^M is strongly correlated to estimates of annual number of dust events (r-value = 0.73, p-value < 0.05) from this work. Toth et al. (2014) found that globally, the average correlation between total AOD and AOD integrated from 500m a.g.l. to the surface was 0.61 over land. For CONUS, this correlation was found to be 0.62 with 0.57 over the western time zone. Therefore, although τ_d is a measure of column integrated aerosol, we still expect surface concentrations to be correlated with column integrated values, especially when averaged over a large region. Interestingly, while an increasing trend in dust was noted for these studies for the period between 2001 and 2015, from these results, the extension of the time

series through 2017 indicates that dust has been decreasing since 2011.

We also compared our new climatology of τ_d^M with long-term, independent, ground-based dust measurements of dust taken at Ragged Point, Barbados (Prospero and Nees, 1986; Prospero et al., 1996; Prospero, 2014). These measurements are based on ash residue from extracted filters with an adjustment factor based on average crustal abundance of Aluminum in soil dust. These data have a standard error that is approximately constant at $\pm 0.1 \mu g m^{-3}$ for concentrations less than 1 $\mu g m^{-3}$ and about $\pm 10\%$ for higher concentrations. We found that in addition to matching the seasonal cycle of dust at this location (Figure 2.8b), monthly-mean τ_d^M over Barbados is positively and statistically significantly correlated (r-value = 0.50, p-value < 0.01) with monthly-mean ground-based dust aerosol measurements when the seasonal cycle is removed from both time series (Figure 2.8a). Monthly mean τ_d^A from 1982 to 2013 is also statistically correlated (r-value = 0.33) with dust concentrations at Barbados, and shows the same seasonality there as τ_d^M (Figure S3).

We also compared our dataset with a monthly time series of dust optical depth (DOD) over Syria as published by Pu and Ginoux (2016) (Figure 2.9). Similar to Ginoux et al. (2012), Pu and Ginoux (2016) used MODIS Deep Blue C006 AOD, SSA, and AE to construct DOD, and thus the data sets are not independent. However, Pu and Ginoux (2016) updated their method by interpolating optical properties to a 0.1°x0.1° grid and using a threshold of SSA at 470nm along with an empirical relationship between AE and f to derive coarse DOD. The time series are related with a correlation coefficient of 0.87 (p-value<0.01) and show the same trend of increasing dust over Syria (Figure 2.9). We are not aware of another independent estimate of τ_d^A against which we can make a comparison.

2.4.3 Seasonal Dust AOD

Having shown that this satellite-based climatology of dust appears to reflect changes in the atmospheric concentration of dust, we next summarize some of the broader characteristics of the global dust cycle, starting with seasonality. Maximums in seasonal mean τ_d^M are found over the Sahara and the Arabian Peninsula

in austral summer (JJA) (Figure 2.10d) and over the Taklamakan and Gobi deserts during spring (MAM) (Figure 2.10c). Aeolian transport from the Sahara towards the Americas is visible during all seasons with a maximum extension westward during the summer (Figure 2.10d,h), which is well known (Prospero and Mayol-Bracero, 2013; Prospero et al., 1996). Seasonal mean τ_d^A, appears far lower than τ_d^M near to major dust sources in all seasons, due to limited retrievals in regions of optically thick dust as described in the previous section. The Spring maximum in dust over Asia can be attributed to the seasonal cycle of the Mongolian cyclonic depression and the related high frequency of springtime cold air outbreaks (Sun et al., 2001; Ge et al., 2014). During this season, dust is transported from the Asian continent over the North Pacific Ocean towards North America at latitudes between 30°N and 50°N. It is presumed that this dust is primarily from the Taklimakan desert as the local topographical and meteorological conditions allow for it to be entrained to elevations exceeding 5km while dust from the Gobi desert is, for the most part, confined closer to the surface (<3km) (Sun et al., 2001). It has also been shown that some portion of this trans-Pacific dust originates from Africa (Creamean et al., 2013).

Discrepancies between τ_d^M over land and τ_d^M over adjacent ocean are visible in some areas with significant anthropogenic aerosol sources, including the Sahel region of Africa and India during austral Fall and Spring (Figure 2.10a,c). This may be due to different methods and data sources used for estimating τ_d^M over land and ocean. The method used for τ_d^M over the ocean leads to a continuous range of τ_d^M, whereas the threshold approach used for estimation of τ_d^M over land may prevent these gradients when there is mixing between anthropogenic aerosols and dust aerosol. However, this may also partially be the result of the different algorithms used in the retrieval of AOD over land and ocean (Sayer et al., 2013; Hsu et al., 2013) (Figure S4). While these unphysical discrepancies could be avoided through spatial interpolation across these boundaries, we have chosen not to do this in order to minimize our assumptions and retain a daily dataset that is directly representative of the satellite observations. At the very least, these results suggest that direct comparison of over-land and over-water τ_d may be problematic.

A region of high summertime mean τ_d^M is visible over the North Pacific Ocean near 45°N (Figure 2.10d). Summertime trans-Pacific transport of dust has been observed (Yumimoto et al., 2010). However, visual inspection of MODIS Terra corrected reflectance on days when τ_d^M over the western North Pacific was high during summer months indicated the possibility of contamination from biomass burning over Europe and Russia. We compared summer seasonal mean τ_d^M and MERRA-2 organic carbon extinction optical thickness at 550nm (Figure S5, accessed at https://giovanni.gsfc.nasa.gov/) and confirmed that summer seasonal mean organic carbon was highest over the western North Pacific in years when summer seasonal mean τ_d^M was highest. This supports the hypothesis that there may be biomass burning contamination over the western North Pacific during these months. The fine mode fraction (f) during these summer high τ_d^M events is approximately $0.57 - 0.63$. In the springtime, most of the high τ_d^M events are associated with fine mode fractions near 0.50, which is closer to f_d.

In addition, this region in the western North Pacific has few retrievals during the summer months due to extensive low cloud cover. The limited number of retrievals is evident in the number of pixels used in the estimate of MODIS Dark Target AOD during the summer in that region. While greater than 36 pixels are incorporated on average in the equatorial Pacific estimations of MODIS Dark Target AOD, only approximately 26 on average are used in this estimation in parts of the western North Pacific. Long-term seasonal mean τ_d^A appears low in the western North Pacific in all seasons (Figure 2.10c-f).

2.5 Discussion

Having presented two datasets of τ_d drived from satellite observations, we next present 2.5.1) regional trends in τ_d as well as 2.5.2) a comparison of τ_d^M to a modern reanalysis dust extinction aerosol optical depth product.

2.5.1 Trends in τ_d^M

In Figure 2.11a we show regional trends in monthly mean τ_d^M from Terra between 2001 and 2018, where the seasonal cycle has been removed. Only trends that are significant at the 95% confidence level are shown. One region that stands out with a large upward trend in dust is the Arabian Peninsula, where values exceed 0.3 decade^{-1} for the MODIS period. This is consistent with previous studies that found increasing trends, of smaller magnitude, in τ in this region (Hsu et al., 2012; Alfaro-Contreras et al., 2017; Toth et al., 2016). Parts of the Saharan desert appear to be getting dustier in τ_d^M from Aqua. However, coastal Northern Africa and the edges of the Sahara display decreasing trends in τ_d^M from Terra (Figure 2.11). Our results show a statistically significant decrease in τ_d^M over Northern China (approximately $100°E, 40°N$), and over Southwest Asia (approximately $180°E, 30°N$). This is consistent with recent findings by Pandey et al. (2017), who found that pre-monsoon dust loading decreased between 2000 and 2015. This decrease has been linked to increased rainfall, and resultant wet scavenging and increased soil moisture, and, to a lesser extent, decreased wind strength. The decrease in τ_d^M over northeast Asia may also be the continuation of a documented decreasing trend from the late 1950s through the 1980s in the region due to reduced cyclone frequency (Qian et al., 2002).

Interestingly, the greatest increase in τ_d^M (1.04 units/decade) is seen over the Aral Sea at the intersection of Kazakhstan and Uzbekistan (44.5°N, 59.5°E). This was once the location of one of the world's largest lakes, spanning over 66,000 km^2 (Izhitskiy et al., 2016). However, the lake has been drying up since the early 1960s, when irrigation projects diverted the rivers that fed it leaving behind a highly emissive exposed playa (Micklin, 1988; Indoitu et al., 2015). The eastern basin of the lake dried up completely in 2014, but the northern parts of the sea remain filled and have largely stabilized. A dramatic increase in τ_d^M is also seen over Razzaza Lake in Iraq, where the shoreline is receding due to diverted irrigation water. The northern-most region of the Caspian Sea, which is also the shallowest portion of the sea, shows a smaller but significant increase in τ_d^M potentially due to the recession of this body of water over the past two decades (Chen et al., 2017).

τ_d derived from MODIS Aqua (2003-2018) displays the same trends of decreasing dust over northeast China and southwest Asia and increasing trends over the Arabian Peninsula (approximately $70°E, 20°N$) and Central Sahara (approximately $10°E, 20°N$) (Figure 2.11b). There are some regional changes that are more pronounced in this record, including a statistically significant increase in τ_d over Southern California (approximately $119°W, 34°N$). There is also a large increase in dust over Oman (0.20; approximately $57°E, 20°N$) that is not present in the τ_d^M derived from Terra and a greater increase over Iran than is present in the τ_d^M derived from Terra. Differences in regional trends between these two datasets could be due the differences in the length of record, as well as the differences in overpass time for the two satellites from which the datasets are derived as it relates to the daily cycle of dust emission (Heinold et al., 2013; Kocha et al., 2013). Terra has a morning orbit while Aqua has an afternoon orbit (Ichoku, 2005). However, it has been shown that although there is no significant overall trend, the offset between the Terra and Aqua C6 total AOD records has oscillated direction over time, and its variability has increased (Levy et al., 2018). This is likely to impact the differences in τ_d^M from Aqua and Terra.

Trends in over-water τ_d, from 1981 to 2018, were also calculated using monthly mean τ_d^A (Figure 2.11c). Over these longer time periods, there is a small increasing trend in τ_d^A near the Arabian Peninsula (0.02 /decade) and a decreasing trend in τ_d^A in the tropical North Atlantic near to the African coast (0.01 /decade). The decreasing trend over offshore of Northern Africa is consistent with the time series of dust at Cape Verde ($23.04°W, 16.5°N$) created using a similar method (Evan and Mukhopadhyay, 2010), and with another study that utilized satellite and coastal surface measurements (Chin et al., 2014).

We note that Zhao et al. (2013) found a slight positive trend in the CDR AVHRR AOT record that is the result of residual cloud contamination. As such, trends in the tropical North Atlantic and Arabian Peninsula could be similarly biased.

2.5.2 Comparison with a modern reanalysis dust product

In order to understand whether this observation-based dataset is consistent with a modern reanalysis dust product, we compared τ_d^M to MERRA-2 dust extinction aerosol optical thickness at 550nm (accessed at https://giovanni.gsfc.nasa.gov/giovanni/) over two of the regions — Barbados and the southwestern U.S. — used previously in our comparisons with ground observations (Figure 2.7-2.8). Our monthly mean τ_d^M, with the seasonal cycle removed,was significantly correlated at the 99% confidence level (r-value = 0.73) to the monthly mean MERRA-2 dust extinction aerosol optical thickness over Barbados (Figure 2.12a). However, the annual mean τ_d^M displays greater inter-annual variability and was much more similar to the ground observational record than the MERRA-2 dust extinction aerosol optical thickness over the southwestern U.S. (Figure 2.12b). Over this location, the MERRA-2 dust record was not statistically significantly correlated (r-value = 0.20) with τ_d^M.

2.6 Conclusion

These global, daily, observation-based datasets of dust aerosol optical depth are rooted in observations of optical characteristics of the aerosol column from Terra MODerate resolution Imaging Spectroradiometer (MODIS) and from the Advanced Very High Resolution Radiometer (AVHRR), but incorporate observations of characteristic fine mode fraction in dusty, clean marine, and anthropogenically dominated regions from the Aerosol Robotic Network (AERONET) as well as surface wind speed from the second Modern-Era Retrospective Analysis for Research and Applications (MERRA-2). As previously mentioned, the long-term mean global τ_d^M over the ocean was found to be 0.03 ± 0.06. While there are few measurements of dust aerosol for comparison, τ_d^M over land compares well with ground-based measurements of dust from the Inter-agency Monitoring of Protected Visual Environments (IMPROVE) network in the western United States and τ_d^M over ocean compares well with independent ground-based measurements made at Ragged Point, Barbados.

While we hoped to create a reliable dataset of τ_d^A extending from 1981 to 2018

using AVHRR aerosol optical thickness (AOT) from the Climate Data Record (CDR) AOT dataset, we found that the AVHRR AOT had limited coverage in dusty regions. Comparison of daily AVHRR AOT and MODIS AOD over the tropical Atlantic indicated that this limited coverage is at least partially explained by optically thick dust identified as cloud in the AVHRR cloud masking process. This limited coverage results in a low offset in seasonal and monthly mean τ_d^A when compared with τ_d^M. We found that τ_d^M increased in the central Sahara and the Middle East and decreased over northern China and southwestern Asia between 2001 and 2018. The largest increase in τ_d occurred over the Aral Sea which has receded, leaving emissive playa surfaces exposed. We found decreasing trends in τ_d^A near Africa in the equatorial Atlantic and increasing trends near the Arabian Peninsula from 1981 to 2018.

In 2011, the Suomi National Polar-Orbiting Partnership (S-NPP) satellite was launched carrying the Visible Infrared Imaging Radiometer Suite (VIIRS), which is intended to continue the observational records that have been provided by sensors such as MODIS and AVHRR (Sayer et al., 2017). VIIRS has been shown to be capable of identifying aerosol type and partitioning between fine and coarse mode aerosol. As such, observational studies that require a shorter record (beginning in 2012) may be able to rely on these products. In addition, Chen et al. (2018) demonstrated that an inversion technique, utilizing the GOES-Chem model, can be applied to certain satellite aerosol optical property retrievals in order to retrieve desert dust. This was applied to one year of satellite-derived aerosol information generated by the GRASP (General Retrieval of Atmosphere and Surface Properties) algorithm from POLDER/PARASOL (Polarization & Anisotropy of Reflectances for Atmospheric Sciences coupled with Observations from a Lidar) retrievals. While this technique can provide daily dust at 2°x2° resolution with uncertainty below 25.8%, it is computationally costly and has not been applied to longer records of remotely sensed aerosol optical properties.

The current work provides daily τ_d generated from a simple algorithm and observed aerosol data. Previous estimates of τ_d have enhanced our understanding of the global dust cycle and have been a valuable tool for evaluating the performance

of global models (Pu and Ginoux, 2018a; Evan and Mukhopadhyay, 2010; Kaufman, 2005; Ginoux et al., 2012). This longer, higher temporal resolution record will facilitate additional advances in our understanding of the dust cycle.

2.7 Acknowledgments

This work was funded by the California Department of Water Resources contract 4600010378, Task Order $OSCOP215$ and the Army Corps of Engineers USACE (CESU) $W912HZ-15-0019$. We thank the AERONET PIs and their staff for establishing and maintaining the 39 sites used in this investigation. We are grateful for the datasets and data archiving centers that supported this work and appreciate those who made our study possible, including the MERRA-2 team at the GMAO and staff at GSFC, and the MODIS teams at NASA, as well as Tom Zhao and the NOAA Climate Data Record team. We thank Dr. Joseph Prospero, Dr. Jennifer Hand, and Dr. Daniel Tong for their contributions of long term datasets for comparisons made in this work, and Dr. Martin Ralph, Dr. Leah Campbell and Dr. Nora Mascioli for helpful comments on this manuscript. We also thank three anonymous reviewers for helpful comments on this manuscript. The datasets described in this manuscript will be made publicly available at Pangea Open Access (https://doi.pangaea.de/10.1594/PANGAEA.909140).

Chapter 2, in full, is a reprint of the material as it appears in Journal of Applied Meteorology and Climatology. Kara K. Voss and Amato T. Evan, (2020). A new satellite-based global climatology of dust aerosol optical depth, Journal of Applied Meteorology and Climatology, doi:10.1175/JAMC-D-19-0194.1. The dissertation author was the primary author of this paper.

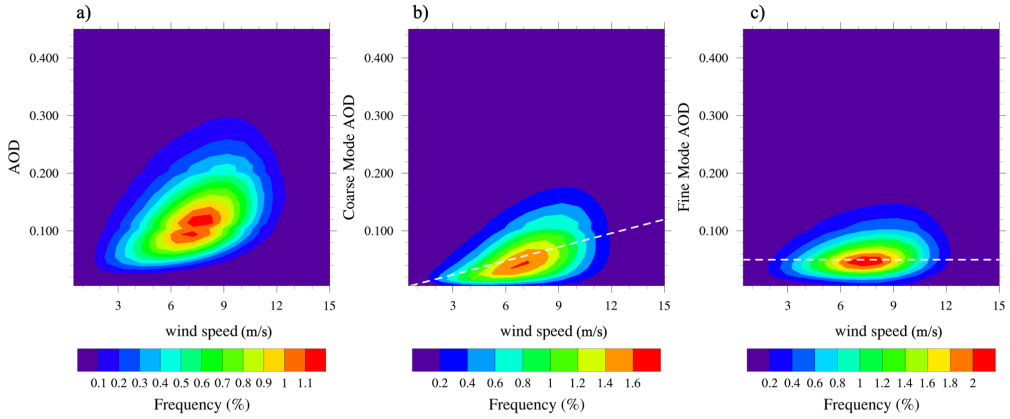

Figure 2.1: Joint probability distribution of MODIS Terra a) AOD, b) coarse mode AOD, and c) fine mode AOD binned by daily mean MERRA-2 wind speed in the southern equatorial Pacific $(0-25°S, 178-130°W)$ from 2001 to 2017. The color contours indicate the percent of total pixels falling within each wind speed and AOD bin. The linear parameterization used to estimate coarse mode AOD from wind speed ($\tau_{m,c} = 0.008$) is shown in the white dashed line in panel b. The constant fine mode AOD parameterization ($\tau_{m,f} = 0.05$) is shown in the white dashed line in panel c.

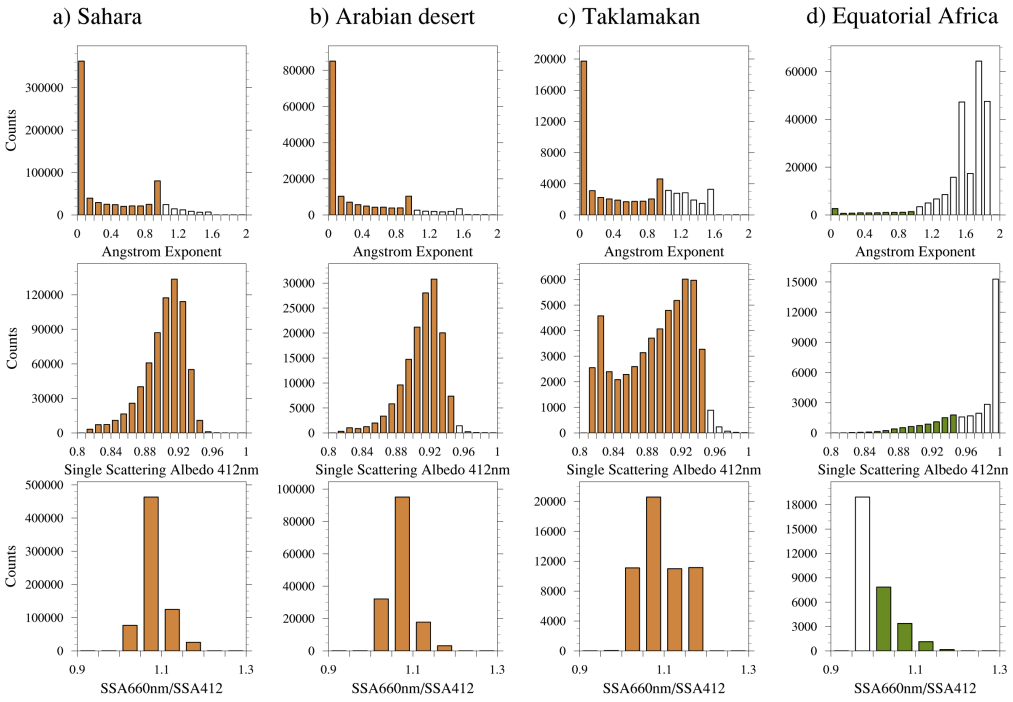

Figure 2.2: Histograms of Angstrom Exponent (top), Single Scattering Albedo (middle), and ratio of Single Scattering Albedo at 412 nm divided by Single Scattering Albedo at 660nm (bottom) for three characteristically dusty regions a) the Sahara desert ($19-30°N, 10-30°E$), b) the Arabian desert ($23-35°N, 40-50°E$), and c) the Taklamakan desert ($36-40°N, 77-88°E$), and one anthropogenic aerosol dominated region, d) equatorial Africa ($10°S-5°N, 10-32°E$) for the period from 2006 to 2010 daily C061 L3 MODIS Deep Blue products. Colored brown (a-c) or green (d) bars indicate bins that match the criteria used to identify dust for the respective optical property.

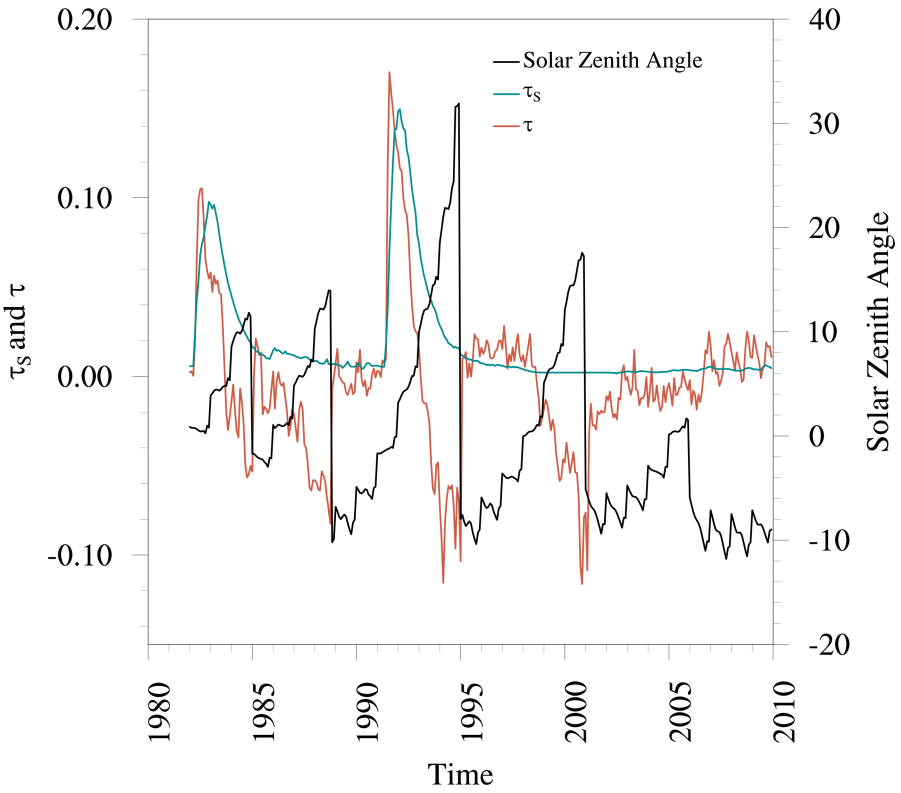

Figure 2.3: Uncorrected global mean time series of AVHRR AOT (τ) (red), AVHRR retrieval Solar Zenith Angle (black) and stratospheric AOD (τ_s) (cyan) from Sato et al. (1993), each from monthly mean with seasonal cycled removed.

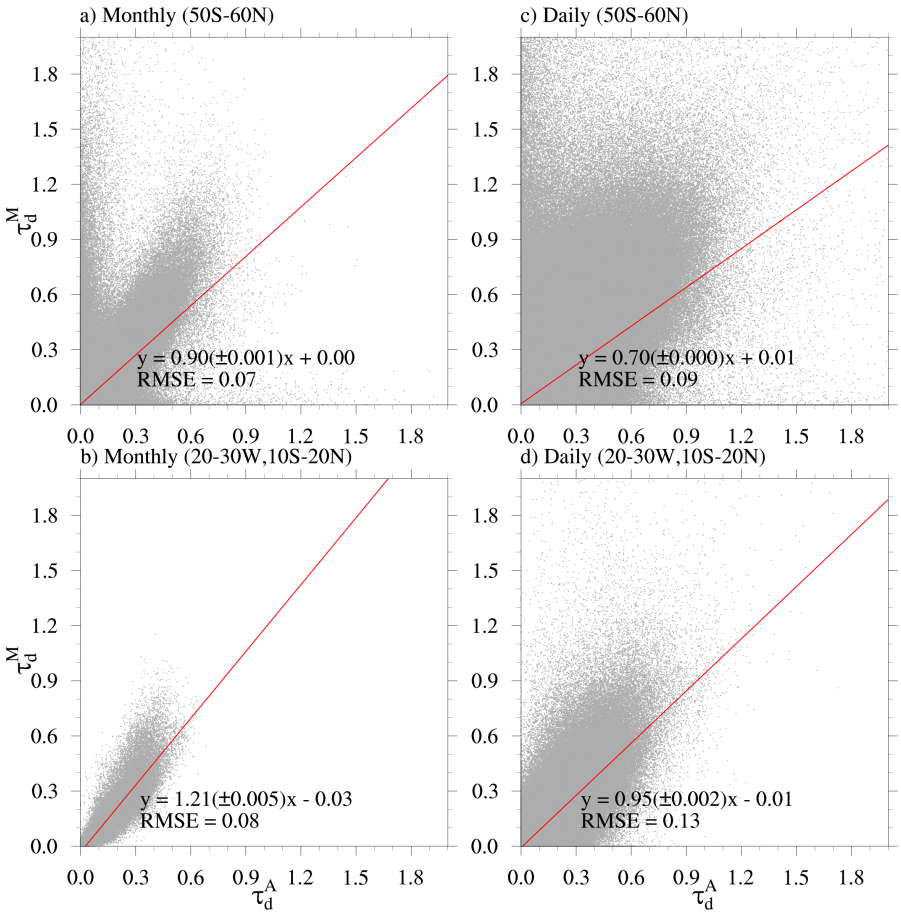

Figure 2.4: Scatterplots of daily (a, c) and monthly mean (b, d) τ_d^M and τ_d^A, for 60°S to 60°N (a, b), and for a region over the tropical Atlantic where dust storms are frequent $(5°S\text{-}20°N,\ 20-30°W)$ (c, d), all for the period 2001–2017. The solid red lines represent the linear least-squares regression, and the corresponding slopes and offsets are indicated in each figure panel, as are RMSE.

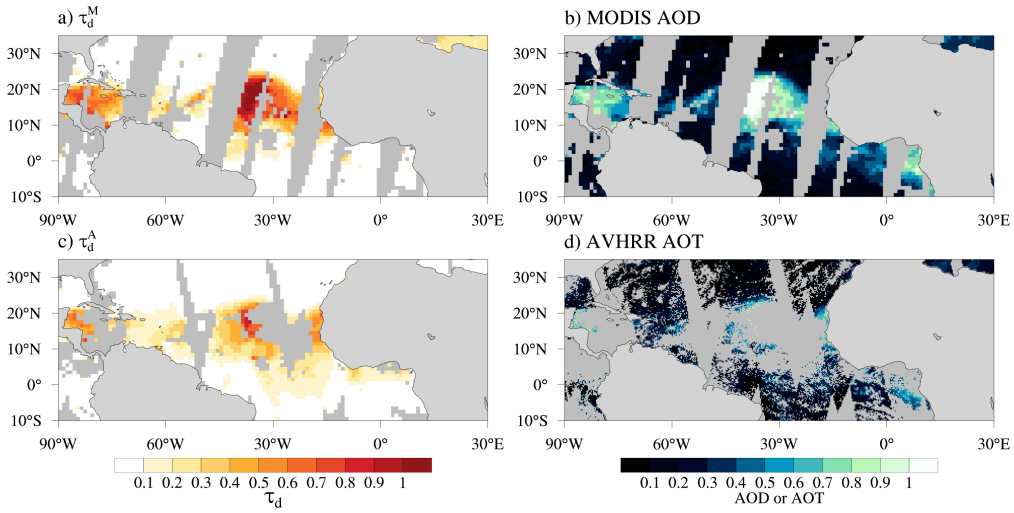

Figure 2.5: June 27th, 2014 *a*) τ_d^M and *b*) MODIS AOD from the Terra platform and *c*) τ_d^A and *d*) AVHRR AOT. Retrievals and estimates over land and locations where there is missing data are shown in grey.

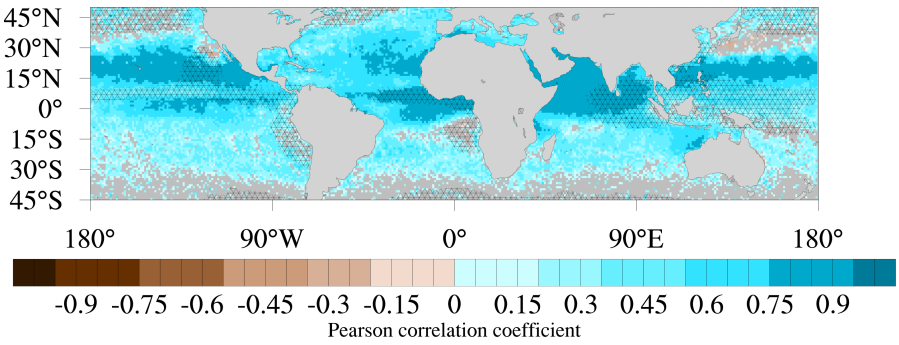

Figure 2.6: Pearson correlation coefficient between monthly τ_d^M and monthly τ_d^A from 2001 to 2017 with the seasonal cycle removed. Regions where the correlation is not significant at the 95% confidence level are masked. Hatched areas indicate locations where daily matched observations from AVHRR and MODIS Terra are present for fewer than 50% of days in the period 2001 to 2017.

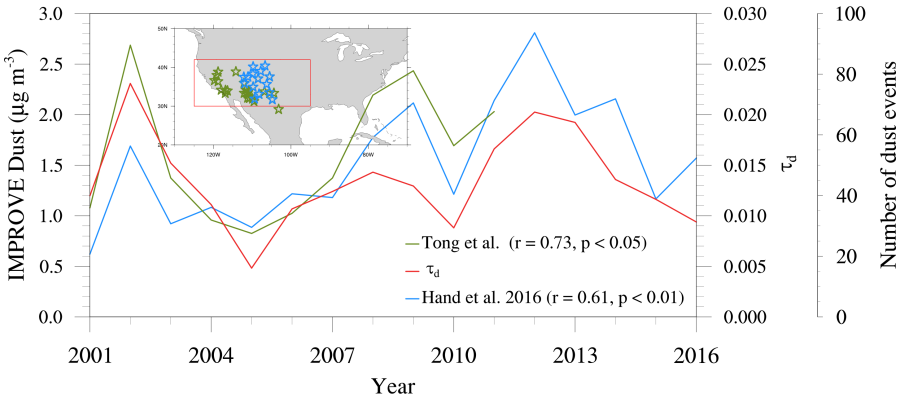

Figure 2.7: Annual mean τ_d^M from land grid points in the Southwestern United States within the region shown in the red box (30-42°N,125-95°W), compared with number of dust events annually in the southwestern U.S. as reported in Tong et al. (2017) (green) and dust concentration from IMPROVE sites in the southwestern U.S. as reported in Hand et al. (2016) (blue). IMPROVE stations used in the Tong et al. (2017) analysis are marked with green stars on the inset map, while stations used in the Hand et al. (2016) analysis are marked with blue stars. There are several overlapping stations. The r-value and p-value of the correlation between t_d^M from Terra and each other time series is shown in the figure legend.

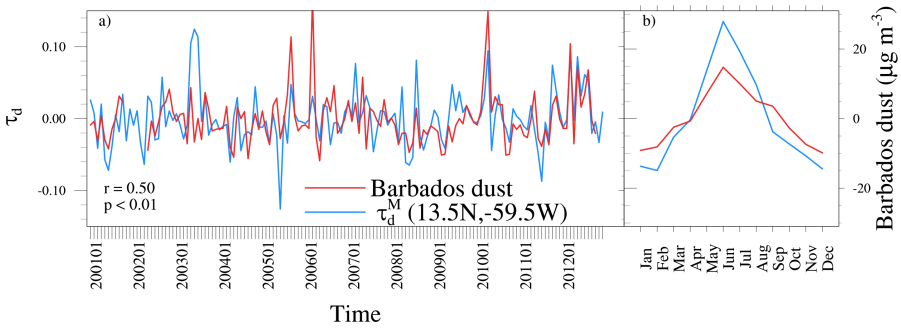

Figure 2.8: *a*) Time series of monthly mean ground based dust aerosol measurements on Barbados (red) compared with τ_d^M over Barbados (blue), each with the seasonal cycle removed. *b*) Climatological monthly mean, with long-term mean removed, of measurements on Barbados (red) and of τ_d^M over Barbados (blue). The r-value and p-value for the correlation between these time series is shown in the bottom left hand corner.

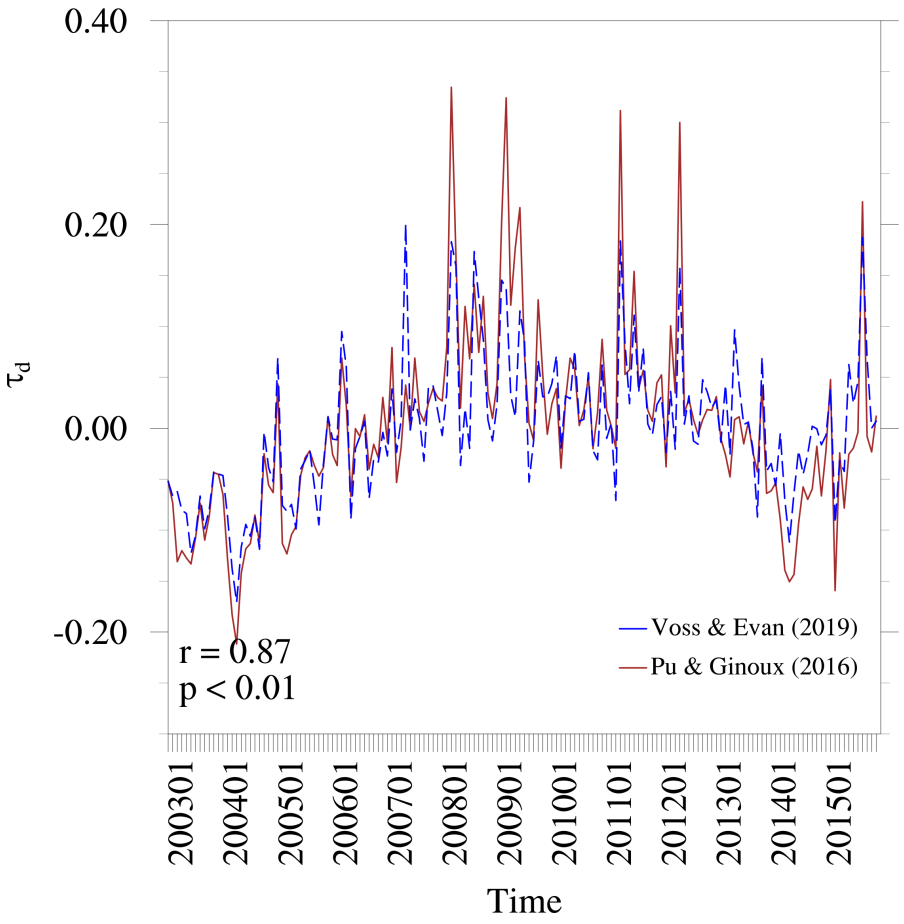

Figure 2.9: Time series of monthly mean dust optical depth (brown) compared with τ_d^M (blue) over Syria ($34 - 36.5°$N and $36.5 - 41°$E) each with the seasonal cycle removed. The r-value and p-value for the correlation between these time series is shown in the left hand bottom corner.

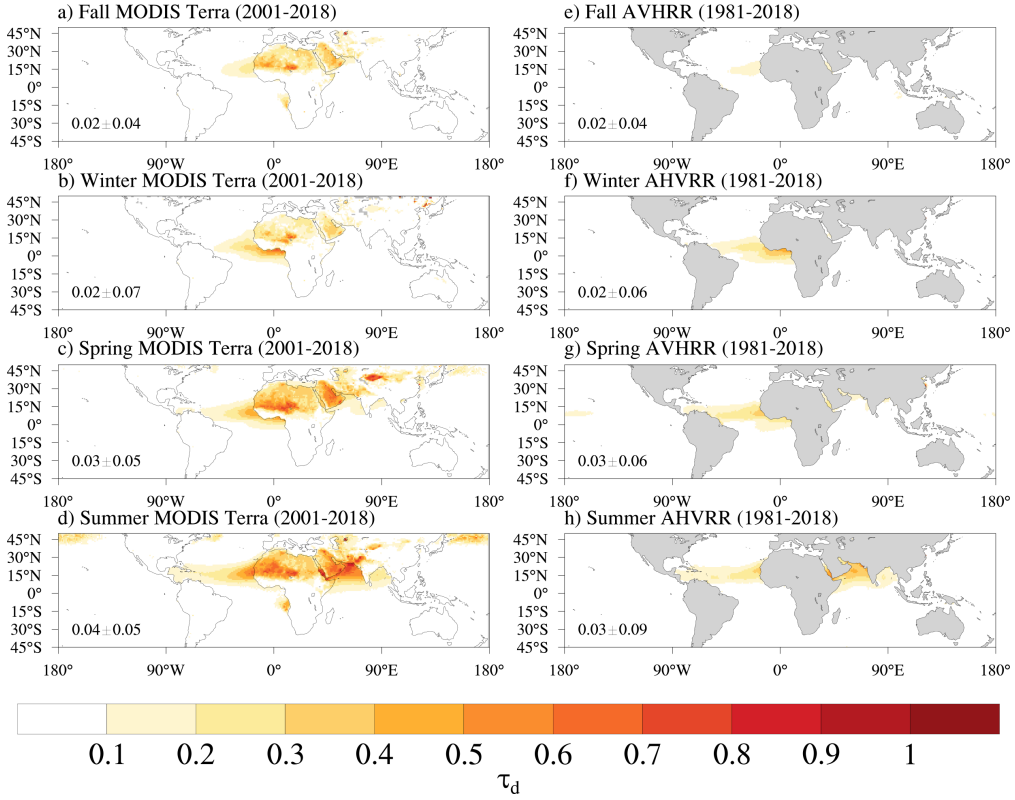

Figure 2.10: Seasonal mean $a-d)$ τ_d^M averaged over the period from 2001 to 2018 and $e-h)$ τ_d^A over the period from 1981 to 2018. The long-term global mean $\tau_d \pm 1\sigma$ uncertainty over the ocean for each season and dataset is featured in the bottom left-hand corner of each panel.

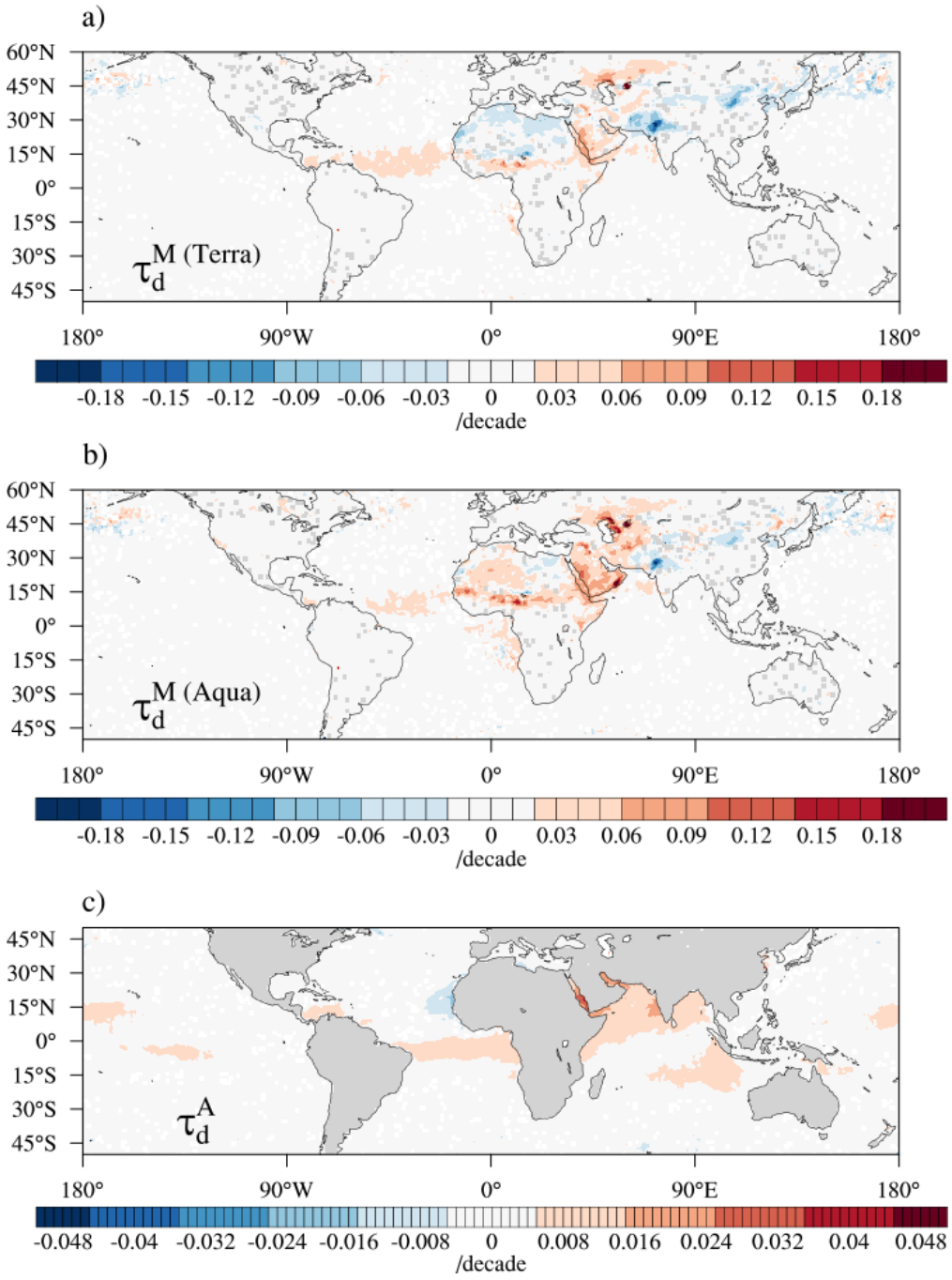

Figure 2.11: Trend in $a)\tau_d^M$ Terra (2001-2018), $b)\tau_d^M$ Aqua (2003-2018) and $c)\tau_d^A$ (1981-2018) with the seasonal cycle removed. Only trends that are significant at the 95% confidence level are shown.

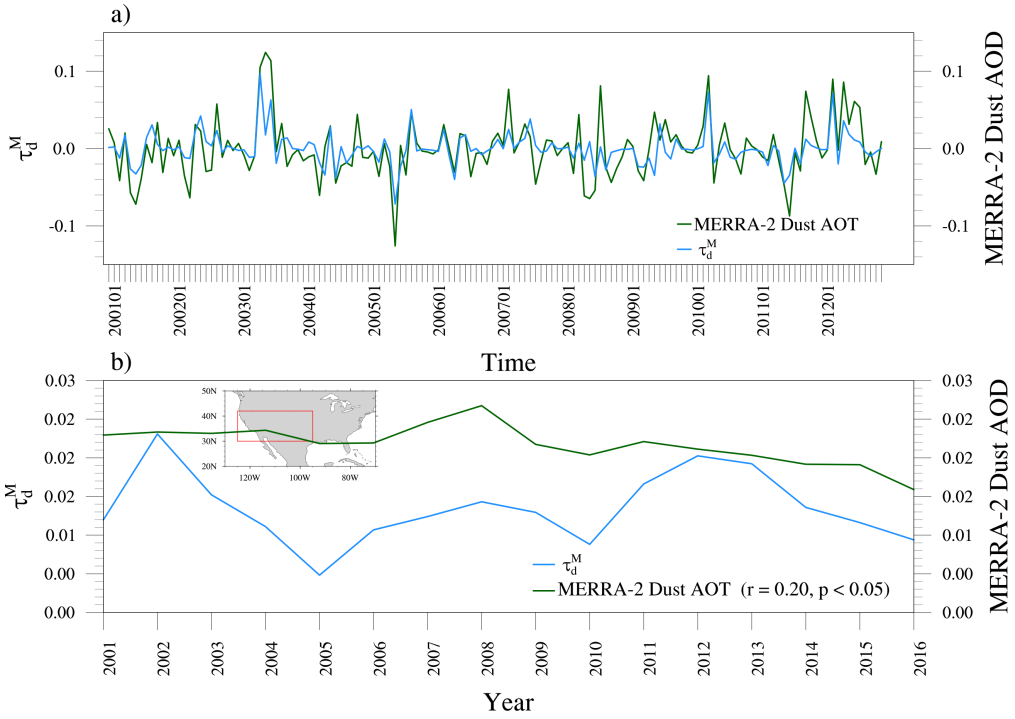

Figure 2.12: *a*) Monthly MERRA-2 dust extinction aerosol optical thickness at 550nm and monthly mean τ_d^M over Ragged Point, Barbados between 2001 and 2013 with the seasonal cycle removed. *b*) Annual mean MERRA-2 dust extinction aerosol optical thickness at 500nm and annual mean τ_d^M over the southwestern U.S. from 2001 to 2016.

Chapter 3

Dusty Atmospheric Rivers: Characteristics and Origins

3.1 Chapter Abstract

Atmospheric Rivers (AR) are narrow bands of strong horizontal transport of water vapor in the mid-latitudes that can cause extreme precipitation, which contributes to beneficial water supply and sometimes flooding. The precipitation productivity of an AR is affected by microphysical processes, including the influence of aerosols. Earlier case studies have shown that some ARs over the North Pacific contain dust from Africa and Asia that can strongly influence precipitation by acting as ice nuclei. This paper explores how commonly dust and ARs occur together, or in close proximity. A "dust score" is introduced to characterize the dustiness of the environment associated with ARs using satellite-based observations. This method is applied to days on which one or more ARs made landfall along the west coast of the U.S. between 2001 and 2018. The dust score is used to describe the seasonality and year-to-year variability of dusty-environment ARs. Dusty ARs occur primarily in the early spring (March-April) and dust is preferentially found within the warm sector of AR-associated extra-tropical cyclones but is also enhanced in the cold sector. Year-to-year variability in dust score is dependent more on year-to-year variability in dust than on the frequency of AR days.

This year-to-year variability is also strongly related to correlations between the frequency of ARs and the dustiness of the northeastern Pacific, motivating additional investigation into potential dynamical association between dust and ARs.

3.2 Introduction

Atmospheric Rivers (ARs) are narrow corridors of water vapor, usually associated with an extra-tropical cyclone, that transport moisture in the lower troposphere and typically contain a low-level jet (Ralph et al., 2018; Zhu and Newell, 1998; Ralph et al., 2004, 2005; Waliser and Guan, 2017; Dettinger et al., 2011; Lamjiri et al., 2017). They are the primary mechanism for transport of moisture from the tropics to the mid-latitudes (Zhu and Newell, 1998), and are responsible for 20-50% of annual precipitation in California (Dettinger et al., 2011). The CalWater Field campaign, beginning with the CalWater Early-Start in 2009 in Northern California (Ault et al., 2011; Ralph et al., 2016) brought meteorologists and atmospheric chemists together to understand and better predict the meteorological and aerosol chemical controls on precipitation from California's landfalling ARs. A major finding of the CalWater field campaigns was that dust, transported from Asia and Africa, can sometimes be found within the ARs making landfall in Northern California (Ault et al., 2011; Creamean et al., 2013, 2014, 2015, 2016).

In the troposphere, homogeneous freezing, freezing of pure liquid water, occurs at temperatures lower than $-38°C$ and relative humidity with respect to ice above 140% (Hoose and Mhler, 2012). Freezing at warmer temperatures requires heterogeneous nucleation through the presence of an aerosol acting as an ice nucleating particle (INP). The temperature at which an INP "activates", or catalyzes freezing, depends on it's chemical composition, particle size and the external conditions. Dust is known to be a relatively warm ice nucleating particle, forming ice at temperatures less than $-15°C$. Dust is sometimes described as the most important INP (**?**) because it is efficient, since it nucleates at a warmer temperature than most other particles (Hoose and Mhler, 2012), and because it is abundant due to its a high emission rate (**?**).

Microphysical observations from CalWater have indicated that trans-Pacific dust causes cloud glaciation in mixed-phase clouds and potentially enhances precipitation by acting as ice nucleating particles (INP) (Creamean et al., 2013; Ault et al., 2011; Martin et al., 2019; Creamean et al., 2016, 2015). Ault et al. (2011), in a comparison of two meteorologically similar AR events, one with and one without dust, found that dust INPs may have have enhanced storm-total precipitation by up to 40%. Creamean et al. (2013) found long-range transported dust layers in clouds coincident with enhanced ice fraction at relatively warm temperatures and Creamean et al. (2015) found that dust and biological particle residues were commonly associated with deep convective clouds with large quantities of precipitation that had been initiated in the ice phase. Given that long-range transported dust from Asia and Africa accounts for a significant portion of dust in the Western U.S. with a seasonal maximum in the Spring (Creamean et al., 2014; VanCuren, 2002; Yu et al., 2012), dust may regularly be an important modulator of AR precipitation.

Although these in-situ observational studies have found results consistent with trans-Pacific dust acting as precipitation enhancing INP, there are, in general, very few measurements of dust during ARs. The limited availability of dust measurements has hindered progress in understanding the role of dust in these events. In this work, we build upon the findings of the CalWater field studies by using a new 18-year record of dust aerosol optical depth (τ_d) from Voss and Evan (2019), thereafter VE19, to create a climatology of ARs in dusty environments through the development of a "dust-score". We use this dust score climatology to investigate the seasonal and inter-annual variability of dusty-environment ARs, the drivers of this variability, and the position of dust relative to AR-associated extra-tropical cyclones.

The remainder of this paper is organized as follows: In the Data section, we describe the various datasets used throughout the analysis. In the Methods section, we describe the calculation of the dust score. In the Results section we describe a case study of an AR in a dusty Pacific environment, followed by an analysis of the location of dust relative to extra-tropical cyclones and we describe the seasonality

and year-to-year variability in the frequency of ARs in dusty environments. We finish the Results section with a decomposition of sources of year-to-year variability in the dust score. We conclude with a description of the limitations of the dust score and a summary of our results.

3.3 Methods

An AR dust score is calculated for every AR day, defined as any day on which an AR was making landfall along the U.S. West Coast, between 2001 and 2018 (Eq 4.2). The AR dust score is calculated from the average of τ_d within the boundaries of an AR feature as identified in the Rutz catalogue only for over-ocean grid cells that fell within a domain that contained the entire U.S. west coast and extended towards the central Pacific to a distance that reflects the approximate length scale (1800km) of a wintertime North Pacific extra-tropical cyclone (Rudeva and Gulev, 2007) $145 - 116°W, 32 - 49°N$ (Fig 3.3). The probability of the presence of an AR at any 1° x 1° grid cell on a given day can be defined as a, which in this case is always 0 or 1. This can be divided by the total number of grid cells that have a probability of 1 to yield the probability of an AR at a given grid cell normalized by the size of the AR, which we will define as A.

$$A = \frac{a}{\sum_{n=1}^{N} a} \tag{3.1}$$

Where n is a $1°x1°$ grid cell in the binary map of AR and N is the total number of non-missing value pixels on a given day. Then, the dust score (S) can be expressed as

$$S = \sum_{n=1}^{N} (\tau_d \cdot A) \tag{3.2}$$

Atmospheric Rivers along the U.S. west coast typically have moisture transport from the southwest to the northeast with an upper level and lower level jet (Ralph et al., 2017). These southwesterly winds make it unlikely that dust from North American sources will flow westward towards the vicinity of ARs over the Pacific on the day of an AR. It is possible that dust from North American sources may

still be advected into the vicinity of an AR over the Pacific, for example, if offshore winds moved it out into the Pacific in the days preceding an AR event. In this case, this dust would impact the dust score. As a conservative measure, dust (τ_d) over land or within one degree longitude of land is excluded from the average of τ_d used to calculate the dust score.

For AR days between 2001 and 2018, the median dust score was 0.015, the 75th and 25th percentile dust scores were 0.034 and 0.004, respectively, and the maximum and minimum dust scores were 0.304 and 0, respectively (Fig 3.4). The mean dust score is 0.026 ± 0.024 where 0.024 is the $1 - \sigma$ uncertainty from the τ_d estimates used in its calculation.

There are several limitations to the AR dust score presented here. We calculate a new dust score for each AR day rather a single score for each AR event. This may lead to longer duration AR events having greater influence on our climatological analysis of the seasonality and inter-annual variability of ARs in dusty environments. We chose to group by AR day rather than AR event because we needed a record that spanned the temporal length of the τ_d record (2001-2018), and we did not have a record of AR event objects for the entirety of that period. Our method of calculation of dust score uses a binary map that does not discriminate between AR events. Any grid cell with a τ_d estimate that is also the location of an AR feature in the Rutz catalogue will be used in the dust score calculation. It is possible that multiple AR objects could be present within the domain on a given day. According to our method, these would be combined in the dust score for that day. Additionally, τ_d estimates are only available in clear sky pixels. Dust that is present within, above, or below clouds will not be counted in the dust score. Therefore, any dust that is activated as CCN or IN will not be counted in the dust score. It is plausible that an AR day could have substantial dust within, above, or below cloud and still have a low dust score.

In order to evaluate the effect of missing data, due to clouds cover an sun glint, on the dust score a simple test was performed. Dust scores were calculated for every AR in the same manner as has been described above, except using MERRA-2 dust extinction optical depth interpolated to the same grid as τ_d (1°x1°). MERRA-

2 dust extinction optical depth, while not independent from τ_d because MODIS AOD is assimilated into the re-analysis, does not have missing data due to clouds or sun glint. Dust scores were calculated from MERRA-2 dust extinction optical depth in two ways: 1) using all available pixels within the AR, and 2) sub-sampled such that data is missing in the same locations/days that is missing for τ_d. This is similar to what has been done previously to evaluate clear sky biases over ocean for MODIS AOD (Zhang and Reid, 2009). These two scores were then compared using a student t-test. The average dust score from MERRA-2 calculated from all available pixels was found to be 0.019 ± 0.017 and the average dust score when sampled the same as τ_d was found to be 0.019 ± 0.018. These differences are not significant ($p = 0.98$), suggesting that the dust score is, on average, not sensitive to missing data due to cloud cover and sun-glint.

3.4 Results

3.4.1 Case study

In order to understand how dust can be transported from continental sources across the Pacific to potentially impact an AR, we present a case study of an AR that made landfall along the U.S. west coast with dust in it's vicinity on March 29th, 2010. This case was chosen as an example because it had very good coverage of τ_d over the Pacific ocean on the date of the AR landfall, and a high score (0.064). On March 29th, this AR had reached the U.S. west coast between 36°N and 49°N, with the highest IVT near 42°N, 121°W. Ten days prior to this event, major dust lofting events occurred over both the Gobi Desert (near 42°N, 95°E; red arrow in Fig 3.6a) and the Taklamakan desert (near 38°N, 80°E; blue arrow in Fig 3.6a) in Asia. Lofted dust can clearly be seen in the MODIS Terra Visible Imagery on March 19, 2010 (Fig 3.5a) and is evidenced by high τ_d over this region on the same date (Fig 3.5b). Kurosaki and Mikami (2007) found the threshold wind speed at the normal land surface for dust emission over the Taklamakan Desert to be 6.7 ± 1.5 m s^{-1}. Over the Gobi Desert, this threshold for dust emission is greater, 13.8 ± 2.0 m s^{-1}. MERRA-2, hourly surface wind speeds over both deserts show

peaks in velocity on March 19, 2010, with velocities exceeding 9 m s^{-1} over the Taklamakan (Fig 3.5c) and 18 m s^{-1} over the Gobi (Fig 3.5d) suggesting conditions favorable for dust emission. The approximate overpass time of MODIS Terra is indicated with a red line. A secondary peak in wind speed is present over both deserts on March 21st, leading to another dust event. These high wind speeds, westerly over the Taklamakan desert and northeasterly over the Gobi desert are also shown in the blue 10-meter wind vectors in Figure 3.5b, consistent with the conditions found favorable for dust lofting over Asian deserts as described in Sun et al. (2001).

On March 18, 2010, one day prior to this dust event, there are few pixels over Asia with τ_d greater than 0.5 (Fig 3.6a). The plume of high dust concentrations, as evidenced by the τ_d values greater than 0.7, is initially present near 42°N, 95°E on March 19, 2010 (Fig 3.6b). After initial lofting, the plume was transported eastward passing eastern Beijing $(40°N, 116°E)$ on March 20,2010 (Fig 3.6c). By March 21, 2019, the plume reached the Asian coast and the Pacific Ocean near 27°N, 122°E (Fig 3.6d). On March 22, 2019, the plume appears elongated from $122 - 160$°E (Fig 3.6e). While a region of missing data, due to the effects of sun glint, prevents visualization, the continuity of the plume on this date was confirmed through use of visible imagery. The CALIPSO Verticle Feature Mask (VFM) classification indicated the presence of dust between 2 and 7km from $25 - 35$°N along a transect near 150°E (Fig 3.7). In Figure 3.6, 500hPa geopotential height contours (blue) are aligned with this westward transport of dust. On March 24, 2019 (Fig 3.6g), the plume had reached 180°E, extending across much of the Pacific Ocean, while partially obscured by cloud cover and sun glint. From March 25 to March 28, dispersion of the plume and cloud cover prevent discrimination of the movement of the plume (Fig 3.6h-k) but there are still broad regions of enhanced τ_d.

On March 29, 2010 at 18:00UTC, as shown in the Climate Forecast System version 2 reanalysis, an upper level trough that approached from the southwest was present near 50°N, 145°W (Fig 3.1). The downstream side of a cyclonically curved upper-level (250hPa) jet was located over Oregon and Washington with

a $> 50\text{ms}^{-1}$ jet streak exit region. An occluded front extended from the low pressure center and the southern half of the cold front was parallel to the jet exit region. Vectors of IVT (black arrows) show transport of water vapor south of the upper level jet and along the northern edge of the region of high (> 15 kg m^{-2}) precipitable water. Daily total precipitation at 4km from PRISM, as shown in the filled blue contours over land in Figure 3.2, indicate that greater than two inches of precipitation fell in most coastal areas of Oregon and Washington on this date with a maximum at 44.9°N, 123.6°W in Polk County, OR where greater than 4.45 inches of precipitation fell. Moisture, evidenced by precipitable water greater than 15 kg m^{-2}, west of 140°W and south of 40°N was transported towards the northeast as an elongated plume with MERRA-2 IVT greater than 250 kg m^{-1}s^{-1} and greater than 2000km in length, meeting the criteria to be classified as an AR from Rutz et al. (2014) (Fig 3.2).

An elongated region of enhanced τ_d was found coincident with an the AR, visible within the horizontal boundaries of AR and along it's edges. The enhanced τ_d appears west of the region of highest IVT. While we cannot infer the altitude of the dust from τ_d, CALIPSO VFM classification on March 29, 2010 at 11:22UTC (Fig 3.8) corroborates the presence of dust near $30 - 40$°N and $145 - 140$°W and shows that dust was present within the lowest two kilometers of the troposphere. Dust is also present during this observation between four and six kilometers.

In order to further understand the transport path of trans-Pacific dust for this event, HYSPLIT (Draxler and Rolph, 2011) air mass forward trajectories were conducted from the source regions of Asia, the Taklamakan and Gobi deserts. National Centers for Environmental Prediction/National Center for Atmospheric Researcher (NCEP/NCAR) reanalysis wind fields were used as input (Kalnay et al., 1996). Forward trajectories were initiated at matrix of grid points over the Talamakan for 12 day trajectories. Sixty-five trajectories were released on March 19 18:00 UTC from 1 degree spaced grid points from $36 - 40$°N, $37 - 78$°E at an altitude of 2km. These are air mass trajectories and, as such, they do not include processes such as wet or dry removal, and convective transport which may affect dust transport. All of these trajectories traveled west and 67% reached the longitude 128°W, along or

near North American West Coast, within the 12 days. A matrix of 32 forward trajectories were released from the Gobi desert between $39-42$°N, $100-107$°E at 1° spacing at the same altitude and time as from the Taklamakan. 37% of these trajectories traveled west and reached 128°W within 12 days. Those trajectories that extend across the Pacific remain primarily confined between $30-45$°N between 135°E and 150°W. However, west of 150°W trajectories from both deserts diverge into two branches. The northern branch reaches the North American coast over western Canada and the southernmost part of Alaska (approximately 50°N). The southern branch reaches the North American coast between Oregon, near 40°N, and Northern Baja California, Mexico, near 27°N.

This transport pathway for Taklamakan and Gobi desert dust reaching North America is consistent with previous studies, including Yu et al. (2019) in which the patterns of long-range transport of Asian dust were studied using the Multi-angle Imaging SpectroRadiometer (MISR) instrument combined with observation-initiated trajectory modeling. Yu et al. (2019) found that while the potential for trans-Pacific transport to North America peaks in the springtime for both deserts, Taklamakan dust exhibits higher potential for long-range transport and reaches a larger range of latitudes along the west coast of the U.S. than Gobi desert dust. This is due to higher injection heights over the source region and mid- to low-level ascending air in the spring and summer. Taklamakan dust exhibits greater influence over North America for latitudes south of 50°N while Gobi dust exhibits greater influence for latitudes north of 50°N. However, both deserts exhibit influence over North America at 40°N, the approximate latitude of landfall of the AR on March 29, 2010. It is notable that in Yu et al. (2019) only 5% of trajectories released during springtime from the Taklamakan and Gobi deserts passed over North America. As previously mentioned, in our analysis 67% and 37% of trajectories from the Taklamakan and Gobi deserts, respectively, released on March 19, 2010 reached 128°W indicating particularly favorable meteorology for long-range transport in our case study. It is also plausible that dust originating from other sources farther west, such as North Africa or the Middle East, mixed with Asian dust and traveled westward reaching the North American coast (Hu et al., 2019).

For this case of an AR in a dusty environment that made landfall on March 29, 2010 we have shown that dust can be lofted from Asian deserts and transport over the western Pacific to impact the environment surrounding an AR, even in the lowest 2km near to where the low level jet resides. While cloud cover and sun glint prevented discrimination of dust in parts of the eastern Pacific, dust, as evidenced by high τ_d was clearly present within the boundaries of the AR feature. The AR dust-score for this event was 0.064, which is within the top 10 percent of AR dust scores for AR days between 2001 and 2018.

3.4.2 Composite analysis

We have shown through a case study that trans-Pacific dust can reach the eastern North Pacific and appear in the vicinity of an AR. However, is dust within such a system spatially randomly distributed or is dust preferentially concentrated in a specific location relative to the AR? Answering this question may help us to understand the mechanism through which dust may come into contact with an AR. While cloud-cover prevents us from robustly investigating the position of dust within, above, or below an AR we are able to investigate the position of dust relative to the center of AR-associated ECs.

Zhang et al. (2019) found that 82% of Atmospheric Rivers are associated with an extra-tropical cyclone (EC), although it should be noted that the distance between the AR and the EC center varies greatly. Examples of the position of an AR relative to an extra-tropical cyclone are shown in Figures 3.3 and 3.1. These examples are not representative of all cases. We created an EC-centric composite of τ_d using EC center locations for the cool seasons (Nov-Mar) from Jan 2001 to March 2010 for ECs identified in Zhang et al. (2019) to be associated with an AR (Figure 3.10a). For each AR-associated EC in the record we composited τ_d within 15 degrees latitude and longitude of the low-pressure center. The conclusions of this section remain the same when the distance from EC center used in the average ranges from 5 to 15 degrees. We then selected only the ECs with average τ_d in the top 10th percentile to composite. We also show in Figure 3.10b the number of pixels (N) used at each grid cell for the composite shown in Figure 3.10a, ie.

the number of non-missing values. Missing data in τ_d may occur due to cloud cover or sun glint. Data may also be limited in cases where the EC center is near to the northern edge of the domain of the τ_d dataset ($55°N$) or near to land. In both panels, contours of sea level pressure (dashed black lines) and AR probability (solid black lines) are shown. We found that τ_d was generally highest nearest in the warm sector of the extra-tropical cyclone, east of the EC center. Dust was also enhanced in the southwestern quadrant of the EC, which is roughly the location of the EC cold sector (Fig 3.10a). The cold sector of the extra-tropical cyclone is the area within the circulation where cold air, advected from higher latitudes, can be found (American Meteorological Society, cited 2020). It typically lies behind the cold front. The regions of highest mean τ_d appear northeast and within the highest AR probabilities, and east and south of the low pressure center. The region of highest mean τ_d has fewer pixels used in the composite, due to cloud cover and because this section fo the cyclone is most likely to be over land where τ_d is excluded from the composite. It is possible that cloud contamination in the AOD retrievals used in the calculation of τ_d could be more prevalent in this region than in other parts of the EC and could therefore appear as an enhancement of mean τ_d in this region. In order to test whether this was the case, we created the same composite but replaced any τ_d with a missing value wherever MODIS Terra daily cloud fraction was greater than 60% (Fig S2). While this substantially decreased our sample size and decreased τ_d in the composite overall, the spatial pattern remained qualitatively the same. The same result was found when other cloud fraction thresholds were used, but when thresholds of 50% or less were used there were not enough τ_d estimates remaining for a thorough analysis. Naud et al. (2016), in making cyclone-centered composites of MODIS AOD, found that when only Northern Hemisphere (NH) ECs with less than 80% cloud cover were used in a composite, the mean AOD was lower but the spatial pattern remained the same compared to when all NH EC were considered, consistent with our result. Therefore, we do not expect the enhancement of dust in the warm sector of the EC composite to be an artifact of cloud contamination.

Creamean et al. (2013) found that post-cold front precipitation was more enriched in dust and biological residues, the particles that remain after water is evaporated from precipitation samples, than in pre-frontal or peak AR conditions. Both Ault et al. (2011) and Creamean et al. (2013) found that all of the atmospheric rivers sampled and analyzed during the CalWater Field campaign in which dust residues were dominant had meteorological conditions corresponding to the passage of a cold front. Likewise, VanCuren (2002) observed short Asian dust events along the U.S. West Coast at sea level in Inter-agency Monitoring of Protected Visual Environments (IMPROVE) measurements, but only during strong frontal passages. These previous observations could have indicated either an enhancement of dust in the post-cold frontal region of the extra-tropical cyclone, or more efficient removal, through activation or deposition, of dust in post cold-frontal conditions.

3.4.3 Seasonality and inter-annual variability

We now aim to answer the question: When do these dusty-environment ARs occur seasonally and how often do they occur annually? Previous published studies have found that sources of trans-Pacific dust include deserts in Asia, North Africa, and the Middle East (Hu et al., 2019) and transport of dust across the Pacific occurs primarily in the springtime, when westerlies are strong but precipitation is weaker than winter (Creamean et al., 2014; Hu et al., 2019). Dust emission over the deserts of Asia has a seasonality with a maximum in the springtime (MAM), as evidenced by high τ_d over the region ($35-45$°N, $78-110$°E) in March, April, and May (Fig 3.12a), and modeling efforts have suggested that trans-Pacific transport from other dust sources also peaks in the spring Hu et al. (2019). However, the season for ARs reaching the west coast of the U.S. is primarily from October to March, as shown through the mean number of AR days per month (Fig 3.12b). In each month between October and March, there are greater than 9 AR days on average. In order to understand how the seasonality of dust and ARs impact the seasonality of ARs in dusty environments, we have grouped AR events by the percentile group of their dust score. By this method, AR days that have a dust

score that is greater or equal to the $50th$ percentile dust score fall into the $50th$ percentile group. AR days that have a dust score that is greater than or equal to the $75th$ percentile dust score fall into the $75th$ percentile dust score group, but are also counted within the $50th$ percentile group, and so forth. We then count the number of AR days that are within each group for each month and divide by the number of years of data (2001-2018) to show the average number of AR days per month within each percentile group (Fig 3.11). Most ARs occur between October and March (black line) (Rutz et al., 2014). However, as the percentile group of AR dust score increases, the number of AR days in the months of October through February decreases much more than the number of AR days in March and April. AR days within the $95th$ percentile dust score (orange line) almost exclusively occur between February and May. For each dust score, the percentage of pixels with τ_d estimates relative to the total possible pixels in the 2-dimensional AR was calculated ie. the data availability. It was found that the seasonality did not change qualitatively when dust scores with data availability below specific thresholds (10%, 20%) were excluded from the analysis. This highlights that the seasonal cycle of ARs in dusty environments includes a maximum in the early springtime, at the confluence of the AR season and the trans-Pacific dust season.

In order to understand how variable the dust score is from year-to-year, we calculated the water-year mean dust score (Fig 3.13a). A water-year begins October 1st and ends on September 1st and is designated according to the calendar year in which it ends. The maximum in water-year mean dust score, 0.033, occurs in 2018 and the minimum, 0.018, occurs in 2004. The average dust score for the water-years 2002 to 2018 was 0.026. The standard deviation of the water-year mean dust score, 0.004, is 16% of the mean. The water-years 2007, 2012 and 2017 also stand out with an annual mean dust score of 0.033, 0.031 and 0.028, respectively. There is no statistically significant trend in the water-year mean dust score.

Having found that there is inter-annual variability in the water-year annual mean dust score, we now aim to understand the source of this variability. Is it due to changes in dust, changes in the number of ARs hitting the west coast of the U.S., or correlated changes in both of these factors? We address this question

Table 3.1: Variance of each term in Equation 3.8 as a percentage of the sum of the variance of these terms. $\overline{\tau_d}\overline{A}$ represents the contribution of the climatological mean and seasonal cycles of dust and ARs to the variance in dust score. $\tau_d'\overline{A}$ represents the contribution from independent changes in dust, while $\overline{\tau_d}A'$ represents the contribution from independent changes in the location of ARs in space and time. $\tau_d'A'$ represents the contribution from correlated changes in dust and the location of ARs in space and time.

$\overline{\tau_d}\overline{A}$	$\tau_d'\overline{A}$	$\overline{\tau_d}A'$	$\tau_d'A'$
13%	40%	5%	41%

by performing a Reynolds decomposition on the time series of the annual AR dust score. The time series of dust score can be expressed as

$$S = \tau_d \cdot A \tag{3.3}$$

Where τ_d and A are a function of space and time and therefore S is also a function of space and time. We can then use a Reynolds Decomposition to define the mean and time varying components of τ_d and A. For example, the mean A is given by

$$\overline{A} = \lim_{T\to\infty}(\frac{1}{T}\int_0^T A dt) \tag{3.4}$$

such that the time varying component is defined as

$$A' = A - \overline{A} \tag{3.5}$$

and then

$$A = \overline{A} + A' \tag{3.6}$$

If we similarly decompose τ_d, then S is

$$S = (\overline{\tau_d} + \tau_d') \cdot (\overline{A} + A') \tag{3.7}$$

or

$$S = \overline{\tau_d}\overline{A} + \tau_d'\overline{A} + \overline{\tau_d}A' + \tau_d'A' \tag{3.8}$$

The four terms on the right hand side in Equation (3.8) are, from left to right:

1. The long term mean of S, which includes the seasonal cycle

2. The contribution to S from changes only in τ_d
3. The contribution to S from changes only in A
4. The contribution to S from correlated changes in τ_d and A.

From Equation (3.8), the total variance in the dust score (S) can be approximated as the sum of the variances from each term plus the co-variance between the terms. The contribution of each of these terms to the total variance in the dust score can be used to understand the sources of inter-annual variability in the dust score. It must be noted that these terms are not completely independent, the correlation between each of the terms is non-zero, resulting in non-linearity. Each of the co-variance terms amount to less than 10% of the variance in dust score. We will excludes these small terms from the rest of our analysis in order to focus on the physically meaningful terms that explain more of the variance.

The sum of the variance of the first four terms in Equation 3.8 account for 69% of the variance in the dust score. In Equation 3.8, if τ_d never had missing values then the annual mean $\overline{\tau_d}\overline{AR}$ would be constant from year to year. However, given that τ_d is missing at some locations in space and time, when any right hand side term is missing S is missing as well. If you were to calculate the annual mean of each of the right hand side terms separately and add them, the only way you will get the same annual mean S is if you sample each right hand side term in space and time only where there are values for term. This means that the annual mean $\overline{\tau_d}\overline{AR}$ will vary from year because the location and number of missing values for all the other terms are different from year to year. Therefore, in Equation 3.8, $\overline{\tau_d}\overline{AR}$, which represents the contribution of correlated seasonal variations of dust and ARs, is at a maximum in 2016 and is at a minimum in 2002 (Fig 3.13b). $\overline{\tau_d}\overline{AR}$ contributes 13% of the variance of those terms (Table 3.1). In Equation 3.8, $\overline{\tau_d}A'$, which represents the contribution of independent changes in the location in space and time of ARs making landfall along the west coast of the U.S., is at a maximum in 2007 and is at a minimum in 2016 (Fig 3.13c). In Equation 3.8, $\tau_d'\overline{A}$, which represents the contribution to the dust score from independent changes in dust, is at a maximum in 2007 and is at a minimum in 2015 (Fig 3.13d). This aligns with the maximum in the dust score. Independent changes in dust contributed

43% to the variance of the dust score (Table 3.1). $\overline{\tau_d}A'$ contributes only 5% to the variance in the dust score (Table 3.1). The higher contribution of $\overline{\tau_d}A'$ than $\tau_d'\overline{A}$ to the variance of the dust score highlights that variability in background dust may be more important for the dust score than variation in ARs. Correlated perturbations in dust and AR feature position contributed 41% of the variance in dust score and are at a maximum in 2018 and a minimum in 2014 (Table 3.1; Fig 3.13e). These correlated perturbations indicate that there may be a dynamical relationship between dust and ARs.

Missing data in τ_d, due to cloud cover or sun glint, may impact the variance budget described in equation 3.8. In order to test whether missing data would impact our conclusions, we performed two additional tests by filling the gaps in τ_d with the long-term (2001-2018) daily mean of τ_d and, secondarily, filling the gaps with zeros. Filling gaps with the long term mean τ_d resulted in an increase of the contribution of the $\overline{\tau_d}\overline{A}$ to the variance, but did not otherwise change our conclusions. Filling the gaps in τ_d also did not change our conclusions, as the relative magnitudes of the contribution of each term to the variance was the same as when gaps were unfilled.

In the calculation of the dust score for each AR day, we used the average AR within the boundaries of the AR. However, there are often large areas of missing τ_d within the AR due to cloud cover. For this reason, we decided to test whether our results would change if we were to extend the boundaries of the averaging region used to calculate the dust score beyond the AR itself. We calculated the dust score and performed the Reynolds decomposition, but extended the boundaries of the AR in one degree latitude and longitude increments. The results were nearly identical to when the dust score is calculated with only dust within the AR boundaries. The maximum and minimum dust score remained identical and the mean decreased by 0.003. Each term in Equation 3.8 accounted for the same fraction of the variance of the dust score.

3.5 Conclusions and discussion

The AR dust score climatology presented here represents a new tool tool to investigate the characteristics and frequency of ARs in dusty environments. The mean dust score for the water-years 2002 to 2018 was found to be $0.026 \pm 0.004\sigma$ (Fig 3.13a). We have shown that there is a distinct seasonal cycle for ARs in dusty environments, with the highest dust score events occurring in March, due to the confluence of the AR season and the trans-Pacific dust season (Fig 3.11). This may be useful information when planning field campaigns investigating aerosol impacts on ARs. We have also shown that dust is present primarily in the warm sector of AR-associated extra-tropical cyclones but is also enhanced in the cold sector (Fig 3.10).

We have decomposed the contribution of the seasonal, and time varying components of τ_d and AR location in space and time to the total variance in dust score (Equation 3.8; Fig 3.13). We discovered that the correlated seasonal changes in τ_d and AR feature contribute 13% to the variance in dust score. While the contribution from independent changes in AR feature variability is small (5%), the contribution from independent changes in τ_d is much larger (40%). The contribution to the variance from correlated changes in τ_d with AR feature are also large (41%), which may indicate a dynamical relationship between dust and ARs. This motivates additional investigation into the meteorological conditions that lead to dusty ARs and the dynamics of these events. We will investigate this further in forthcoming work. The dust score presented here does not directly provide information about provenance. As a result, the question "To what extent do each of the major source regions (eg. Africa, East Asia, Middle East) contribute to dust in the vicinity of ARs?" remains unanswered but could be addressed through additional in-situ observations and/or modeling studies.

As discussed in the Methods section, there are several limitations to the AR dust score presented here. As a result of calculating a new dust score for each AR day, longer duration AR events may have greater influence on our climatological analysis of the seasonality and inter-annual variability of ARs in dusty environments. It is also possible that multiple AR objects could be present within the

domain on a given day and would be combined in the dust score for that day. Additionally, τ_d estimates are only available in clear sky pixels. Dust that is present within, above, or below clouds will not be counted in the dust score. Therefore, any dust that is activated as CCN or IN will not be counted in the dust score. It is plausible that an AR day could have substantial dust within, above, or below cloud and still have a low dust score.

3.6 Data Availability Statement

The AR dust score dataset described in this manuscript will be made publicly available at Pangea Open Access doi: XXXXXXXXX.

3.7 acknowledgments

This work was funded by the California Department of Water Resources contract 4600010378, Task Order $OSCOP215$ and the Army Corps of Engineers USACE (CESU) $W912HZ-15-0019$. We are grateful for the datasets and data archiving centers that supported this work and appreciate those who made our study possible, including the MERRA-2 team at the GMAO and staff at GSFC. We also thank the PRISM team and Oregon State University, and the MODIS team. We thank Dr. Zhenhai Zhang for his data contributions and guidance.

Chapter 3, in full, is a reprint of the material as it was submitted to Journal of Climate. K. K. Voss, A. T. Evan, K. A. Prather, F. M. Ralph, (In Review). Dusty Atmospheric Rivers: Characteristics and Origins, Journal of Climate. The dissertation author was the primary author of this paper.

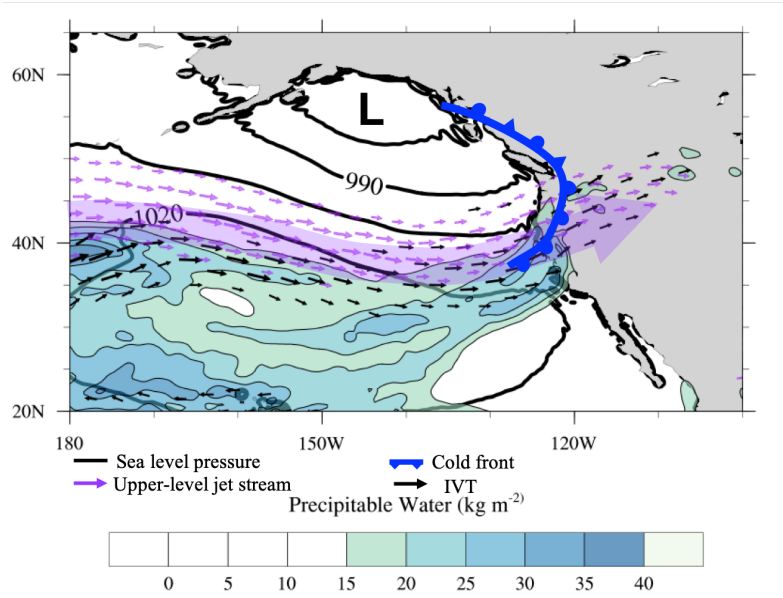

Figure 3.1: A conceptual synoptic view of conditions at 18:00 UTC 29 March 2010 based on information from the Climate Forecast System version 2 operational analysis (https://www.ncdc.noaa.gov/data-access/model-data/model-datasets/climate-forecast-system-version2-cfsv2, last access: 9 January 2020) and the Weather Prediction Center Surface Analysis Archive (https://www.wpc.ncep.noaa.gov/archives/, last access: 9 January 2020). Precipitable water is shown in blue filled contours and 250 hPa wind vectors are shown with purple arrows for wind speeds greater than 50m s^{-1}. IVT vectors are shown with black arrows for IVT greater than 250 kg m^{-2}. The upper-level jet is highlighted with a light purple curved arrow and sea level pressure contours (hPa) from CFSR are shown in black. The cold front location are drawn based WPC information.

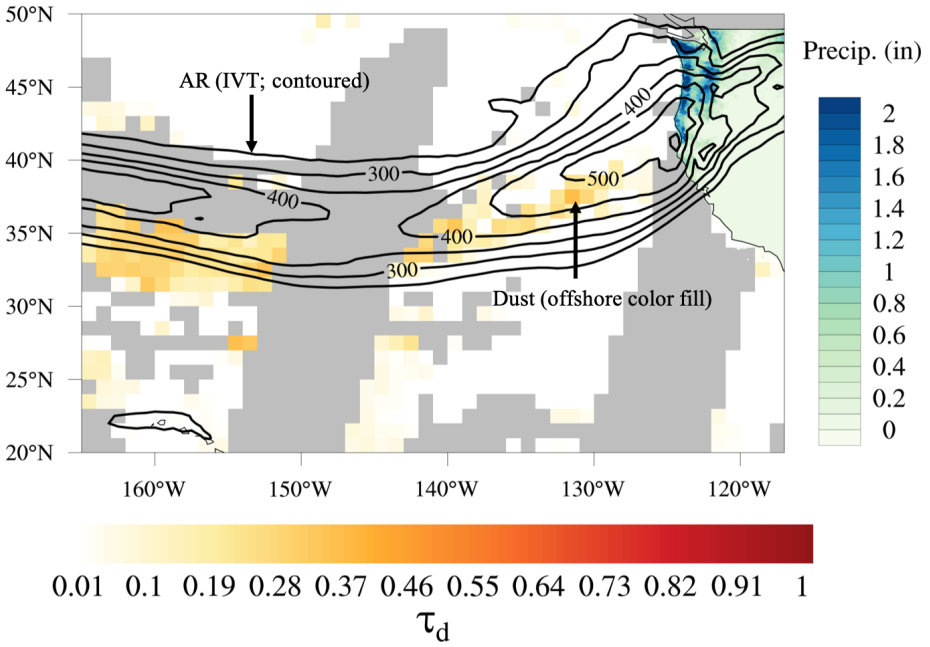

Figure 3.2: 18:00 UTC IVT (line contours), τ_d over land (filled orange contours), and PRISM daily precipitation (filled blue contours) when the AR made landfall on March 29, 2010. IVT contours are shown in 50 kg m^{-1} s^{-1} increments between 250 and 600 kg m^{-1} s^{-1}

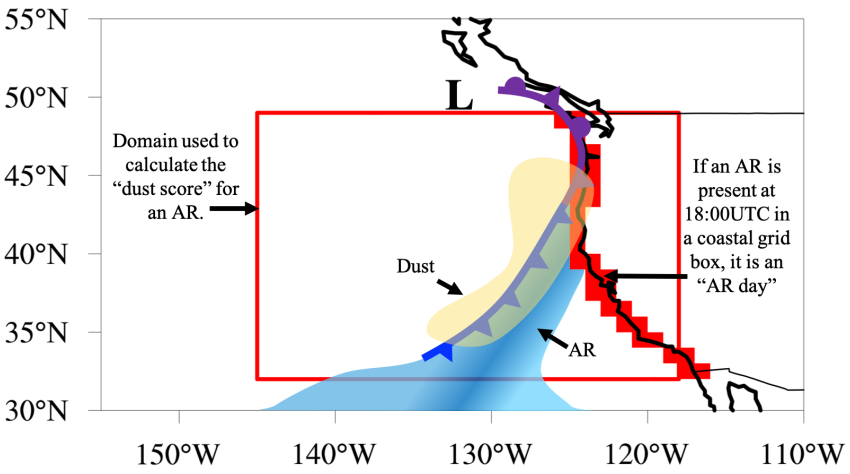

Figure 3.3: Schematic of an AR making landfall along the U.S. West Coast. In this example, the AR is located in the warm sector of an occluded extra-tropical cyclone along the cold front. The domain used in the calculation of dust score ($145 - 118°$W, $32 - 49°$N) is shown in the red box and 1-degree grid cells used to identify the U.S. West Coast for the purpose of defining AR days are filled in red.

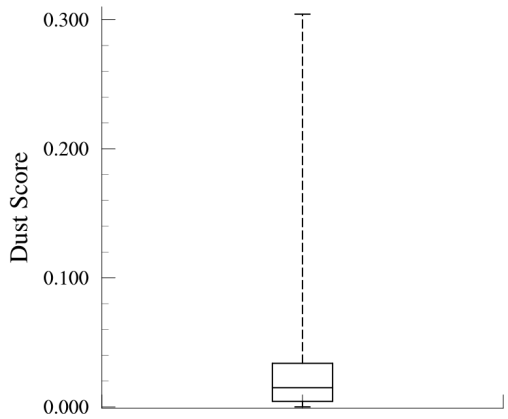

Figure 3.4: Box plot of dust scores for AR days between 2001 and 2018. The center line of the box represents the median (0.015), the top of the box represents the 75th percentile (0.034), and the bottom of the box represents the 25th percentile (0.004) dust scores. The top and bottom whiskers represent the maximum (0.30) and minimum (0), respectively.

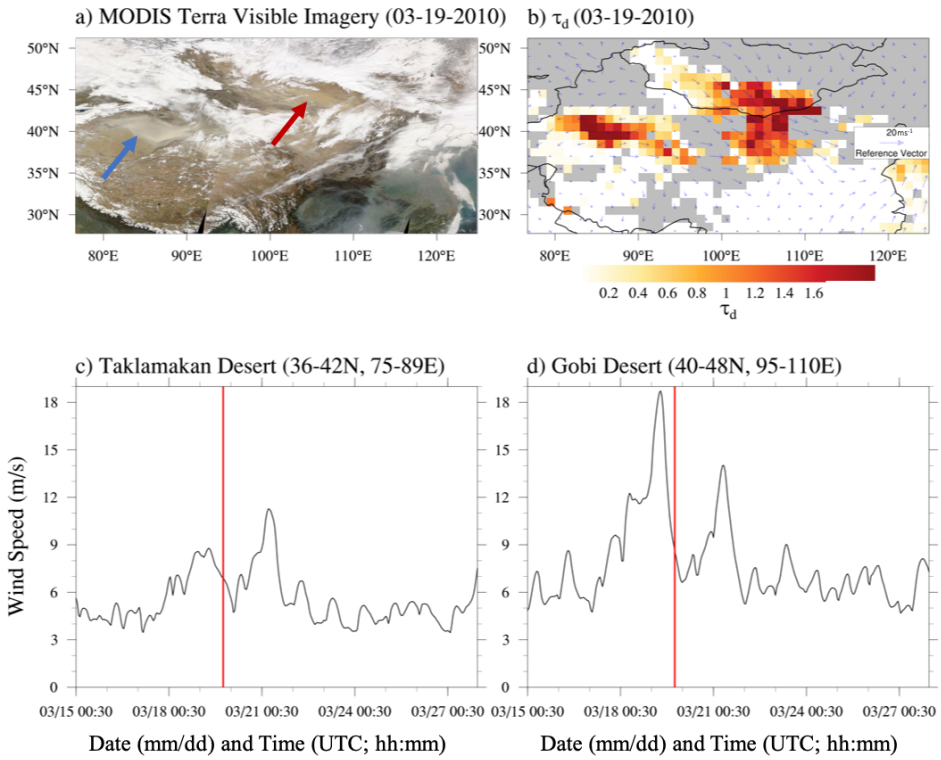

Figure 3.5: a) MODIS Terra Visible image of Asia on March 19, 2010 showing visible dust lofting over source regions in the Taklamakan desert (blue arrow) and Gobi desert (red arrow). b) τ_d derived from MODIS Terra on March 19th, 2019 showing enhanced dust over the Taklamakan desert and the Gobi desert overlaid with daily 10m wind vectors (ms^{-1}) from MERRA-2. Hourly MERRA-2 surface wind speed from March 15-21, 2010 averaged over c) the Taklamakan desert and d) the Gobi desert, showing enhanced winds on March 19 20:00 UTC. Grey areas in panel b indicate missing τ_d data. The overpass time of Terra MODIS is indicated on each wind speed time series with a red vertical line.

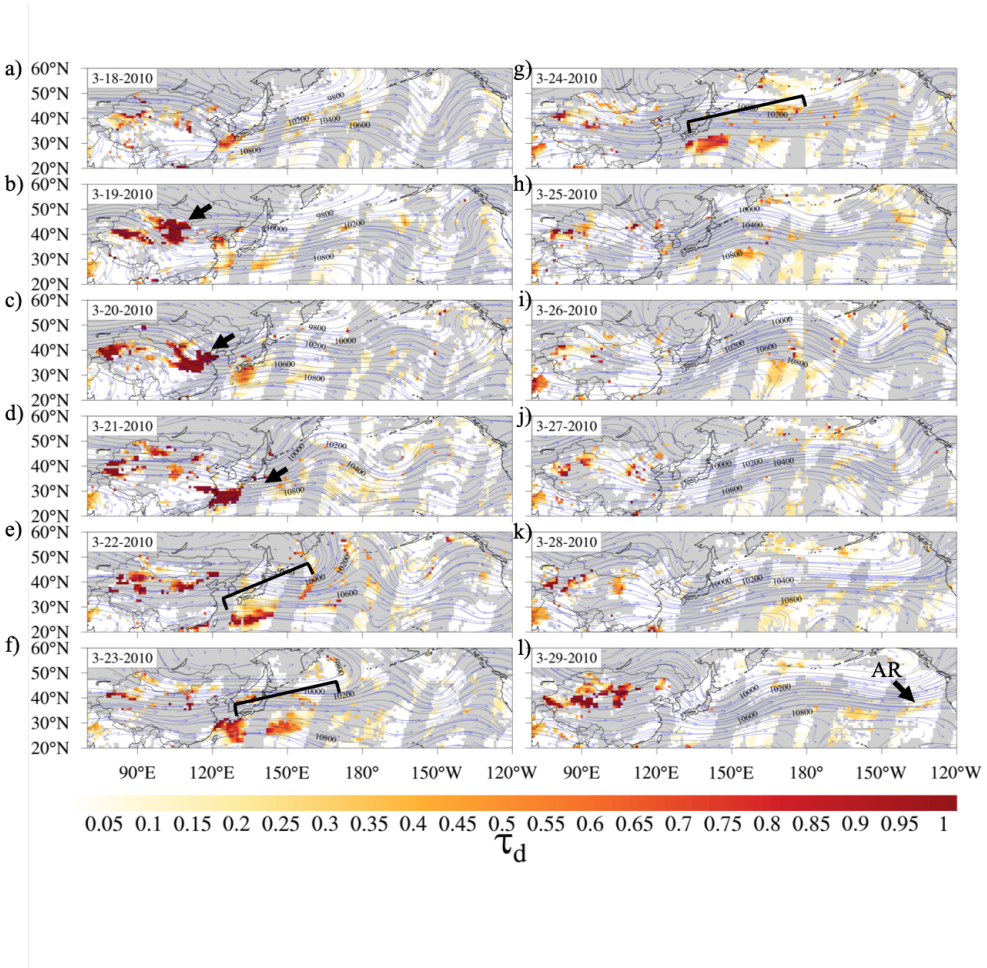

Figure 3.6: τ_d and MERRA-2 500hPa geopotential height and wind vectors for March 18, 2010 to March 29, 2010. Dust is initially lofted on March 19th and is transported across the Pacific, arriving coincident with an Atmospheric River on March 29, 2010. The black arrows follow the movement of the dust plume and black brackets indicate its extension. The AR is indicated in panel l.

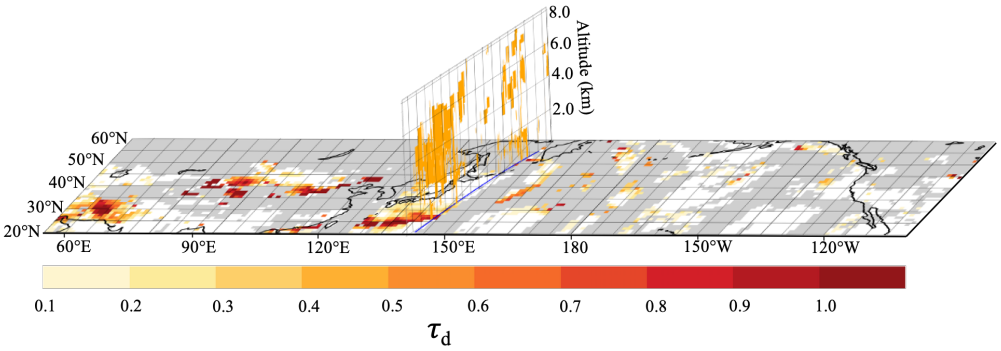

Figure 3.7: Transect from $30 - 50°$N near 150°E of CALIPSO Vertical Feature Mask (VFM) dust classification on March 22, 2010 16:11UTC overlaid upon τ_d centered upon the North Pacific Ocean on that date. The CALIOP orbital track is shown with.

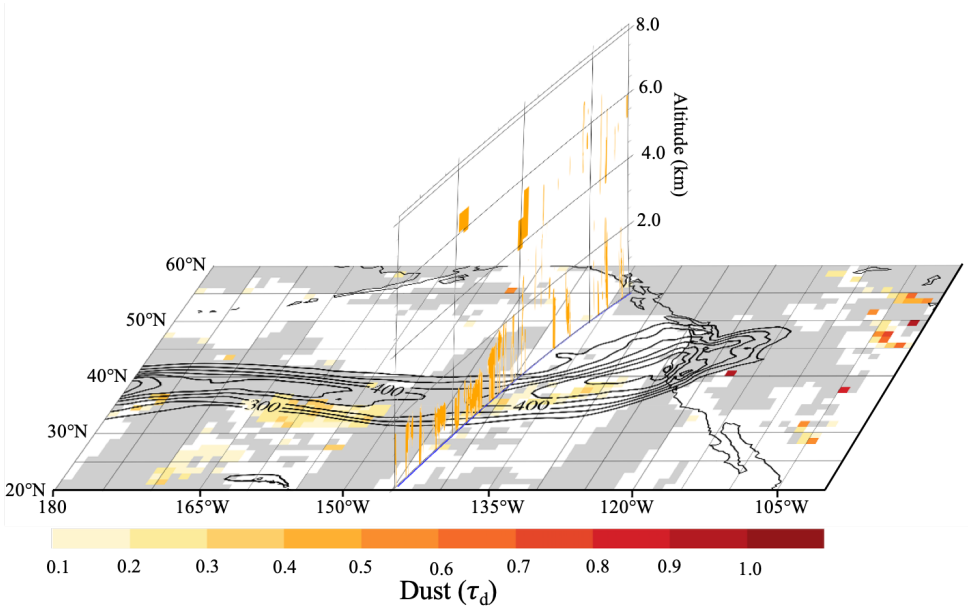

Figure 3.8: Transect from $30 - 50°$N near 145°W of CALIPSO Vertical Feature Mask (VFM) dust classification on March 29, 2010 11:22UTC overlaid upon τ_d centered upon the North Pacific Ocean on that date. The CALIOP orbital track is shown with a blue line.Contours of IVT greater than 250 kg m^{-s} s^{-1} are shown in black.

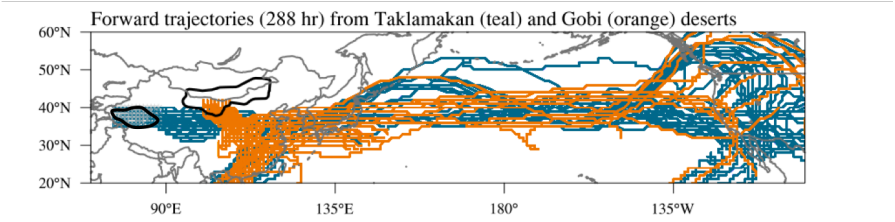

Figure 3.9: NOAA HYSPLIT 288 hour forward trajectory ensembles from the Taklamakan (teal) and Gobi (orange) deserts released at 18:00 UTC 19 March 2010 2km using 1 degree NCEP/NCAR meteorological information. The Gobi and Taklamakan deserts are outlined in black.

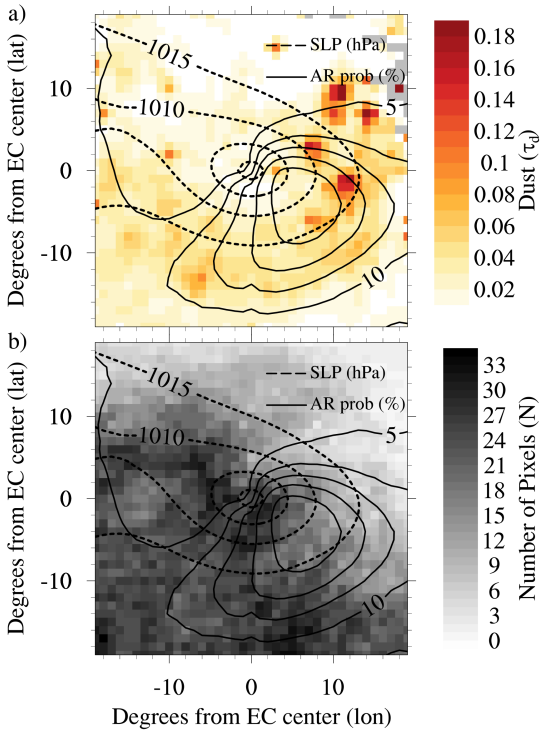

Figure 3.10: *a*) Extratropical cyclone-centric composite of τ_d using cool season (Nov-Mar) EC center locations from January 2001 to March 2010, for ECs that were found to be associated with an AR in Zhang et al. (2019) and which had mean τ_d within 15 degrees of EC center in the 90th percentile. *b*) The number of pixels (N), or non-missing values, for each grid cell used in the mean when calculating a). In both panel a and b, black solid line contours show AR probability (%), while dashed line contours show sea level pressure (hPa).

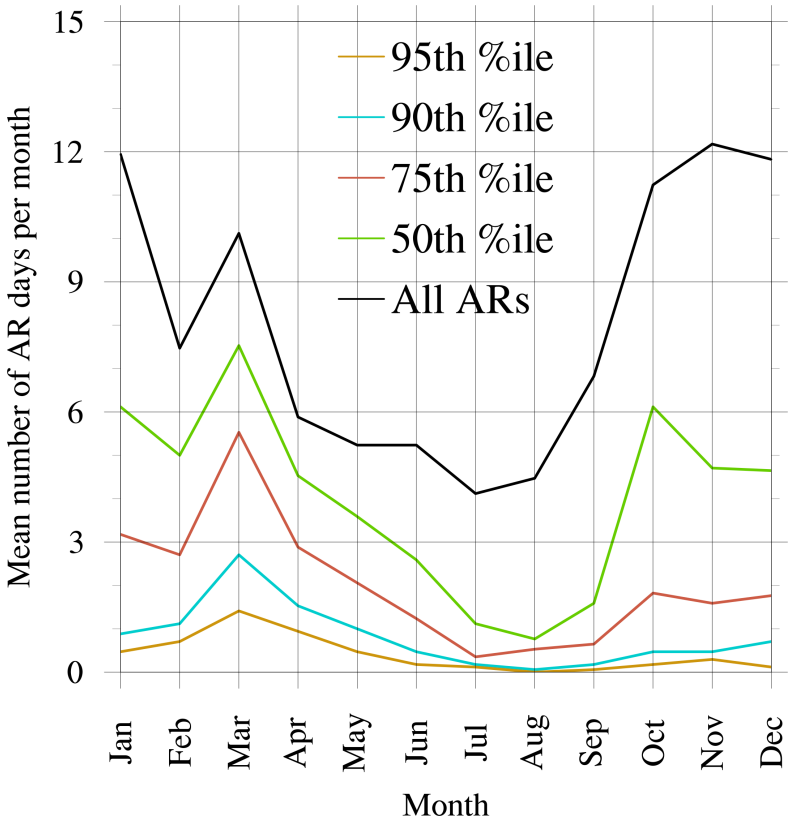

Figure 3.11: Average number of days each month with ARs making landfall along the contiguous U.S. west coast for the period from 2001-2018 grouped by dust-score percentile e.g. AR days with dust score greater than the 90th percentile dust score for the 2001-2018 period fall into the 90th percentile dust score group. ARs with dust scores greater than the 75th percentile dust score occur mostly during the Spring, when the dust season in Asia is at its peak.

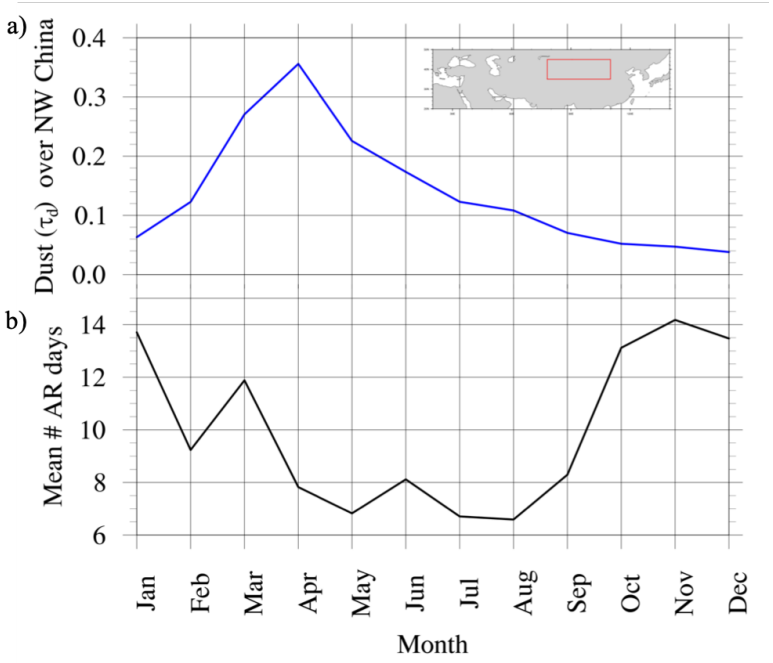

Figure 3.12: a) Climatological (2001-2017) monthly mean τ_d over northwestern China ($35-45°$N,$78-110°$E, red box in inset map). b) Mean number of days per month when an AR was landfalling along the U.S. west coast between 2001 and 2017.

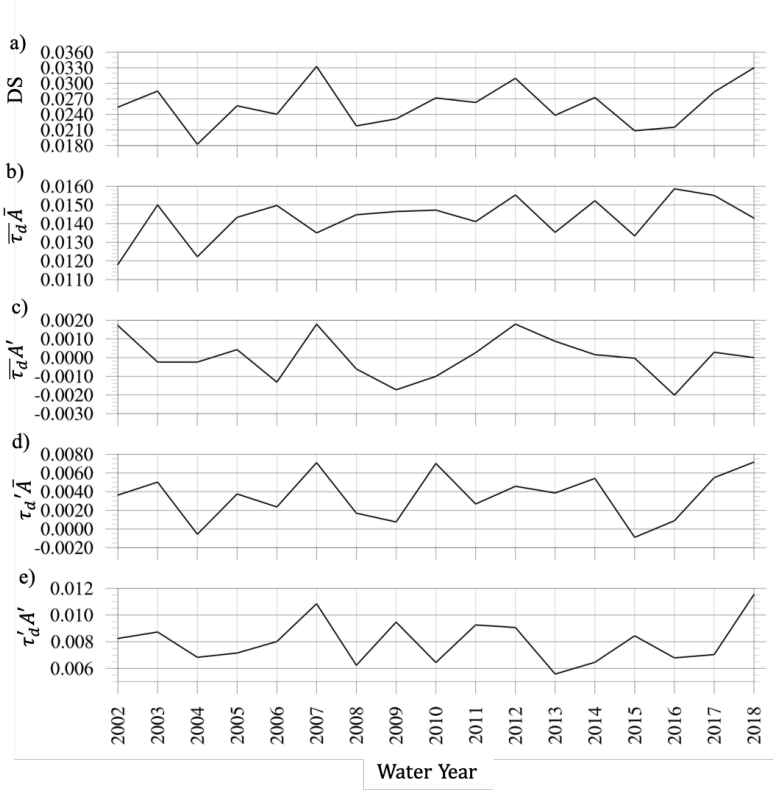

Figure 3.13: Time series (2001-2018) of water year mean terms in equation 3.8. Equation 3.8 describes the Reynolds decomposition dust score time series which was performed in order to understand the contribution of changes in dust and AR occurrence to the variability of the dust score.

Chapter 4

Evaluating the meteorological conditions associated with dusty atmospheric rivers

4.1 Chapter abstract

Trans-Pacific dust has been shown to influence the micro-physical characteristics of atmospheric rivers that make landfall along the U.S. west coast. Atmospheric Rivers (AR) reaching North America provide valuable water resources, but also can produce damaging floods. While substantial research has been devoted to understanding the structure and meteorological drivers of Atmospheric Rivers, far less is known about the conditions that lead to the presence of dust within and around these storms. Here, we utilize an 18-year record of AR dust scores combined with satellite, reanalysis, and observational meteorological data to understand the drivers of ARs embedded within dusty environments, or "dusty ARs", as compared to ARs in more pristine environments. We find that dusty ARs are associated with transport of dust from the east Asian coast to North America. Dusty ARs are associated with conditions that are especially conducive to transport of dust across the Pacific; namely, enhanced mid- to upper-tropospheric westerly winds over Asian dust source regions and over the Pacific. In contrast,

ARs in more pristine environments are associated with a persistent ridge over the central Pacific, which blocks zonal westerly flow, as well as continental dust.

4.2 Introduction

Mineral dust has been shown to influence the micro-physical characteristics of mixed phase clouds and is sometimes found within Atmospheric Rivers (ARs) that make landfall along the U.S. west coast, particularly in the late winter and early springtime (Ault et al., 2011; Creamean et al., 2013). ARs, narrow corridors of strong water vapor transport typically associated with an extra-tropical cyclone (Ralph et al., 2018), modulate the hydro-climate of the western U.S. by producing extreme precipitation (Neiman et al., 2008; Dettinger et al., 2011; Ralph et al., 2006; Lamjiri et al., 2017). Trans-Pacific dust, from regions such as Asia and Africa, has the potential to increase precipitation from ARs by enhancing ice formation in mixed-phase clouds (Creamean et al., 2013; Ault et al., 2011). While understanding of the structure and meteorological drivers of Atmospheric Rivers has evolved substantially in the recent two decades, there has been no long-term evaluation of the meteorological conditions that lead to the presence of dust in the environments surrounding ARs.

Our understanding of the impact of dust on AR precipitation and cloud micro-physics rests primarily on case studies of ARs during several years of CalWater Field campaigns, when chemical measurements of dust in clouds and precipitation were made (Ralph et al., 2016; Ault et al., 2011; Creamean et al., 2013, 2015, 2016; Fan et al., 2014). In order to understand the relationship between dust and ARs from a climatological perspective, a dust score has been developed for days of AR landfall along the U.S. west coast between 2001 and 2018 (Voss et al., In Review) using dust estimates from satellite observations (Voss and Evan, 2019) combined with the Rutz AR catalogue (Rutz et al., 2014). This dust score was calculated as the average of the dust aerosol optical depth (τ_d) within the lateral boundaries of the AR. It was calculated for every "AR day", defined as any day on which an AR was made landfall along the U.S. west coast from 2001 through 2018. It

was found that ARs with dust scores in the top 10th percentile occur primarily in March, at the confluence of the AR season (Oct-Mar) (Rutz et al., 2014) and the season favorable for trans-Pacific dust (Mar-May) (Voss et al., In Review). Correlated year-to-year variability in the frequency of ARs and the dust-content of the eastern North Pacific was found to explain more than a third of the variability of the dust score (Voss et al., In Review), suggesting that AR frequency and the dustiness of the eastern Pacific may be linked in some way, potentially through large-scale circulation. Here we explore this linkage.

We aim to understand how dusty AR events, defined here as the top 100 AR days in late winter and early spring (Feb.-Apr.) from 2001 through 2018, develop. We do this through investigation of the following question: What meteorological features are associated with dusty ARs *a*) over dust source regions and *b*) over the North Pacific, and how do these meteorological features differ from features associated with pristine ARs, defined here as the bottom 100 AR days in late winter and early spring (Feb.-Apr.) when ranked by dust score? We hypothesize that dusty ARs are characterized by conditions favorable to dust lofting over continental sources, including enhanced wind speeds over desert regions. We conjecture that dusty ARs will also be associated with conditions favorable for trans-Pacific transport, such as enhanced upper-level zonal winds extending across the North Pacific. We predict that ARs in more pristine environments will either have low surface wind speeds, and therefore less emission, over source regions and/or will have conditions that are unfavorable for trans-Pacific dust transport. This may include weak mid- and upper-level westerly winds, and ridging over the central Pacific.

We proceed by describing the datasets and methods used to investigate the conditions that control the dust content of the environment surrounding ARs that made landfall along the U.S. west coast between 2001 and 2018. We continue by comparing the probability distribution functions and composites of meteorological variables from dusty and pristine ARs. We show that the magnitude of the AR dust score is related to transport of dust across the Pacific. Our findings suggest that ARs, whether dusty or pristine, are generally associated with evidence of dust

emission from Asian deserts in the week prior. Dusty ARs are associated with enhanced upper- and mid level westerly winds over Asian dust sources and over the Pacific, while pristine ARs are associated with broad ridging over the central Pacific that may block or weaken westerly flow. We conclude with a discussion of how these findings may relate to other circulation features that exert influence over North American weather. Finally, we discuss the potential value of these findings for contextualizing future work on the relationship between dust and ARs.

4.3 Data and Methods

AR dust scores from Voss et al. (In Review) (Eq 4.2) are used throughout the analysis. The AR dust score is calculated from the average of dust aerosol optical depth (τ_d) within the boundaries of an AR feature as identified in the Rutz catalogue only for over-ocean grid cells that fell within a domain that contained the entire U.S. west coast and extended towards the central Pacific to a distance that reflects the approximate length scale (1800 km) of a wintertime North Pacific extra-tropical cyclone (Rudeva and Gulev, 2007) $145 - 116°$W, $32 - 49°$N. The probability of the presence of an AR at any 1° x 1° grid cell on a given day can be defined as P_{ar}, which in this case is always 0 or 1. This can be divided by the total number of grid cells that have a probability of 1 to yield the probability of an AR at a given grid cell normalized by the size of the AR, which we will define as P_{AR}.

$$P_{AR} = \frac{P_{ar}}{\sum_{n=1}^{N} P_{ar}} \tag{4.1}$$

Where n is a $1°x1°$ grid cell in the binary map of AR and N is the total number of non-missing value pixels on a given day. The dust score (S) is then defined as

$$S = \sum_{n=1}^{N} (\tau_d \cdot P_{AR}) \tag{4.2}$$

The dust score (S) is based upon daily dust aerosol optical depth (τ_d) from Voss and Evan (2019), hereafter VE19, for AR days between 2001 and 2018. The VE19 record of τ_d is an observational satellite-remote sensing estimate of column-integrated dust at $1°x1°$ spatial resolution. Only τ_d over ocean is used to calculate

S. Estimates of τ_d over ocean are based on isolation of the dust contribution to the Moderate Resolution Imaging Spectroradiometer (MODIS) Terra level 3 Dark Target Aerosol Optical Depth (AOD) at 550nm. In the calculation of τ_d, it is assumed that the total AOD is the sum of the contributions from dust, pollution, biomass burning, and marine aerosol (Kaufman, 2005). The contribution of marine aerosol to the total AOD is parameterized based on surface wind speed from reanalysis. The contribution from pollution and biomass burning aerosol is estimated based on the ratio of fine to coarse mode AOD. Estimates of τ_d are only available for clear-sky pixels and are also absent where sun glint occurs. The estimate of τ_d represents dust at approximately 1030 local time, as this is the approximate overpass time of the Terra satellite. Occasionally pixels of very high (> 0.5) τ_d were present within the AR feature, preferentially in the summer months (JJA). Inspection of MODIS Terra visible imagery on those dates at the location of the very high τ_d pixels yielded indications that this was a result of smoke, or thin cloud cover that was not screened out in the MODIS cloud clearing algorithm. In order to remove the impacts of these non-dust artifacts, we replaced any τ_d greater than or equal to 0.5 with a missing value prior to calculation of the dust score. For AR days between 2001 and 2018, the median dust score was 0.011, the 75th and 25th percentile dust scores were 0.022 and 0.005, respectively, and the maximum and minimum dust scores were 0.110 and 0, respectively.

Wind speeds and visibility at 3-hourly resolution from select surface stations (Table 4.1) located within desert dust source regions in Asia, the Middle East, and Northern Africa were used to investigate dust emission prior to AR days. Only stations that reported 3-hourly measurements between 2001 and 2018 were used in the analysis. Data were obtained from the National Ocean and Atmospheric Association (NOAA) National Centers for Environmental Information (NCEI) global surface station network (gis.ncdc.noaa.gov/maps/ncei/cdo/hourly).

The Modern-Era Retrospective analysis for Research and Applications, Version 2 (MERRA-2) 18:00 UTC surface wind vectors and daily mean sea level pressure (SLP), 500 and 250hPa zonal winds and geo-potential heights were used at 0.500° x 0.625° resolution. These variables were obtained from EarthData GES DISC

Table 4.1: Surface stations over desert source regions in Asia, the Middle East, and Africa used for 3-hourly wind speed and visibility measurements as indicators of dust emission.

Country	**Source Region**	**Stations (Lat, Lon)**
China	Taklamakan Desert	Tazhong (39.000°N, 83.667°E), Tikanlik (40.633°N, 87.700°E)
China	Gobi Desert	Guaizihu (41.367°N, 102.367°E), Bayan (40.750°N, 104.500°E)
Saudi Arabia	Arabian Desert	Turaif (31.693°N ,38.731°E), Hail (27.438°N, 41.686°E), Arar (30.907°N, 41.138°E), Yenbo (24.144°N, 38.063°E), Al Ahsa (25.285°N, 49.485°E), Al Baha (20.296°N, 41.634°E), Nejran (17.611°N, 44.419°E), Wadi Al Dawasir (20.504°N, 45.200°E), Sharurah (17.467°N, 47.121°E)
Chad	Sahara Desert	Faya Largeau (17.917°N, 19.110°E), Fada (17.167°N, 21.550°E)

(disc.gsfc.nasa.gov). A daily seasonal cycle, or climatology, of each of the aforementioned variables was constructed in order to calculate anomalies. The seasonal cycle was constructed from 30 years (1986-2018) of daily data using a 21-day running mean technique as described in (Hart and Grumm, 2001). A 30-year time period was chosen in order to obtain a smooth seasonal cycle. However, the results of our analysis are qualitatively the same when only the analysis time period (2001-2018) is used in calculation of anomalies. Daily mean MERRA-2 dust extinction optical depth for select days in the period from 2001 to 2018 was also used. A bootstrap with resampling approach was used for determining statistical significance of anomaly fields. A randomly sampled 1000 member distribution of representative data was compared with the composite signal and signals falling above the 90th percentile or below the 10th percentile at each MERRA-2 grid cell were deemed statistically significant.

4.4 Results and Discussion

4.4.1 Trans-Pacific Dust

Previous studies have found that long-range transported dust influences the micro-physical characteristics of ARs that make landfall along the U.S. West Coast (Ault et al., 2011; Creamean et al., 2013), and dust from the Taklamakan and Gobi Desert takes between 6 and 12 days to cross the Pacific (Yu et al., 2012). The March peak in the number of dusty ARs, at the confluence of the beginning of the trans-Pacific dust season and the end of the AR season suggests that trans-Pacific dust contributes more to the dustiness of the surroundings of an AR than local dust (Voss et al., In Review). Therefore, we hypothesize that dusty ARs will, on average, be associated not only with high τ_d within the domain used in calculating the dust score, but with evidence of transport across the Pacific ocean. In order to test this, dusty AR days, defined as the top 100 AR days in February, March, and April (FMA) when ranked by dust score, were compared with pristine AR days, defined as the bottom 100 AR days in FMA when ranked by dust score between 2001 and 2018. While the number of samples in each subset, (100) was chosen arbitrarily, other subset sizes (20, 30, 180) were tested and produced the same results qualitatively but with weaker signals, in dust and meteorological features, for 180 member subsets and noisier results for the small (20, 30) subsets.

We first compare composite Hovmoller diagrams of mean τ_d over eastern Asia and the Pacific Ocean, averaged over $30 - 50°$N, between 40°E and 240°E, for the 15 days leading up to the AR day (Fig 4.1,4.2). An AR day is defined as any day on which an AR was making landfall along the U.S. west coast from 2001 through 2018. For simplicity of language, AR days will be referred to as "ARs" hereafter. The area over eastern Asia, top panel in Figures 4.1 and 4.2, is shown with a separate color scale from the Pacific Ocean, bottom panel, for clarity due to the steep gradient in τ_d between desert source regions and relatively clean air over ocean. The approximate longitudinal boundaries of three major dust source regions, the Middle East, the Taklamakan desert, and the Gobi desert are shown in boxes marked with "M", "T", and "G", respectively.

Both dusty and pristine ARs show very high τ_d over the northern part of the Middle East ($50-60°$E) and over the Taklamakan ($70-90°$E for the 15 days leading up to the AR (Fig 4.1, 4.2). Over the Middle East, there is very little difference between τ_d prior to dusty and pristine ARs, as evidenced by less than 0.03 tau_d differences between dusty and pristine ARs (Fig 4.3). The mean τ_d over the Middle East was found to be 0.12 ± 0.043 for dusty ARs (Fig 4.1) and 0.11 ± 0.046 for pristine ARs (Fig 4.2). Over Asian deserts, τ_d was found to be slightly higher in the days leading up to dusty ARs compared to pristine ARs. Over the Taklamakan desert, the mean τ_d was found to be 0.18 ± 0.039 for dusty ARs and 0.17 ± 0.034 for pristine ARs. Over the Gobi desert, mean τ_d was found to be 0.10 ± 0.035 for dusty ARs and 0.09 ± 0.037 for pristine ARs.

The dusty AR composite is suggestive of transport of dust from these deserts eastward towards the coast, as evidenced by eastward extension of the 0.10 and 0.08 τ_d contours between 8 and 10 days prior to the AR day from 110° to 120°E (Fig 4.1). This is also visible as a greater than 0.03 positive offset in τ_d for dusty ARs relative to pristine ARs at the same time and location in figure 4.3. In general, the area between 110°E and 120°W which stretches from the central Gobi desert to the Asian coast shows 0.03 to 0.06 higher τ_d between 6 and 11 days prior to dusty ARs as compared to pristine ARs (Fig 4.3). There is an additional very high τ_d region near 120°E, the location of the east Asian coast, with peak values near 8 days prior to the AR and between 6 and 2 days prior to the AR day (Fig 4.1) indicating dust that has been transported offshore. The dusty and pristine AR composites differ more substantially over the Pacific. In the days leading up to the dusty AR days there is high (> 0.04) τ_d in the central Pacific within 12 days of the AR. Eight days prior to the AR, a region of greater than 0.045 τ_d extends between 140 and 145°E which is just offshore of northern Japan. A an area of high τ_d appears to propagate eastward across the Pacific at variable speed. On the day of the AR, there is a region of greater than 0.07 τ_d found east of 120°W associated with the AR. If a constant speed is assumed, the high (> 0.04) τ_d plume beginning 8 days prior to the AR and arriving along the U.S. west coast on the day of the AR indicates a transport speed of approximately 11.25 degrees longitude per day,

or approximately 956km per day at the latitude of 40°N. This transport speed is equivalent to approximately 11m s^{-1}.

Interestingly, three days prior to the AR day there is another eastward extension of the 0.10 τ_d contour from the Asian deserts ($70 - 95$°E) towards 110°E, and an eastward propagating high (> 0.04) τ_d signal over the western North Pacific (Fig 4.1). This is indicative of another wave of dust transport, potentially suggesting that these dust transport events occur successively.

For the pristine AR cases there is still high (0.07) τ_d over the Taklamakan ($70 - 90$°E) desert, Gobi desert ($100 - 110$°E) and even slightly offshore ($100 - 139$°E) (Fig 4.2). However, there is very little temporal variation in the zonal extent of contours over land. For example, the eastern boundary of the 0.04 τ_d contour over the Gobi desert remains near 110°E from 15 days prior to the pristine AR until 4 days prior to the AR in figure 4.2. In contrast, in the hovmoller diagram of dusty ARs the eastern boundary of the 0.04 τ_d contour over the Gobi varies in location between 110°E 15 days prior to the AR to 135°E 9 days prior to the AR and east to 113°E 4 days prior to the AR (Fig 4.1). There is much lower τ_d over the central and eastern Pacific in all days leading up to the AR (Fig 4.3). In contrast to the dusty AR composite, there are no days for which τ_d over the Gobi desert is above 0.12 for pristine ARs (Fig 4.2). Over the Pacific, there are isolated areas with > 0.04 τ_d, such as at 160°W twelve days prior to the AR or 180°E seven days prior to the AR, but they do not coherently propagate eastward and they do not persist longer than several days. There is also no region of very high (> 0.07) τ_d east of 120°W on the day of the AR.

Estimates of retrieved τ_d are only made for cloud-free and sun glint-free pixels. As a result, τ_d estimates from satellite retrievals are limited in very cloudy conditions such as those associated with extra-tropical cyclones and ARs. In contrast, MERRA-2 provides 1-hourly reanalysis dust extinction optical depths including under cloud cover. Dust extinction optical depths from MERRA-2 ($\tau_{d,M}$) are not completely independent from retrieved τ_d as MODIS AOD is assimilated into the reanalysis. Hovmoller composite diagrams of $\tau_{d,M}$ for the days preceding dusty and pristine AR days show qualitatively similar features to observed τ_d over ocean, but

differ slightly over land (Figs. 4.4, 4.5). The sea level pressure contours on these figures will be discussed later in section 4.4.3. Overall, $\tau_{d,M}$ is lower than τ_d and the color scale in Figures 4.4 and 4.5 has been adjusted accordingly. West of 60°E, the hovmoller diagram for dusty ARs shows $\tau_{d,M}$ mostly greater than 0.15 for all 15 days prior to the AR (Fig 4.4). For pristine ARs, $\tau_{d,M}$ east of 60° is mostly less than 0.15 between 15 and 4 days prior to the AR day (Fig 4.5). The more than 0.018 differences in $\tau_{d,M}$ over the Middle East between dusty and pristine ARs, as shown in figure 4.6, indicate that dusty ARs may be associated with dustier conditions over the Middle East. This was not evident in retrieved τ_d over the same region (Fig 4.1). The mean $\tau_{d,M}$ over the Middle East was found to be 0.13 ± 0.026 for dusty ARs and 0.11 ± 0.025 for pristine ARs.

Over the Taklamakan desert within 12 days of the AR, dusty ARs have more than 0.2 higher $\tau_{d,M}$ than pristine ARs (Fig 4.6). This difference between the dusty and pristine ARs is more pronounced than what was observed for τ_d in figure 4.3 over Asian deserts. At 105°E, near the Asian coast, dusty ARs do have higher $\tau_{d,M}$ (> 0.10) than pristine ARs consistent with what was observed for τ_d in Figure 4.1. Over the western Pacific, the composite of dusty ARs shows more dust than pristine ARs. Near day 8 in the dusty AR composite , there is a peak in the zonal extent of the 0.01 $\tau_{d,M}$ contour reaching 160°E. This peak is present in other contours on days closer to the AR, indicating an eastward migration of dust across the Pacific, consistent with what was described for retrieved τ_d. There is also a region of high (0.04) dust extinction east of 220°E where ARs make landfall along the U.S. west coast (Fig 4.4). The composite of $\tau_{d,M}$ for pristine ARs shows less dust overall in the Pacific, and this difference is most pronounced within a corridor that indicates an eastward migration in time, as evidenced by the greater than 0.005 offset in $\tau_{d,M}$ for dusty compared to pristine ARs that appears in a diagonal form in figure 4.6. Interestingly, there is a peak in the zonal extent of contours of $\tau_{d,M}$ near 150°E around seven days prior to the AR and indicates some eastward transport of dust in the days leading up to the AR (Fig 4.5). However, the magnitude is much smaller than for the dusty ARs and there is a minimum in dust extinction east of 220°E, the U.S. west coast.

The differences between τ_d over the Pacific for the days leading up to dusty and pristine AR reveal evidence of trans-Pacific transport of dust as a defining factor in the dustiness of the environment surrounding an AR. While τ_d, M from reanalysis indicate that dusty ARs are are associated with enhancement of dust over source regions such as the Middle East and the Taklamakan desert, retrieved τ_d did not yield strong evidence of this. It is unclear from these composites whether this transport is associated with an enhancement of dust emission over source regions, an enhancement of meteorological conditions favorable for transport, or both of these factors. In order to investigate this, we proceed by analysing the meteorological precursor conditions for dusty and pristine ARs over dust source regions and over the north Pacific.

4.4.2 Source Regions

Imported aerosol mass to North America is dominated by dust, primarily from Asia, followed by contributions from Africa and the Middle East (Yu et al., 2012). In order to understand whether dust emission over distant source regions in the days prior to an AR is a strong modulator of the dust content of the environment surrounding the AR, 3-hourly surface wind speed and visibility measurements from meteorological stations within Asian, Middle Eastern, and African dust source regions were compared for days leading up to dusty and pristine ARs. While these are not direct measurements of dust emission, dust emission is known to be primarily a function of surface wind speeds and in the absence of daily observed measurements of dust emission over these major dust source regions for the time period of interest (Benedetti et al., 2018), wind speed and visibility have been demonstrated as useful analogues in previous studies (Baddock et al., 2014; Kurosaki and Mikami, 2007).

Comparing measurements from stations within Asian dust source regions using all measurements in FMA regardless of whether there was an associated AR, mean wind speed and mean visibility are lower for the Taklamakan (mean wind speed: 2.12 ± 1.80m/s; mean visibility: $19,947 \pm 10,151$m) than for the Gobi (4.59 ± 3.23m/s; $26,215 \pm 6841$m) desert. The probability distribution function (PDF) of

Gobi desert wind speed for FMA (grey lines; Fig 4.7a) is wider than that of the Taklamakan (grey lines; Fig 4.7b) and has a longer tail extending towards high wind speeds. The PDF of visibility for the Gobi desert (grey lines; Fig 4.7e) shows that more than 60% of measurements are clear, with visibility greater than $25,000$ m. The PDF of visibility for the Taklamakan desert using all measurements from FMA (grey lines; Fig 4.7f) shows that a smaller fraction ($< 50\%$) of measurements are clear (visibility 2.5 km). The Taklamakan desert is known to have a lower threshold wind speed for dust emission than the Gobi desert (Kurosaki and Mikami, 2007).

Over the Gobi desert, the PDFs of visibility (Fig 4.7e) measurements prior to the AR are virtually identical for the 6 to 10 days prior to dusty (red line) and pristine (blue line) ARs. Differences between each of the subsets, ie. dusty AR, pristine AR, and all measurements, are within 3% for all visibility bins less than 27 km (Fig 4.7g). However, each visibility subset is statistically different from each other subset at 99% confidence, likely as a result of large ($> 6\%$) differences for the very high visibility (30 km) bins (Fig 4.7g). There is a greater than 5% higher probability of very clear (30 km visibility) measurements for the dusty AR subset compared to the pristine AR subset, and an almost 7% lower probability of very clear measurements for the pristine AR subset compared to the all measurement subset. This is contradictory to our hypothesis that there would be more dust, and therefore lower visibility, over the Gobi desert in the days prior to dusty ARs compared to pristine ARs. The PDFs of wind speeds for the days prior to dusty and pristine ARs are also nearly identical (Fig 4.7a), with differences of less than $\pm 2\%$ (Fig 4.7c). Interestingly, both prior-to-AR groups have higher mean winds speeds (dusty: 5.29 ± 3.34m/s; pristine: 5.13 ± 3.34m/s) than the when all measurements from FMA are used (4.59 ± 3.23m/s). This is clearly visualized as a shift in the PDF of wind speeds towards higher speeds for days prior to both dusty and pristine AR subsets as compared to all measurements (Fig 4.7a). For example, the probability of a measurement being in the 2 ms^{-1} bin is more than 3% lower for the dusty and pristine ARs than for all measurements, and the probability of a measurement being in the 6 ms^{-1} bin is 2% higher for dusty and pristine ARs compared to

all measurements (Fig 4.7c). Further, the difference in the mean between dusty ARs and all FMA measurements and pristine ARs and all FMA measurements is significant at 99% confidence but there is no difference between dusty and pristine ARs at the same confidence level. This supports our hypothesis that dusty ARs are associated with higher surface wind speeds over the Gobi desert, which lead to dust emission. However, it also would suggest that there are other determining factors for whether an AR is dusty since pristine ARs are also associated with these high wind speeds over the Gobi desert.

The average wind speed over the Taklamakan desert prior to dusty ARs is 2.15 ± 1.92m/s while prior to pristine ARs it is 2.09 ± 1.75m/s. The mean difference between the dusty and pristine AR subsets is not statistically significant at 99% confidence and the PDFs for the dusty AR, pristine AR, and all measurement subsets are similar to one another (Fig 4.7b). However, the difference of the dusty AR subset PDF and the pristine AR subset PDF indicates that there is a higher probability of wind speeds greater than 6 ms^{-1} for dusty ARs than for pristine ARs (Fig 4.7d). There is also a higher probability of wind speeds greater than 6 ms^{-1} for dusty ARs as compared to all measurements. Dust emission has been found to be dependent on exceeding of specific thresholds in wind speed (Kurosaki and Mikami, 2007), so differences between subsets in the high wind speed bins may be important even if the mean wind speed does not differ.

The PDFs of visibility for the Taklamakan show similar distributions for the days prior to dusty and pristine ARs (Fig 4.7f), with differences in probability within 1% excluding the 30 km visibility bin (Fig 4.7h). Both dusty and pristine ARs have higher probabilities for measurements with lower than 22.5 km visibility, with differences of up to +7%, and 28% lower probability for measurements in the highest visibility (30 km) bin. The average visibility over the Taklamakan prior to dusty AR days is 14.281 ± 8.408 km while prior to pristine AR days it is 15.156 ± 8.648 km, and this difference is statistically significant at 99% confidence. The average for the all measurement subset was found to be 19.948 km, which is statistically different from both the dusty AR and pristine AR subsets at 99% confidence. These results did not change qualitatively when the analysis window

was shifted 2 days earlier, ie. 4 to 9 days prior to the AR, or later, ie. 8 to 14 days prior to the AR, or when the length of the analysis window was shortened to 3 days. These results support our hypothesis that dusty ARs are associated with lower visibility over the Taklamakan desert, a possible indication of dust emission. However, consistent with what was found for the Gobi desert, pristine ARs were also found to be associated with lower visibility over the Taklamakan desert. While visibility was found to be lower over the Taklamakan desert prior to dusty ARs compared to pristine ARs, the difference was much smaller than the difference from the all measurement subset, again suggesting that other factors besides dust emission from source regions may play a role in modulating the dust content of the surroundings of an AR.

This same analysis was performed using stations above 25°N from Saudi Arabia previously used for dust transport studies (Notaro et al., 2013) and with stations from Africa near to source regions as identified in (Gherboudj et al., 2017). There was no difference in the PDF of visibility between days prior to dusty and pristine ARs for Saudi Arabia or for Chad, nor were there differences between the prior-to-AR groups and the climatology.

Composites of MERRA-2 2-meter wind speed between 5 and 11 days prior to AR landfall for dusty (Fig 4.8a) and pristine (Fig 4.8b) AR days both show small (< 3 m s^{-1}) positive anomalies in wind speed 9-days prior to AR landfall over the Gobi (near 40°N, 103°E) and Taklamakan desert (near 40°N, 85°E) as well as over the northern part of the Arabian Peninsula (near 30°N, 17°E) and northern Africa (above 22°N) but there is no clear difference between the days prior to dusty and pristine AR days (Fig 4.8c). The spatial structure of 2-meter wind speed does not change between 12 and 5 days of AR landfall, so only the composite for 9 days prior to AR landfall is shown in Figure 4.8.

Overall, these results show mixed consistency with our hypothesis. We predicted that dusty ARs would be associated with high wind speeds and low visibility, indirect indicators of dust emission over source regions, and that pristine ARs would not be associated with these indicators. While it was found that the mean wind speed over the Gobi desert was higher that normal for dusty ARs, with a

significant difference at 99% confidence, the pristine ARs were also found to be associated with a higher mean wind speed than normal. Inconsistent with our hypothesis, dusty ARs were found to be associated with a higher mean visibility over the Gobi desert than pristine ARs. Over the Taklamakan desert, there was no statistically significant difference in mean wind speed for dusty ARs or pristine ARs from all measurement or from each other. However, dusty ARs were associated with a higher probability of high (> 6 ms^{-1}) wind speeds, which may be important for dust emission. Consistent with our hypothesis, dusty ARs were found to be associated with a statistically significantly lower mean visibility than normal. However, the same is true for pristine ARs. The difference between dusty and pristine ARs, in visibility over the Taklamakan, were much smaller than the difference from the all measurement subset. This could indicate that dust emission in these regions in springtime is in some way linked to AR activity through large scale circulation. This is also supported by the similarity of τ_d over source regions in the days leading up to dusty and pristine ARs as shown in Figures 4.1 and 4.2

4.4.3 Pacific Region

It is plausible that the meteorological conditions of the Pacific may yield considerable influence over whether dust is transported across the Pacific to reach the surroundings of an AR. In order to test whether this is the case, synoptic meteorological conditions over the Pacific for dusty ARs were compared to that for pristine ARs to test the hypothesis that dusty ARs are associated with conditions that would be favorable for transport of dust from the Asian continent towards North America. These conditions could include enhanced upper-level zonal winds across the Pacific and/or eastward propagating extra-tropical cyclones that may facilitate transport dust across the Pacific.

In order to investigate the upper-level dynamics associated with dusty ARs as compared with pristine ARs, composites of 250-hPa anomalous, relative to the seasonal cycle, zonal winds (shaded contours) and anomalous 250-hPa geopotential height (line contours) were constructed using the days prior and dusty (Fig 4.9) and pristine (Fig 4.10) ARs. Geopotential heights at this pressure level

are commonly used to investigate upper-tropospheric features such as the North Pacific Jet (Griffin and Martin, 2017; Jaffe et al., 2011; Eichelberger and Hartmann, 2007), but the features (e.g. troughs, ridges) we describe here are also present at 500hPa. In the composite of six days prior to the dusty ARs (Fig 4.9a), two weak (-5m anomaly) upper-level troughs are present, one over Mongolia, centered near 100°E, and one over northern Japan (135°E). These troughs are associated with 2 ms^{-1} enhancements in upper-level eastward winds over northern Asia, at the eastern edge of the Taklamakan desert (approx. 90°E) and over the entire Gobi desert (approx. $90 - 116$°E), extending over Japan towards the Pacific. Between 5 and 4 days prior to the AR (Fig 4.9b,c), the trough over Mongolia recedes and the trough over Japan deepens to a -15 m anomaly. Simultaneously, a +30 m ridge develops in the north eastern Pacific centered around 35°N, 225°E with a -50 m trough over western British Columbia (55°N, 240°E) just northeast of it. Three days prior to the AR (Fig 4.9d), the trough over Japan extends eastward and begins to shed a smaller low geo-potential height anomaly into the central Pacific and 3-5 ms^{-1} anomalous westerly winds develop between 30 and 40°N in the central Pacific, indicating an extension of the North Pacific Jet. Two days prior to the AR (Fig 4.9e), the parent stationary low over Japan continues to deepened beyond -25 m while shedding a smaller low into the central Pacific. The troughs that were present in the Central Pacific and over British Columbia merge on the day before the AR (Fig 4.9f), forming a low -50 m geo-potential height anomaly in the Gulf of Alaska (approx. 55°N, 215°E). The trough over Japan widens on the day before the AR. On day zero (Fig 4.9g), the day the AR makes landfall on the western U.S. coast, there is an elongated trough over the eastern Pacific and western North America and a trough over Japan that has maintained position, yet weakened slightly from the day before. These two upper-level troughs are associated with enhanced +3 to +7 ms^{-1} westerly upper-level zonal winds extending across the Pacific from 135°E to 245°e, near 30°N in the western Pacific. There are also greater than 6 ms^{-1} enhancements in zonal winds between 30 and 50°N in the eastern Pacific, between the strong trough and the ridge. The enhanced westerly winds over the eastern Taklamakan and entire Gobi desert 6 days prior to the AR

day are likely to facilitate transport of dust from these source regions towards the Asian Pacific coast. Consistent with this, there is a greater than 0.10 positive offset in τ_d between southern central Mongolia (near 45°N, 110°E) and the Asian coast (near 45°N, 125°E) for dusty ARs as compared to pristine ARs six days prior to the AR (Fig 4.11a). There are also greater than +0.05 offsets in τ_d for dusty ARs at the southern flank of the stationary low 500-hPa (Fig 4.11b) and 250-hPa (Fig 4.9b) geo-potential height anomalies over Japan, co-located with the enhanced westerly zonal winds in the upper-troposphere. Within four days of the AR, positive offsets in τ_d over the Pacific are mostly co-located with low 500-hPa geo-potential height anomalies (Fig 4.11d-g). For example, two days prior to the AR (Fig 4.11e), there are > 0.04 offsets in τ_d for dusty ARs, as compared to pristine ARs, positioned on the southern flank of a -25 m 500-hPa geo-potential height anomaly centered at 41°N, 185°E. The largest positive offsets (> 0.08) in τ_d over the Pacific occur on the day of the AR offshore of the western U.S. and east of 210°E, situated between a ridge (40°N, 235°E) and trough (55°N, 220°E) (Fig 4.11g).

A very different pattern emerges in composites of upper-level (250-hPa) zonal winds (shaded contours) and geo-potential heights (line contours) for pristine ARs (Fig 4.10). There is substantial ridging over the Asian continent with +15 and +100 m 250-hPa geo-potential height centers near 50°N, 95°E and 50°N, 130°E, respectively, six days prior to the AR (Fig 4.10a) and broader ridging over the continent within five days of the AR (Fig 4.10b). The southern flank of these high geo-potential height anomalies are collocated with weak anomalous -5 ms^{-1} upper-level flow over Asian dust source regions between three and five days prior to AR landfall (Fig 4.10b-d). For these pristine ARs, a ridge centered at 180°E persists in the central Pacific between 6 days and 1 day prior the AR, blocking or weakening flow from the Asian continent towards North America (Fig 4.10a-f). However, the difference in τ_d between dusty and pristine ARs three to five days prior to the AR indicates that dust may still be present in the western and central Pacific but displaced to the North, as evidenced by -0.04 offsets in τ_d within $45-50$°N, $140-190$°E between dusty and pristine ARs (Fig 4.11b-d). The deeper than 100 m low in the gulf of Alaska (near 50°N,135°W) is fed by the central Pacific

high (Fig 4.10g).

The pattern of upper-level geo-potential height for dusty ARs bears resemblance to the extended mode of the North Pacific Jet. The North Pacific jet stream is a narrow corridor of strong upper-level (200-250-hPa) wind speeds that is consistently located downstream of the Asian continent but meanders because of factors such as interactions with baroclinic eddies along the storm track, the East Asian winter monsoon, and tropical convection (Winters et al., 2019), and is a region of high horizontal and vertical sheer. Empirical Orthogonal Function analysis has been used to identify several leading modes of variability of the North Pacific jet stream (Eichelberger and Hartmann, 2007; Winters et al., 2019; Athanasiadis et al., 2010; Jaffe et al., 2011). These leading modes include a zonal extension or retraction and a north or southward meridional shift. Griffin and Martin (2017) found that the mode of the North Pacific jet stream yields considerable influence on the large-scale flow pattern across the North Pacific and over North America.

The extended jet pattern was found to develop from two upper-level low (250-hPa) geo-potential height anomalies, one in the central North Pacific at the exit region of the climatological jet, near 200°E, 40°N, and another just north of the climatological jet, near southern Japan (Fig. 4.9b). These upper-level height anomalies each produce enhancements in zonal eastward wind at their southern flanks. As the height anomaly in the central Pacific intensifies, it merges with the low anomaly near East Asia. So, too, do the anomalies in zonal wind resulting in an effective extension of the jet farther to the east towards North America. These features in the upper-level geo-potential height and zonal wind fields are the similar to the features that are present in composites of upper-level height and winds in the days prior to dusty ARs (Fig. 4.9), suggesting that an extended north Pacific jet may allow dust to be transported from Asian dust source regions into the central and eastern North Pacific where it can be picked up by an extra-tropical cyclone and reach the vicinity of an AR.

Hovmoller diagrams of mean $30-40$°N anomalous sea level pressure (SLP) between the Asian coast (100°E) and North America (210°E) for dusty ARs between 15 days prior to the AR and the day of the AR show a region of anomalously low

SLP that develops over western China (100°E) beginning around 15 days prior to the AR, deepening to a minimum of less than -150 hPa around 11 days prior and weakening to zero by approximately eight days prior to the AR (Fig 4.4). At the same time, a greater than +250 hPa ridge develops in the eastern North Pacific until around six days prior to the AR. Between nine days prior to the AR and the day of the AR, the low SLP from the western China coast weakens and a new region of less than -150 hPa low SLP anomaly developed in the central Pacific (near 160°E) between 8 and 3 days prior to the AR, appearing to migrate towards the western U.S. coast (near 210°E). Between 5 days prior and the day of the AR, this trough deepens to less than -300 hPa in the Northeastern Pacific.

From a hovmoller diagram of mean SLP for the days prior to pristine ARs (Fig 4.5), the primary feature is a region of high, greater than 300 hPa, SLP between 160°E and 220°E that has developed by 15 days prior to the AR and weakens slightly, by at least 50 hPa, around 4 days prior to the AR day but persists as a region of anomalously high SLP up to the AR day. A region of anomalously low (approx. -100 hPa) SLP is also present over western China (near 100°E) between 9 and 14 days prior to the AR for the pristine days but it is weaker than for the dusty days. The anomalous low SLP, approximately -100 hPa, feature in the western Pacific (near 120°E) is mostly confined within the 2 days leading up to the AR and the day of the AR and is confined east of 140°W. The trough and ridge patterns described using composites of upper-level (250-hPa) winds and heights (Fig 4.9, 4.10) are consistent with what is found at mid-levels of the troposphere (500-hPa; not shown).

The latitude of landfall of ARs is controlled by dipoles in pressure along the coastline that may direct moisture through the dominant flow towards specific location. The northeastward slanting ridge centered just offshore of northern California and the trough centered in the gulf of Alaska in the composite of upper-level geo-potential height (Fig 4.9), which also exists at 500 and 850-hPa (not shown) may steer ARs towards the Pacific Northwest and southern British Columbia. It is therefore plausible that ARs impacting the northern parts of the U.S. coastline are more likely to contain dust than those impacting places such as southern

California.

Some of the characteristic synoptic conditions associated with dusty ARs, including an enhanced 250-hPa North Pacific Jet (Fig 4.9) and low 500-hPa geopotential heights (Fig 4.11) across the North Pacific, are the same conditions that have been found to be associated with AR families, successive but distinct AR events within a short time period (Fish et al., 2019). It is possible that these dusty ARs occur in succession, associated with AR families. The suggestion that dusty ARs may occur successively is consistent with a case study of a dusty AR (Voss et al., In Review). While the case study in Voss et al. (In Review) focused on an AR event that followed a major Asian dust storm on March 19th, 2010, another very high τ_d event over the Gobi desert and the beginning of a dust transport event was visible 7 to 9 days later, at the same time that the AR event that the case study focused on was making landfall along the U.S. west coast.

4.4.4 Conceptual Model

The conceptual model presented in Figure 4.12 summarizes the steps in the development of dusty ARs, suggested by our findings. In step I, high wind speeds over Asia loft dust from source regions such as the Taklamakan and Gobi deserts. This step is not unique to dusty ARs, but our finding suggest that it often occurs for both high and pristine ARs. In step II, mid- to upper-level westerly winds over the Asian continent transport dust from source regions towards the Asian coast. In step III, an extended North Pacific Jet over Japan transports dust from the Asian coast towards the central Pacific. In step IV, a transient extra-tropical cyclone, potentially one that developed from a parent low associated with the extended jet, moves eastward towards North America carrying with it dust from the western or central Pacific. In step V, an AR develops associated with a deepening low in the Gulf of Alaska that now contains dust from the transient extra-tropical cyclone.

4.5 Conclusion

An 18-year record of dust score for Atmospheric Rivers (ARs) that made landfall along the U.S. west coast was used to investigate the conditions that enhance the dust content of the environment surrounding the AR. It was found that dusty ARs are associated with long-range transport of dust across the Pacific Ocean. Our findings suggest that dust emission over source regions in Asia appears to be favored in the week prior to AR landfall for both dusty and pristine ARs. In addition, the synoptic conditions associated with dusty ARs, as opposed to pristine ARs, indicate that the large- and synoptic-scale meteorology over the North Pacific is an important modulator of the dustiness of AR surroundings. These conditions include enhanced upper and mid-level westerly winds over northern China, where there are dust sources, an extended jet over Japan, and eastward propagating extra-tropical cyclones moving from the western and central Pacific towards North America.

While this work does not address the impacts of dust on ARs, it may serve to contextualize further research on this subject. For example, the statistical relationship between dust score and cloud micro-physical parameters or precipitation may be as much a result of the synoptic and large-scale meteorological conditions that lead to the presence of dust in ARs as a result of dust enhancing precipitation or dust changing cloud micro-physics. A long-term analysis of the impacts of dust on precipitation or micro-physical characteristics would be informative for understanding the impact of dust on ARs, but would need to be cautious of the underlying dynamics that lead to these events.

While research on the impact of dust on ARs has focused on the micro-physical impacts of dust, when acting as an ice nucleating particle, it is also possible that dust may have direct impacts on the temperature structure of the environment surrounding ARs. The direct radiative effect of trans-Pacific dust in springtime has been estimated at approximately -3 W $m^{-}2$, which is approximately 37% of the impact from North American domestic-sourced aerosols (Yu et al., 2012). Whether dust has direct impacts on the temperature structure of ARs, or their associated extra-tropical cyclones, remains an open question worth addressing.

Finally, this understanding may also yield some amount of predictability that may be useful for timing field measurements. In-situ measurements are extremely valuable for constraining the impact of dust on ARs, and the ability to predict when an AR is likely to contain dust may allow for more efficient use of resources.

4.6 Acknowledgments

This work was funded by the California Department of Water Resources contract 4600010378, Task Order $OSCOP215$ and the Army Corps of Engineers USACE (CESU) $W912HZ-15-0019$. We are grateful for the datasets and data archiving centers that supported this work and appreciate those who made our study possible, including the MERRA-2 team at the GMAO. We thank Meredith Fish for her contributions of a 30-year running mean climatology of MERRA-2 variables.

Chapter 4, in part is currently being prepared for submission for publication of the material. K. K. Voss; A. T. Evan; F. M. Ralph. The dissertation author was the primary investigator and author of this material.

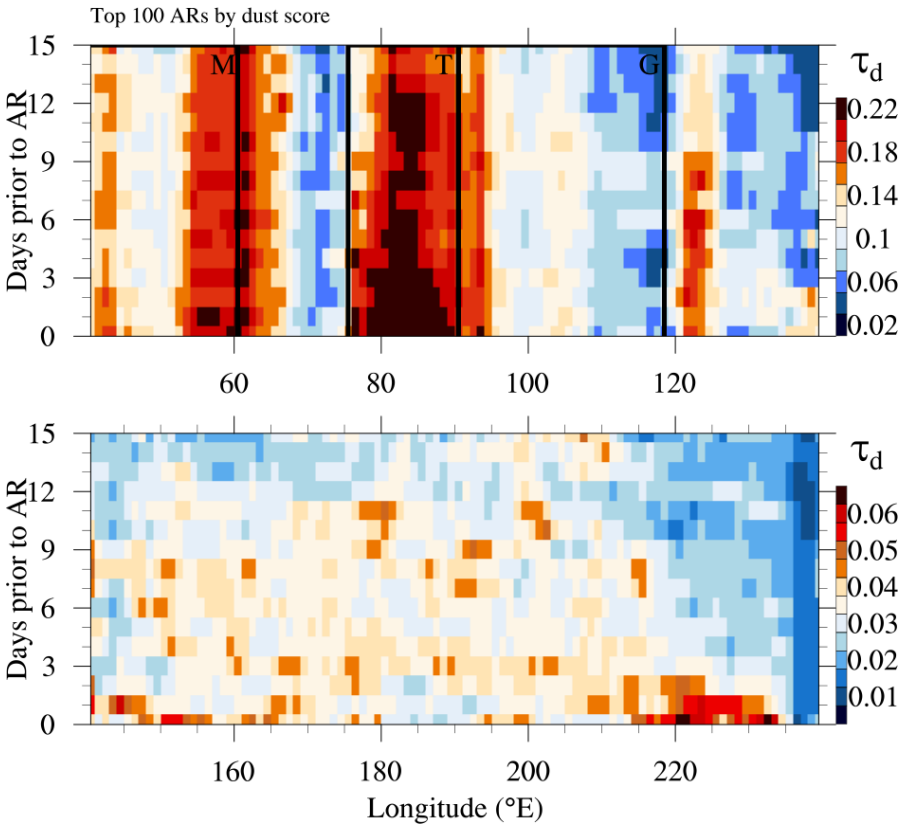

Figure 4.1: Composite Hovmoller diagram of mean $30-50$°N dust aerosol optical depth (τ_d) over the Asian continent ($40-140$°E; top) and over the North Pacific Ocean ($140-240$°E; bottom) for the 15 days leading up to and the day of dusty ARs. A 5-point local smoothing filter was applied to the τ_d field prior to calculation of the $30-50$°N mean.

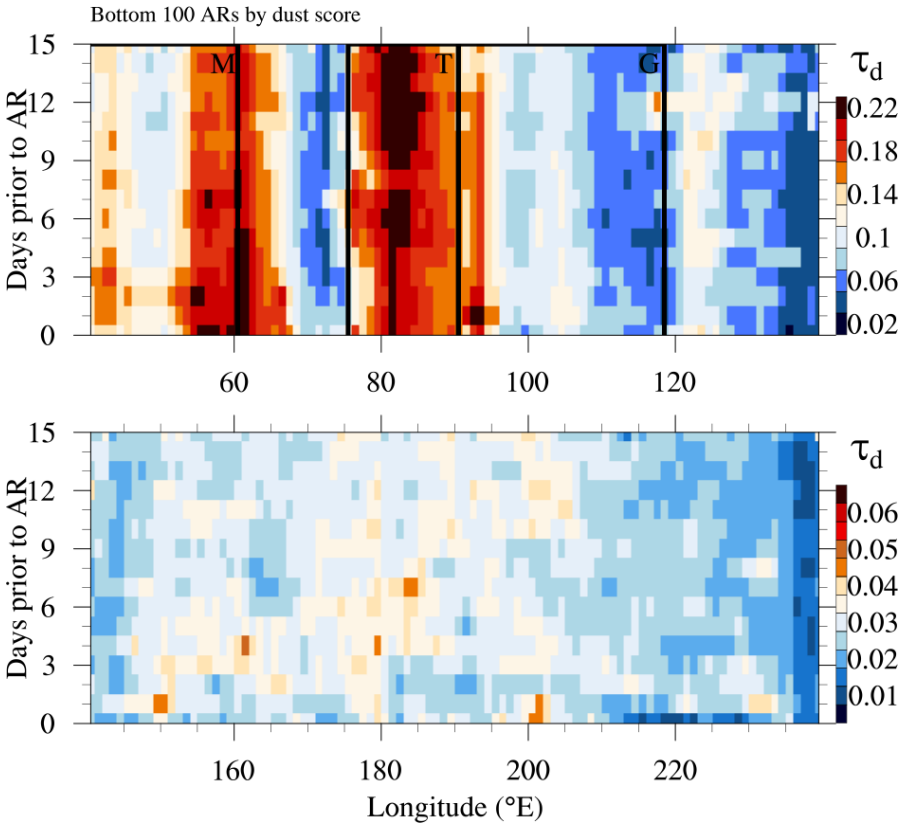

Figure 4.2: Same as Figure 4.1 but for pristine ARs.

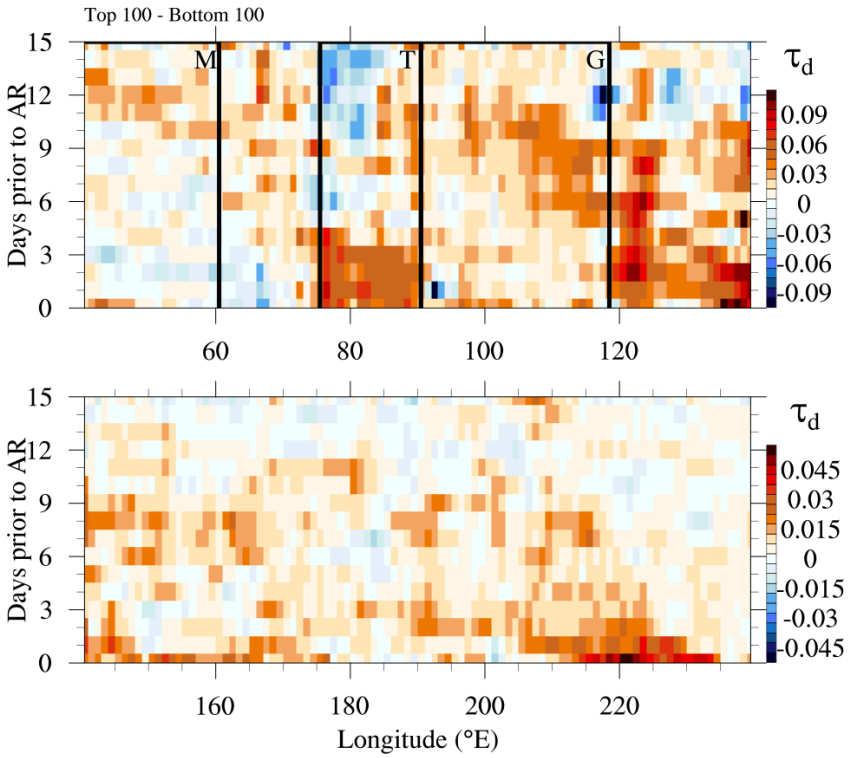

Figure 4.3: Difference of Figure 4.1 and 4.2.

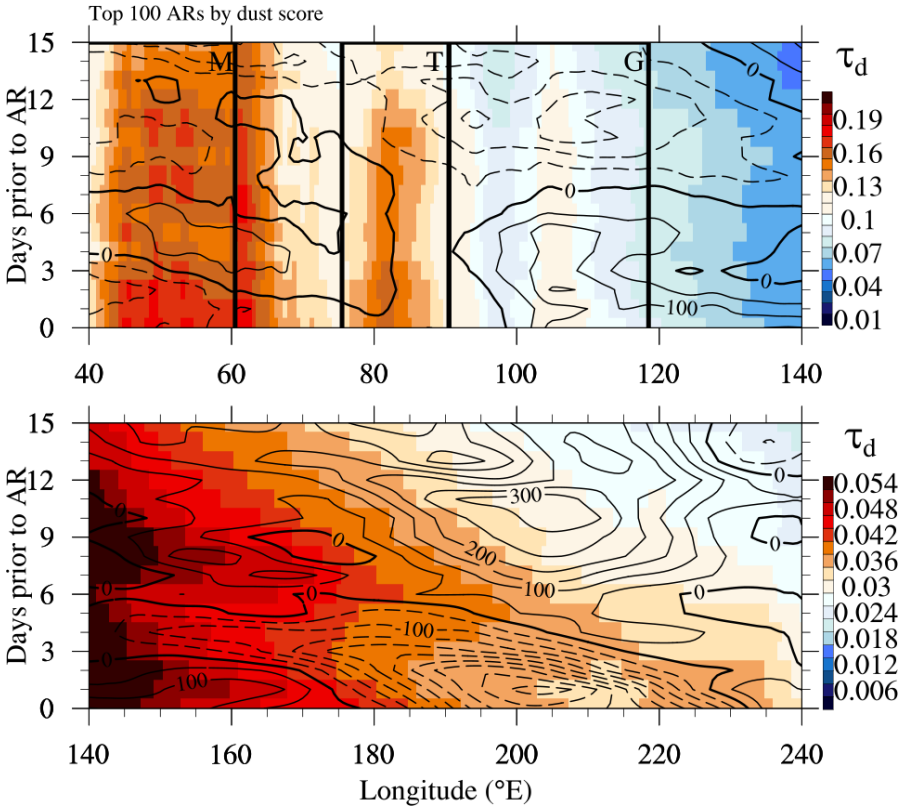

Figure 4.4: Composite Hovmoller diagram of MERRA-2 mean $30-50°$N dust extinction optical depth ($\tau_{d,M}$; shaded) and sea level pressure anomalies (SLP; hPa; lines) over the Asian continent ($40-140°$E; top) and over the North Pacific Ocean ($140-240°$E; bottom) for the 15 days leading up to and the day of dusty ARs. Positive SLP anomalies are shown with solid lines while negative anomalies are shown with dashed lines.

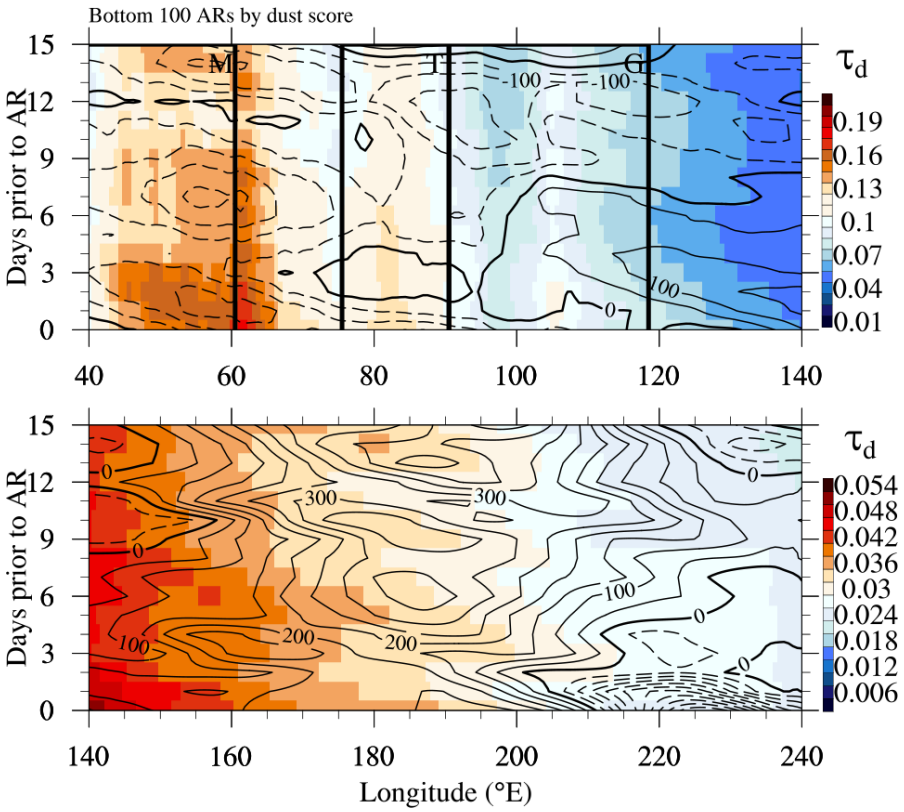

Figure 4.5: Same as Figure 4.4 but for pristine ARs

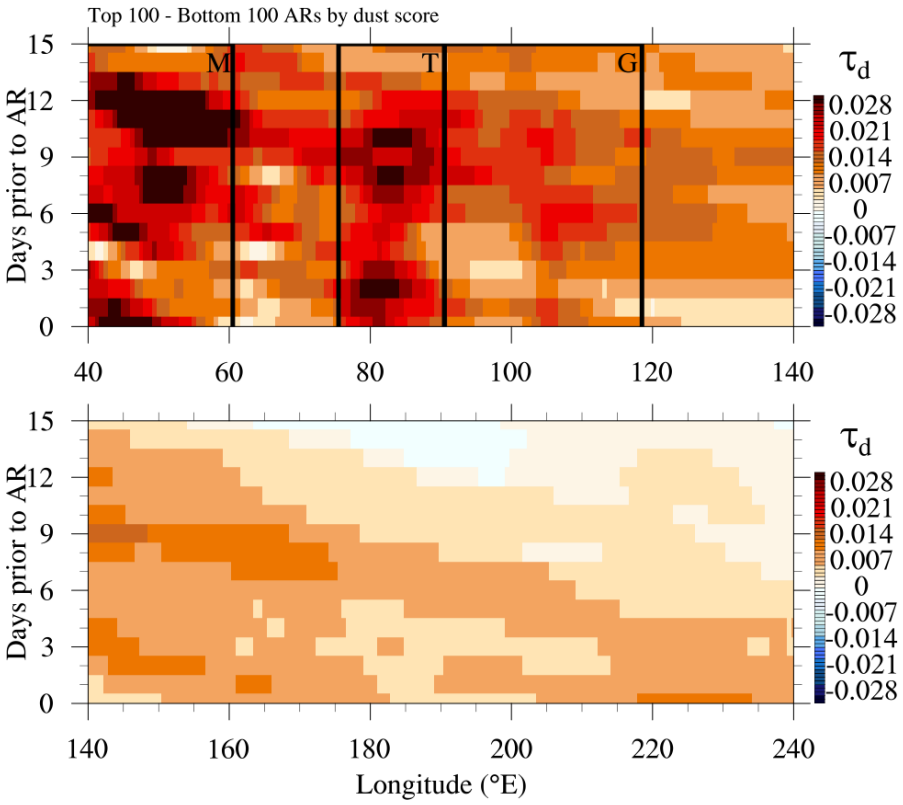

Figure 4.6: Difference of figures 4.4 and 4.5 for $\tau_{d,M}$.

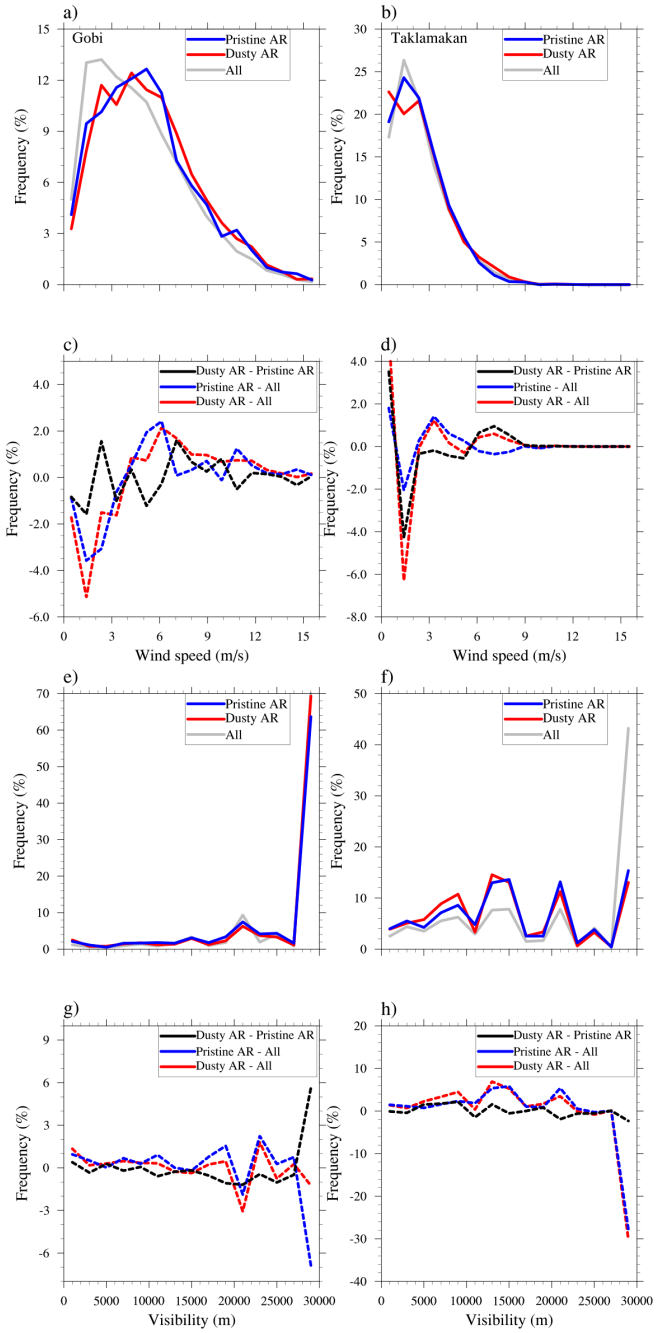

Figure 4.7: Probability Density Function (PDF) of aggregated 3-hourly a-b) wind speed (ms^{-1}) and e-f) visibility (m) measurements between 2001 and 2018 for subsets of all February-April (FMA) measurements (grey), the 6 to 11 days prior to dusty ARs (red), and the 6 to 11 days prior to pristine ARs (blue) at surface stations in the a,e) Gobi and b,f) Taklamakan desert. The differences of the PDF for dusty ARs compared to all FMA measurements (red), pristine ARs compared to all FMA measurements (blue), and dusty ARs compared to pristine ARs (black) are shown for c) winds speed over the Gobi desert, d) wind speed over the Taklamakan desert, e) visibility over the Gobi desert, and f) visibility over the Taklamakan desert.

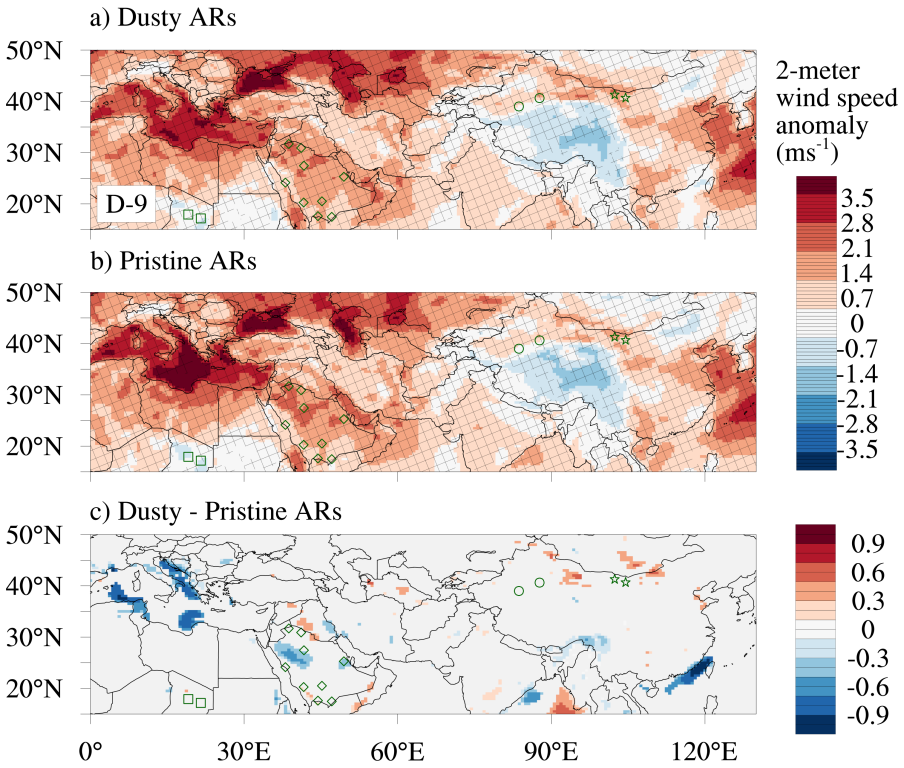

Figure 4.8: Composite of 2-meter wind speed (shaded contours; m s^{-1}) for 9-days prior to a) dusty ARs and b) pristine ARs, and c) the differences of dusty and pristine ARs. The location of ground stations in the Taklamakan desert, Gobi desert, Saudia Arabia, and Chad are shown with circles, stars, diamonds, and squares, respectively. Hatching in a) and b) indicates wind speed anomalies that are significant at 90% confidence. Only differences that are significant at 95% confidence are shaded in panel c.

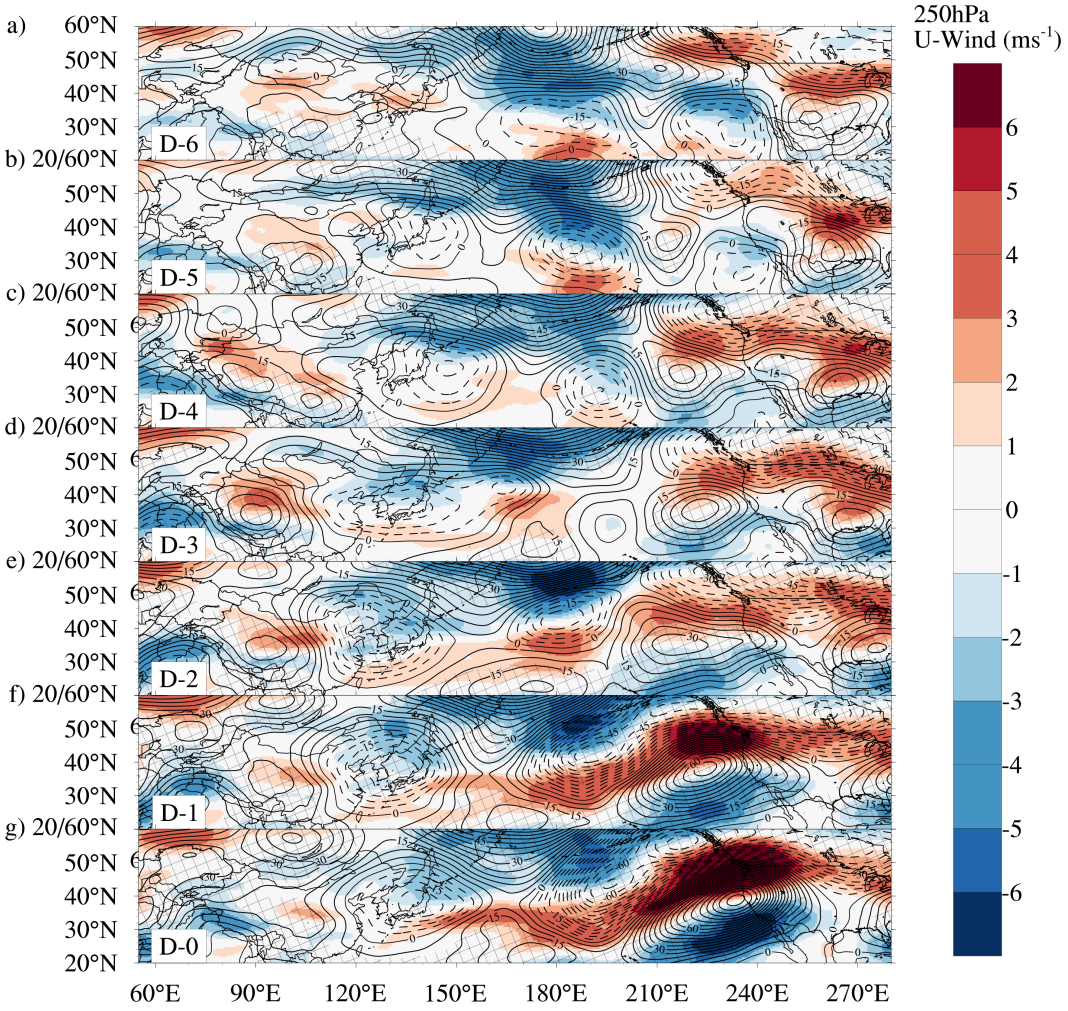

Figure 4.9: Composite of 250-hPa zonal winds (shaded contours; m s^{-1}) and 250-hPa geo-potential height (line contours; m) anomalies for days prior (a-f) and day of (g) dusty ARs. Negative geo-potential height anomalies are shown with a dashed line while positive anomalies are shown with a solid line. Hatching indicates geo-potential height anomalies that are significant at 90% confidence.

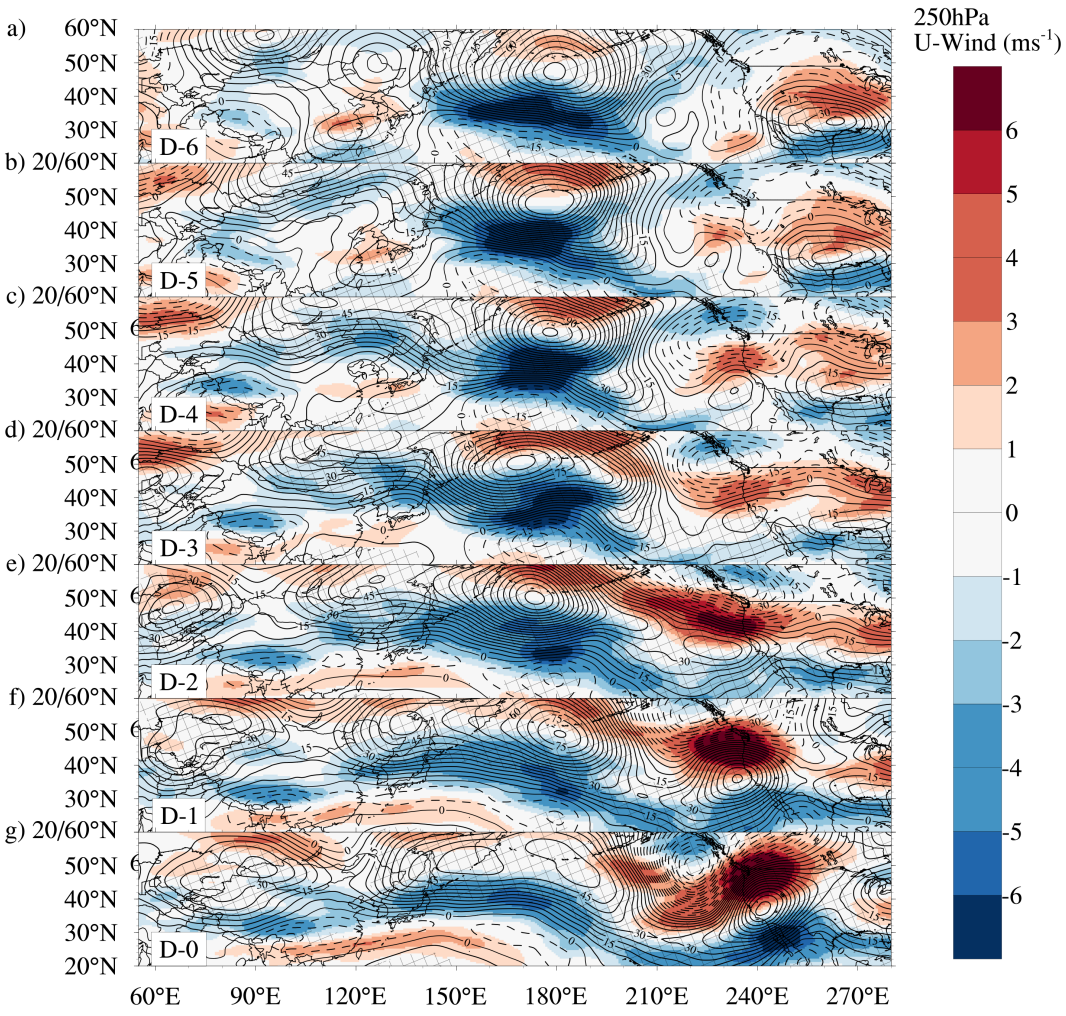

Figure 4.10: Same as Fig 4.9 but for pristine ARs.

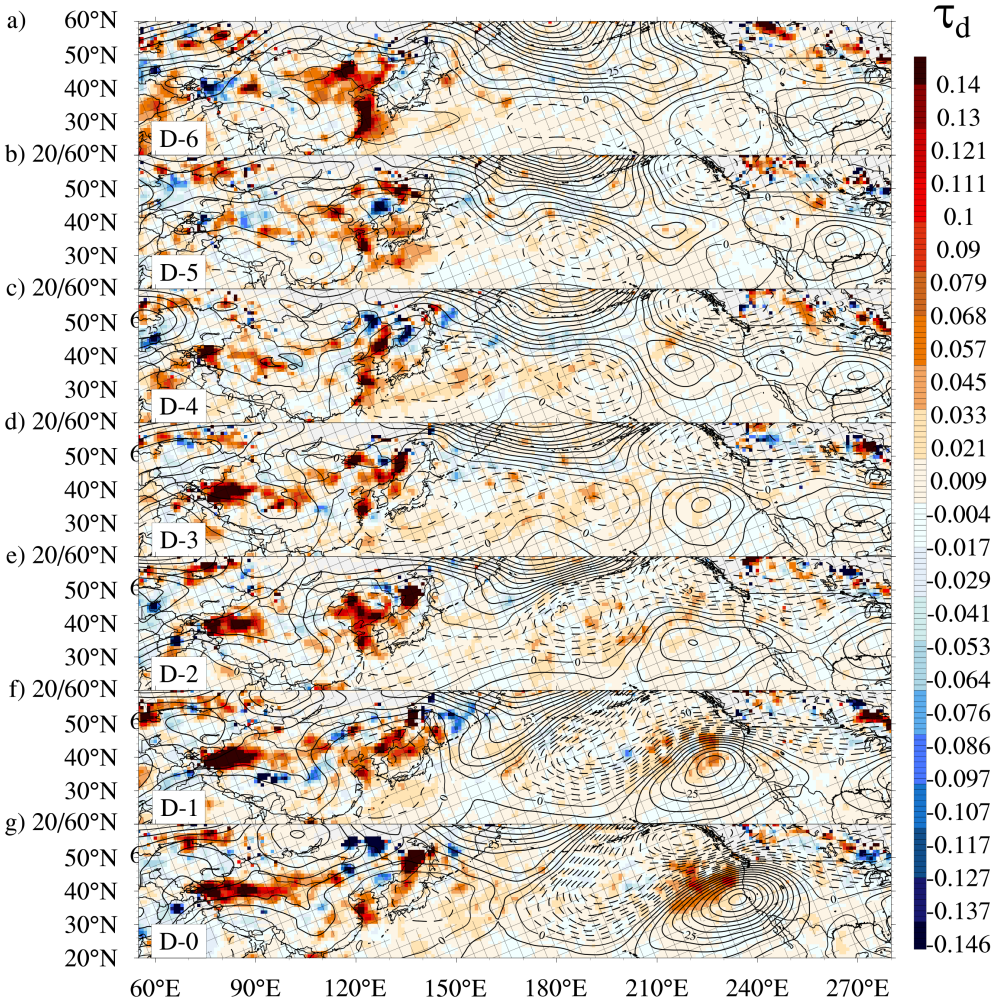

Figure 4.11: Composite of dust aerosol optical depth (τ_d; shaded contours) difference between days leading up to dusty and pristine ARs and 250-hPa geo-potential height (line contours; m) anomalies for days prior (a-f) and day of (g) dusty ARs. A nine-point local smoothing filter has been applied to the τ_d field. Negative geo-potential height anomalies are shown with a dashed line while positive anomalies are shown with a solid line. Hatching indicates geo-potential height anomalies that are significant at 90% confidence.

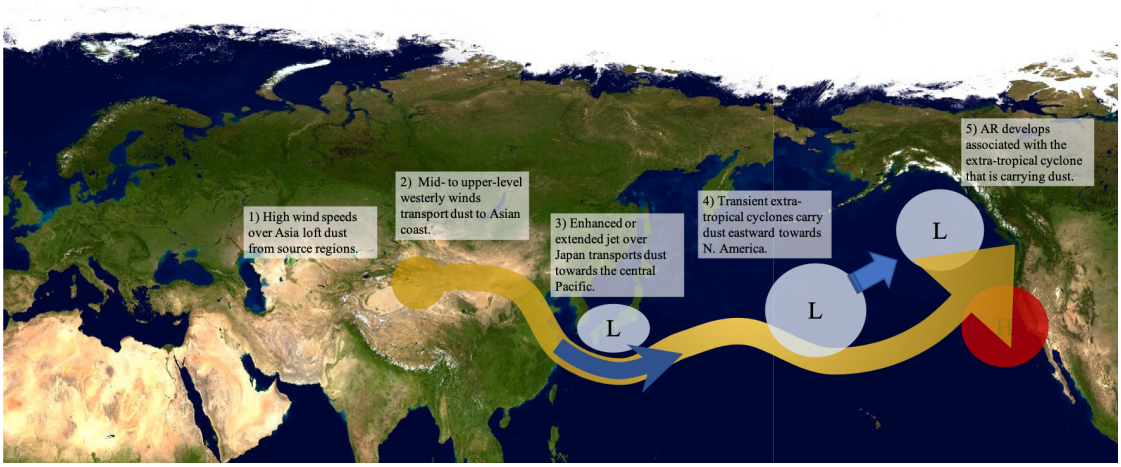

Figure 4.12: Conceptual model of the development of a dusty AR. The mustard yellow meandering arrow represents transported dust. The blue and red circles represent high and low mid- and upper-level geo-potential heights, respectively, and the broken blue arrows indicate the direction of movement of the trough. The blue solid arrow represents the North Pacific Jet.

Chapter 5

Conclusions

5.0.1 Summary of major contributions

In this dissertation, satellite retrievals, observations, and model output were used to understand the frequency, characteristics, and drivers of dust in the vicinity of Atmospheric Rivers (AR). This work addresses existing gaps in the tools available for researching dust, and in our understanding of the dust cycle.

In Chapter II, three global datasets of dust aerosol optical depth (τ_d) were developed from a simple algorithm and observation-based data. These estimates are rooted in observations of optical characteristics of the aerosol column from satellite retrievals. Daily dust estimates between 2001 and 2018 (τ_d^M) were derived from the Moderate Resolution Imaging Spectroradiometer. Monthly dust estimates between 1981 and 2018 (τ_d^A) were derived from the Advanced Very High Resolution Radiometer (AVHRR). The long-term mean global τ_d^M over the ocean was found to be 0.03 ± 0.06. While there are few measurements of dust aerosol for comparison, τ_d^M over land was found to compare well with ground-based measurements of dust from the Inter-agency Monitoring of Protected Visual Environments (IMPROVE) network in the western United States and τ_d^M over ocean was found to compare well with independent ground-based measurements made at Ragged Point, Barbados.

The observation-based dust estimates (τ_d^M) described in chapter II, allowed for the development of an AR dust score climatology, presented in chapter III. This AR dust score climatology represents a new tool tool to investigate the characteristics

and frequency of ARs in dusty environments. The mean dust score for the water-years 2002 to 2018 was found to be $0.026 \pm 0.004\sigma$. It was shown that there is a distinct seasonal cycle for ARs in dusty environments, with the highest dust score events occurring in March, due to the confluence of the end of the AR season and the beginning of the trans-Pacific dust season. In chapter II, it was also shown that dust is present primarily in the warm sector of AR-associated extra-tropical cyclones but is also enhanced in the cold sector. From a decomposition of the sources of year-to-year variability of the dust score, it was found that the correlated seasonal changes in τ_d and AR feature contribute 13% to the variance in dust score. While the contribution from independent changes in the frequency and position of ARs is small (5%), the contribution from independent changes in τ_d is much larger (40%). The contribution to the variance from correlated changes in τ_d with AR position and frequency are also large (41%), which may indicate a dynamical relationship between dust and ARs. This provided the motivation for an investigation into the meteorological conditions that lead to dusty ARs in chapter IV.

In Chapter IV, an 18-year record of dust score for Atmospheric Rivers (ARs) that made landfall along the U.S. west coast was used to investigate the conditions that enhance the dust content of the environment surrounding the AR. It was found that dusty ARs are associated with long-range transport of dust across the Pacific Ocean. While dust emission over source regions in Asia appears to be favored in the week prior to AR landfall, our results suggest that dust emission over these same source regions is also favored for pristine ARs, suggesting that there are other factors that determine whether that dust reaches the vicinity of an AR. The synoptic conditions associated with dusty ARs, as opposed to pristine ARs, indicate that the large- and synoptic-scale meteorology over the north Pacific is a major factor in the dustiness of AR surroundings. These conditions include enhanced upper and mid-tropospheric westerly winds over dust sources in northern China, an extended jet over Japan, and eastward propagating extra-tropical cyclones moving from the western and central Pacific towards North America.

5.0.2 Remaining questions

This research improves our understanding of how often and why dust is present in the vicinity of an AR. Many questions remain regarding the relationship between dust and ARs. The dust estimates presented in chapter II and the AR dust score presented in chapter III cannot directly prove dust provenance. Therefore, while our findings and previous literature suggest that Asian deserts are a major contributor and other, e.g. African or Middle Eastern, sources contribute some amount to dust in ARs (Ault et al., 2011; Creamean et al., 2013), we do not have a quantitative understanding of the contributions from different sources. Further, because our satellite-derived dust estimates can only be made for cloud-free pixels we cannot directly observe dust within cloudy regions of an AR. Therefore, the questions remains "Where is dust present in an AR, and does this change throughout the life cycle of the AR?".

Our analysis of the meteorological conditions associated with dusty ARs, in chapter IV, yielded evidence that the dust content of the environment surrounding an AR is linked to specific patterns in synoptic-scale circulation. As these patterns are linked to climate modes which are connected, in turn, to different types of ARs it would be interesting to investigate the relationship between the dust score and climate modes. This could yield additional predictability for these events. Such an analysis could be done by comparing the dust score to principle component time series of AR modes as presented in Guirguis et al. (2018).

Finally, while case studies have indicated that dust may enhance ice formation in ARs and increase precipitation (Ault et al., 2011; Creamean et al., 2013), we still have no quantitative understanding of this process. We also do not know whether there is dependency of this effect on the location of dust within or around an AR. Additionally, while on an annual basis Asian dust has been suggested to have a substantial direct radiative effect over North America (Yu et al., 2012), the direct radiative effect of dust on the structure of an AR has not been considered in any previous study.

Bibliography

Ai, N., and K. R. Polenske, 2008: Socioeconomic impact analysis of yellow-dust storms: An approach and case study for Beijing. *Economic Systems Research*, **20 (2)**, 187–203, doi:10.1080/09535310802075364.

Alfaro-Contreras, R., J. Zhang, J. S. Reid, and S. Christopher, 2017: A study of 15-year aerosol optical thickness and direct shortwave aerosol radiative effect trends using MODIS, MISR, CALIOP and CERES. *Atmospheric Chemistry and Physics*, **17 (22)**, 13 849–13 868, doi:10.5194/acp-17-13849-2017.

American Meteorological Society, cited 2020: Cold sector. Glossary of Meterology [Available online at http://glossary.ametsoc.org/wiki/"coldsector"].

Angstrom, A., 1929: On the atmospheric transmission of sun radiation and on dust in the air. *Geogr. Ann.*, **11**, 1.

Athanasiadis, P. J., J. M. Wallace, and J. J. Wettstein, 2010: Patterns of wintertime jet stream variability and their relation to the storm tracks. *Journal of the Atmospheric Sciences*, **67 (5)**, 1361–1381, doi:10.1175/2009jas3270.1.

Ault, A. P., C. R. Williams, A. B. White, P. J. Neiman, J. M. Creamean, C. J. Gaston, F. M. Ralph, and K. A. Prather, 2011: Detection of Asian dust in California orographic precipitation. *Journal of Geophysical Research*, **116 (D16)**, doi:10.1029/2010jd015351.

Baddock, M., C. Strong, J. Leys, S. Heidenreich, E. Tews, and G. McTainsh, 2014: A visibility and total suspended dust relationship. *Atmospheric Environment*, **89**, 329–336, doi:10.1016/j.atmosenv.2014.02.038.

Bedoya, A., D. Nisperuza, D. Alegría, M. Múnera, J. L. Guerrero-Rascado, C. E. Zapata, J. F. Jiménez, E. Landulfo, and Á. Bastidas, 2016: Strong Saharan dust event detected at Lalinet LOA-UNAL station, over Medellín, Colombia by active and passive remote sensing. *EPJ Web of Conferences*, **119**, 08 006, doi:10.1051/epjconf/201611908006.

Benedetti, A., J. S. Reid, P. Knippertz, J. H. Marsham, F. D. Giuseppe, S. Rémy, S. Basart, O. Boucher, I. M. Brooks, L. Menut, L. Mona, P. Laj, G. Pappalardo, A. Wiedensohler, A. Baklanov, M. Brooks, P. R. Colarco, E. Cuevas,

A. da Silva, J. Escribano, J. Flemming, N. Huneeus, O. Jorba, S. Kazadzis, S. Kinne, T. Popp, P. K. Quinn, T. T. Sekiyama, T. Tanaka, and E. Terradellas, 2018: Status and future of numerical atmospheric aerosol prediction with a focus on data requirements. *Atmospheric Chemistry and Physics*, **18 (14)**, 10 615–10 643, doi:10.5194/acp-18-10615-2018.

Bosilovich, M. G., S. Akella, L. Coy, R. Cullather, C. Draper, R. Gelaro, R. Kovach, Q. Liu, A. Molod, P. Norris, K. Wargan, W. Chao, R. Reichle, L. Takacs, Y. Vikhliaev, S. Bloom, A. Collow, S. Firth, G. Labow, G. Partyka, S. Pawson, O. Reale, S. D. Schubert, and M. Suarez, 2015: MERRA-2: Initial evaluation of the climate, technical report series on global modeling and data assimilation. Tech. rep., National Aeronautics and Space Administration, Goddard Space Flight Center.

Bréon, F.-M., A. Vermeulen, and J. Descloitres, 2011: An evaluation of satellite aerosol products against sunphotometer measurements. *Remote Sensing of Environment*, **115 (12)**, 3102–3111, doi:10.1016/j.rse.2011.06.017.

Brown, J. K. M., 2002: Aerial dispersal of pathogens on the global and continental scales and its impact on plant disease. *Science*, **297 (5581)**, 537–541, doi:10.1126/science.1072678.

Cazorla, A., R. Bahadur, K. J. Suski, J. F. Cahill, D. Chand, B. Schmid, V. Ramanathan, and K. A. Prather, 2013: Relating aerosol absorption due to soot, organic carbon, and dust to emission sources determined from in-situ chemical measurements. *Atmospheric Chemistry and Physics*, **13 (18)**, 9337–9350, doi:10.5194/acp-13-9337-2013.

Chan, P. K., X.-P. Zhao, and A. K. Heidinger, 2013: Long-term aerosol climate data record derived from operational AVHRR satellite observations. *Dataset Papers in Geosciences*, **2013**, 1–5, doi:10.7167/2013/140791.

Chaubey, J. P., K. K. Moorthy, S. S. Babu, and V. S. Nair, 2011: The optical and physical properties of atmospheric aerosols over the Indian Antarctic stations during southern hemispheric summer of the International Polar Year 2007–2008. *Annales Geophysicae*, **29 (1)**, 109–121, doi:10.5194/angeo-29-109-2011.

Chen, C., O. Dubovik, D. K. Henze, T. Lapyonak, M. Chin, F. Ducos, P. Litvinov, X. Huang, and L. Li, 2018: Retrieval of desert dust and carbonaceous aerosol emissions over Africa from POLDER/PARASOL products generated by the GRASP algorithm. *Atmospheric Chemistry and Physics*, **18 (16)**, 12 551–12 580, doi:10.5194/acp-18-12551-2018.

Chen, G., L. D. Ziemba, D. A. Chu, K. L. Thornhill, G. L. Schuster, E. L. Winstead, G. S. Diskin, R. A. Ferrare, S. P. Burton, S. Ismail, S. A. Kooi, A. H. Omar, D. L. Slusher, M. M. Kleb, J. S. Reid, C. H. Twohy, H. Zhang, and

B. E. Anderson, 2011: Observations of Saharan dust microphysical and optical properties from the Eastern Atlantic during NAMMA airborne field campaign. *Atmospheric Chemistry and Physics*, **11 (2)**, 723–740, doi:10.5194/acp-11-723-2011.

Chen, J. L., T. Pekker, C. R. Wilson, B. D. Tapley, A. G. Kostianoy, J.-F. Cretaux, and E. S. Safarov, 2017: Long-term Caspian Sea level change. *Geophysical Research Letters*, **44 (13)**, 6993–7001, doi:10.1002/2017gl073958.

Chin, M., T. Diehl, Q. Tan, J. M. Prospero, R. A. Kahn, L. A. Remer, H. Yu, A. M. Sayer, H. Bian, I. V. Geogdzhayev, B. N. Holben, S. G. Howell, B. J. Huebert, N. C. Hsu, D. Kim, T. L. Kucsera, R. C. Levy, M. I. Mishchenko, X. Pan, P. K. Quinn, G. L. Schuster, D. G. Streets, S. A. Strode, O. Torres, and X.-P. Zhao, 2014: Multi-decadal aerosol variations from 1980 to 2009: a perspective from observations and a global model. *Atmospheric Chemistry and Physics*, **14 (7)**, 3657–3690, doi:10.5194/acp-14-3657-2014.

Corringham, T. W., F. M. Ralph, A. Gershunov, D. R. Cayan, and C. A. Talbot, 2019: Atmospheric rivers drive flood damages in the western United States. *Science Advances*, **5 (12)**, eaax4631, doi:10.1126/sciadv.aax4631.

Creamean, J. M., A. P. Ault, A. B. White, P. J. Neiman, F. M. Ralph, P. Minnis, and K. A. Prather, 2015: Impact of interannual variations in sources of insoluble aerosol species on orographic precipitation over California's central Sierra Nevada. *Atmospheric Chemistry and Physics*, **15 (11)**, 6535–6548, doi:10.5194/acp-15-6535-2015.

Creamean, J. M., J. R. Spackman, S. M. Davis, and A. B. White, 2014: Climatology of long-range transported Asian dust along the west coast of the United States. *Journal of Geophysical Research: Atmospheres*, **119 (21)**, 12,171–12,185, doi:10.1002/2014jd021694.

Creamean, J. M., A. B. White, P. Minnis, R. Palikonda, D. A. Spangenberg, and K. A. Prather, 2016: The relationships between insoluble precipitation residues, clouds, and precipitation over California's southern Sierra Nevada during winter storms. *Atmospheric Environment*, **140**, 298–310, doi:10.1016/j.atmosenv.2016.06.016.

Creamean, J. M., K. J. Suski, D. Rosenfeld, A. Cazorla, P. J. DeMott, R. C. Sullivan, A. B. White, F. M. Ralph, P. Minnis, J. M. Comstock, J. M. Tomlinson, and K. A. Prather, 2013: Dust and biological aerosols from the Sahara and Asia influence precipitation in the western U.S. *Science*, **339 (6127)**, 1572–1578, doi:10.1126/science.1227279.

DeMott, P. J., K. Sassen, M. R. Poellot, D. Baumgardner, D. C. Rogers, S. D. Brooks, A. J. Prenni, and S. M. Kreidenweis, 2003: African dust

aerosols as atmospheric ice nuclei. *Geophysical Research Letters*, **30 (14)**, doi: 10.1029/2003gl017410.

Dettinger, M. D., F. M. Ralph, T. Das, P. J. Neiman, and D. R. Cayan, 2011: Atmospheric rivers, floods and the water resources of California. *Water*, **3 (2)**, 445–478, doi:10.3390/w3020445.

Draxler, R. R., and G. Rolph, 2011: HYSPLIT (HYbrid Single-Particle Lagrangian Integrated Trajectory) Model access via NOAA ARL READY website [Available at (http://ready.arl.noaa.gov/HYSPLIT.php)]. edited, NOAA Air Resources Laboratory, Silver Springs, MD.

Dubovik, O., B. Holben, T. F. Eck, A. Smirnov, Y. J. Kaufman, M. D. King, D. Tanré, and I. Slutsker, 2002: Variability of absorption and optical properties of key aerosol types observed in worldwide locations. *Journal of the Atmospheric Sciences*, **59 (3)**, 590–608, doi:10.1175/1520-0469(2002)059¡0590:voaaop¿2.0.co;2.

Duce, R. A., C. K. Unni, B. J. Ray, J. M. Prospero, and J. T. Merrill, 1980: Long-range atmospheric transport of soil dust from Asia to the tropical North Pacific: Temporal variability. *Science*, **209 (4464)**, 1522–1524, doi: 10.1126/science.209.4464.1522.

Dunion, J. P., and C. S. Velden, 2004: The impact of the Saharan Air Layer on Atlantic tropical cyclone activity. *Bulletin of the American Meteorological Society*, **85 (3)**, 353–366, doi:10.1175/bams-85-3-353.

Eichelberger, S. J., and D. L. Hartmann, 2007: Zonal jet structure and the leading mode of variability. *Journal of Climate*, **20 (20)**, 5149–5163, doi: 10.1175/jcli4279.1.

Evan, A. T., J. Dunion, J. A. Foley, A. K. Heidinger, and C. S. Velden, 2006: New evidence for a relationship between Atlantic tropical cyclone activity and African dust outbreaks. *Geophysical Research Letters*, **33 (19)**, doi: 10.1029/2006gl026408.

Evan, A. T., C. Flamant, S. Fiedler, and O. Doherty, 2014: An analysis of aeolian dust in climate models. *Geophysical Research Letters*, **41 (16)**, 5996–6001, doi: 10.1002/2014gl060545.

Evan, A. T., and S. Mukhopadhyay, 2010: African dust over the northern tropical Atlantic: 1955–2008. *Journal of Applied Meteorology and Climatology*, **49 (11)**, 2213–2229, doi:10.1175/2010jamc2485.1.

Fan, J., L. R. Leung, P. J. DeMott, J. M. Comstock, B. Singh, D. Rosenfeld, J. M. Tomlinson, A. White, K. A. Prather, P. Minnis, J. K. Ayers, and Q. Min, 2014:

Aerosol impacts on California winter clouds and precipitation during CalWater 2011: local pollution versus long-range transported dust. *Atmospheric Chemistry and Physics*, **14 (1)**, 81–101, doi:10.5194/acp-14-81-2014.

Fish, M. A., A. M. Wilson, and F. M. Ralph, 2019: Atmospheric river families: Definition and associated synoptic conditions. *Journal of Hydrometeorology*, **20 (10)**, 2091–2108, doi:10.1175/jhm-d-18-0217.1.

Formenti, P., 2003: Chemical composition of mineral dust aerosol during the Saharan Dust Experiment (SHADE) airborne campaign in the Cape Verde region, september 2000. *Journal of Geophysical Research*, **108 (D18)**, doi:10.1029/2002jd002648.

Formenti, P., J. L. Rajot, K. Desboeufs, S. Caquineau, S. Chevaillier, S. Nava, A. Gaudichet, E. Journet, S. Triquet, S. Alfaro, M. Chiari, J. Haywood, H. Coe, and E. Highwood, 2008: Regional variability of the composition of mineral dust from western Africa: Results from the AMMA SOP0/DABEX and DODO field campaigns. *Journal of Geophysical Research*, **113**, doi:10.1029/2008jd009903.

Foster, M. J., and A. Heidinger, 2013: PATMOS-x: Results from a diurnally corrected 30-yr satellite cloud climatology. *Journal of Climate*, **26 (2)**, 414–425, doi:10.1175/jcli-d-11-00666.1.

Ge, J. M., J. P. Huang, C. P. Xu, Y. L. Qi, and H. Y. Liu, 2014: Characteristics of Taklimakan dust emission and distribution: A satellite and reanalysis field perspective. *Journal of Geophysical Research: Atmospheres*, **119 (20)**, 11,772–11,783, doi:10.1002/2014jd022280.

Gelaro, R., and Coauthors, 2017: The Modern-Era Retrospective Analysis for Research and Applications, version 2 (MERRA-2). *Journal of Climate*, **30 (14)**, 5419–5454, doi:10.1175/jcli-d-16-0758.1.

Gherboudj, I., S. N. Beegum, and H. Ghedira, 2017: Identifying natural dust source regions over the Middle East and North Africa: Estimation of dust emission potential. *Earth-Science Reviews*, **165**, 342–355, doi:10.1016/j.earscirev.2016.12.010.

Ginoux, P., 2003: Empirical TOMS index for dust aerosol: Applications to model validation and source characterization. *Journal of Geophysical Research*, **108 (D17)**, doi:10.1029/2003jd003470.

Ginoux, P., J. M. Prospero, T. E. Gill, N. C. Hsu, and M. Zhao, 2012: Global-scale attribution of anthropogenic and natural dust sources and their emission rates based on MODIS Deep Blue aerosol products. *Reviews of Geophysics*, **50 (3)**, doi:10.1029/2012rg000388.

Glantz, P., E. Nilsson, and W. von Hoyningen-Huene, 2009: Estimating a relationship between aerosol optical thickness and surface wind speed over the ocean. *Atmospheric Research*, **92 (1)**, 58–68, doi:10.1016/j.atmosres.2008.08.010.

Gong, S. L., 2003: A parameterization of sea-salt aerosol source function for sub- and super-micron particles. *Global Biogeochemical Cycles*, **17 (4)**, n/a–n/a, doi:10.1029/2003gb002079.

Griffin, D. W., 2007: Atmospheric movement of microorganisms in clouds of desert dust and implications for human health. *Clinical Microbiology Reviews*, **20 (3)**, 459–477, doi:10.1128/cmr.00039-06.

Griffin, K. S., and J. E. Martin, 2017: Synoptic features associated with temporally coherent modes of variability of the North Pacific jet stream. *Journal of Climate*, **30 (1)**, 39–54, doi:10.1175/jcli-d-15-0833.1.

Grythe, H., J. Strm, R. Krejci, P. Quinn, and A. Stohl, 2014: A review of sea-spray aerosol source functions using a large global set of sea salt aerosol concentration measurements. *Atmospheric Chemistry and Physics*, **14 (3)**, 1277–1297, doi:10.5194/acp-14-1277-2014.

Guirguis, K., A. Gershunov, R. E. S. Clemesha, T. Shulgina, A. C. Subramanian, and F. M. Ralph, 2018: Circulation drivers of atmospheric rivers at the north american west coast. *Geophysical Research Letters*, **45 (22)**, doi:10.1029/2018gl079249.

Hand, J. L., W. H. White, K. A. Gebhart, N. P. Hyslop, T. E. Gill, and B. A. Schichtel, 2016: Earlier onset of the spring fine dust season in the southwestern United States. *Geophysical Research Letters*, **43 (8)**, 4001–4009, doi:10.1002/2016gl068519.

Hart, R. E., and R. H. Grumm, 2001: Using normalized climatological anomalies to rank synoptic-scale events objectively. *Monthly Weather Review*, **129 (9)**, 2426–2442, doi:10.1175/1520-0493(2001)129¡2426:uncatr¿2.0.co;2.

Heidinger, A. K., M. J. Foster, A. Walther, and X. T. Zhao, 2014: The pathfinder atmospheres–extended AVHRR climate dataset. *Bulletin of the American Meteorological Society*, **95 (6)**, 909–922, doi:10.1175/bams-d-12-00246.1.

Heinold, B., P. Knippertz, J. H. Marsham, S. Fiedler, N. S. Dixon, K. Schepanski, B. Laurent, and I. Tegen, 2013: The role of deep convection and nocturnal low-level jets for dust emission in summertime West Africa: Estimates from convection-permitting simulations. *Journal of Geophysical Research: Atmospheres*, **118 (10)**, 4385–4400, doi:10.1002/jgrd.50402.

Holben, B., T. Eck, I. Slutsker, D. Tanré, J. Buis, A. Setzer, E. Vermote, J. Reagan, Y. Kaufman, T. Nakajima, F. Lavenu, I. Jankowiak, and A. Smirnov, 1998: AERONET—a federated instrument network and data archive for aerosol characterization. *Remote Sensing of Environment*, **66 (1)**, 1–16, doi:10.1016/s0034-4257(98)00031-5.

Holben, B. N., D. Tanré, A. Smirnov, T. F. Eck, I. Slutsker, N. Abuhassan, W. W. Newcomb, J. S. Schafer, B. Chatenet, F. Lavenu, Y. J. Kaufman, J. V. Castle, A. Setzer, B. Markham, D. Clark, R. Frouin, R. Halthore, A. Karneli, N. T. ONeill, C. Pietras, R. T. Pinker, K. Voss, and G. Zibordi, 2001: An emerging ground-based aerosol climatology: Aerosol Optical Depth from AERONET. *Journal of Geophysical Research: Atmospheres*, **106 (D11)**, 12 067–12 097, doi:10.1029/2001jd900014.

Hoose, C., and O. Mhler, 2012: Heterogeneous ice nucleation on atmospheric aerosols: a review of results from laboratory experiments. *Atmospheric Chemistry and Physics*, **12 (20)**, 9817–9854, doi:10.5194/acp-12-9817-2012.

Hosler, C. L., D. C. Jensen, and L. Goldshlak, 1957: On the aggregation of ice crystals to form snow. *Journal of Meteorology*, **14 (5)**, 415–420, doi:10.1175/1520-0469(1957)014¡0415:otaoic¿2.0.co;2.

Hsu, N. C., R. Gautam, A. M. Sayer, C. Bettenhausen, C. Li, M. J. Jeong, S.-C. Tsay, and B. N. Holben, 2012: Global and regional trends of aerosol optical depth over land and ocean using SeaWiFS measurements from 1997 to 2010. *Atmospheric Chemistry and Physics*, **12 (17)**, 8037–8053, doi:10.5194/acp-12-8037-2012.

Hsu, N. C., M.-J. Jeong, C. Bettenhausen, A. M. Sayer, R. Hansell, C. S. Seftor, J. Huang, and S.-C. Tsay, 2013: Enhanced Deep Blue aerosol retrieval algorithm: The second generation. *Journal of Geophysical Research: Atmospheres*, **118 (16)**, 9296–9315, doi:10.1002/jgrd.50712.

Hsu, N. C., J. Lee, A. M. Sayer, N. Carletta, S.-H. Chen, C. J. Tucker, B. N. Holben, and S.-C. Tsay, 2017: Retrieving near-global aerosol loading over land and ocean from AVHRR. *Journal of Geophysical Research: Atmospheres*, **122 (18)**, 9968–9989, doi:10.1002/2017jd026932.

Hsu, N. C., A. M. Sayer, C. Bettenhausen, J. Lee, R. C. Levy, S. Mattoo, L. A. Munchak, and R. Kleidman, 2014: Comparing MODIS C6 'Deep Blue ' and 'Dark Target' aerosol data. Tech. rep., NASA.

Hu, Z., J. Huang, C. Zhao, Y. Ma, Q. Jin, Y. Qian, L. R. Leung, J. Bi, and J. Ma, 2019: Trans-pacific transport and evolution of aerosols: spatiotemporal characteristics and source contributions. *Atmospheric Chemistry and Physics*, **19 (19)**, 12 709–12 730, doi:10.5194/acp-19-12709-2019.

Huang, H., G. E. Thomas, and R. G. Grainger, 2010: Relationship between wind speed and aerosol optical depth over remote ocean. *Atmospheric Chemistry and Physics*, **10 (13)**, 5943–5950, doi:10.5194/acp-10-5943-2010.

Huneeus, N., M. Schulz, Y. Balkanski, J. Griesfeller, J. Prospero, S. Kinne, S. Bauer, O. Boucher, M. Chin, F. Dentener, T. Diehl, R. Easter, D. Fillmore, S. Ghan, P. Ginoux, A. Grini, L. Horowitz, D. Koch, M. C. Krol, W. Landing, X. Liu, N. Mahowald, R. Miller, J.-J. Morcrette, G. Myhre, J. Penner, J. Perlwitz, P. Stier, T. Takemura, and C. S. Zender, 2011: Global dust model intercomparison in AeroCom phase i. *Atmospheric Chemistry and Physics*, **11 (15)**, 7781–7816, doi:10.5194/acp-11-7781-2011.

Ichoku, C., 2005: Quantitative evaluation and intercomparison of morning and afternoon Moderate Resolution Imaging Spectroradiometer (MODIS) aerosol measurements from Terra and Aqua. *Journal of Geophysical Research*, **110 (D10)**, doi:10.1029/2004jd004987.

Indoitu, R., G. Kozhoridze, M. Batyrbaeva, I. Vitkovskaya, N. Orlovsky, D. Blumberg, and L. Orlovsky, 2015: Dust emission and environmental changes in the dried bottom of the Aral Sea. *Aeolian Research*, **17**, 101–115, doi:10.1016/j.aeolia.2015.02.004.

Isono, K., M. Kombayasi, and A. Ono, 1959: The nature and origin of ice nuclei in the atmosphere. *J. Meteorol. Soc. Japan*, **37**, 211–233.

Izhitskiy, A. S., P. O. Zavialov, P. V. Sapozhnikov, G. B. Kirillin, H. P. Grossart, O. Y. Kalinina, A. K. Zalota, I. V. Goncharenko, and A. K. Kurbaniyazov, 2016: Present state of the Aral Sea: diverging physical and biological characteristics of the residual basins. *Scientific Reports*, **6 (1)**, doi:10.1038/srep23906.

Jaeglé, L., P. K. Quinn, T. S. Bates, B. Alexander, and J.-T. Lin, 2011: Global distribution of sea salt aerosols: new constraints from in situ and remote sensing observations. *Atmospheric Chemistry and Physics*, **11 (7)**, 3137–3157, doi:10.5194/acp-11-3137-2011.

Jaffe, S. C., J. E. Martin, D. J. Vimont, and D. J. Lorenz, 2011: A synoptic climatology of episodic, subseasonal retractions of the Pacific jet. *Journal of Climate*, **24 (11)**, 2846–2860, doi:10.1175/2010jcli3995.1.

Jiang, M., J. Feng, Z. Li, R. Sun, Y.-T. Hou, Y. Zhu, B. Wan, J. Guo, and M. Cribb, 2017: Potential influences of neglecting aerosol effects on the NCEP GFS precipitation forecast. *Atmospheric Chemistry and Physics*, **17 (22)**, 13 967–13 982, doi:10.5194/acp-17-13967-2017.

Kahn, R. A., M. J. Garay, D. L. Nelson, K. K. Yau, M. A. Bull, B. J. Gaitley, J. V. Martonchik, and R. C. Levy, 2007: Satellite-derived aerosol optical depth over

dark water from MISR and MODIS: Comparisons with AERONET and implications for climatological studies. *Journal of Geophysical Research*, **112 (D18)**, doi:10.1029/2006jd008175.

Kalnay, E., M. Kanamitsu, R. Kistler, W. Collins, D. Deaven, L. Gandin, M. Iredell, S. Saha, G. White, J. Woollen, Y. Zhu, A. Leetmaa, R. Reynolds, M. Chelliah, W. Ebisuzaki, W. Higgins, J. Janowiak, K. C. Mo, C. Ropelewski, J. Wang, R. Jenne, and D. Joseph, 1996: The NCEP/NCAR 40-year reanalysis project. *Bulletin of the American Meteorological Society*, **77 (3)**, 437–471, doi:10.1175/1520-0477(1996)077¡0437:tnyrp¿2.0.co;2.

Kaufman, Y. J., 2005: Dust transport and deposition observed from the Terra-Moderate Resolution Imaging Spectroradiometer (MODIS) spacecraft over the Atlantic Ocean. *Journal of Geophysical Research*, **110 (D10)**, doi:10.1029/2003jd004436.

Kaufman, Y. J., I. Koren, L. A. Remer, D. Rosenfeld, and Y. Rudich, 2005: The effect of smoke, dust, and pollution aerosol on shallow cloud development over the Atlantic Ocean. *Proceedings of the National Academy of Sciences*, **102 (32)**, 11 207–11 212, doi:10.1073/pnas.0505191102.

King, M. D., S. Platnick, W. P. Menzel, S. A. Ackerman, and P. A. Hubanks, 2013: Spatial and temporal distribution of clouds observed by MODIS onboard the Terra and Aqua satellites. *IEEE Transactions on Geoscience and Remote Sensing*, **51 (7)**, 3826–3852, doi:10.1109/tgrs.2012.2227333.

Klaver, A., P. Formenti, S. Caquineau, S. Chevaillier, P. Ausset, G. Calzolai, S. Osborne, B. Johnson, M. Harrison, and O. Dubovik, 2011: Physico-chemical and optical properties of Sahelian and Saharan mineral dust: in situ measurements during the GERBILS campaign. *Quarterly Journal of the Royal Meteorological Society*, **137 (658)**, 1193–1210, doi:10.1002/qj.889.

Kleidman, R. G., N. T. ONeill, L. A. Remer, Y. J. Kaufman, T. F. Eck, D. Tanré, O. Dubovik, and B. N. Holben, 2005: Comparison of Moderate Resolution Imaging Spectroradiometer (MODIS) and Aerosol Robotic Network (AERONET) remote-sensing retrievals of aerosol fine mode fraction over ocean. *Journal of Geophysical Research*, **110 (D22)**, doi:10.1029/2005jd005760.

Kocha, C., P. Tulet, J.-P. Lafore, and C. Flamant, 2013: The importance of the diurnal cycle of aerosol optical depth in West Africa. *Geophysical Research Letters*, **40 (4)**, 785–790, doi:10.1002/grl.50143.

Kok, J. F., 2010: A scaling theory for the size distribution of emitted dust aerosols suggests climate models underestimate the size of the global dust cycle. *Proceedings of the National Academy of Sciences*, **108 (3)**, 1016–1021, doi:10.1073/pnas.1014798108.

Kok, J. F., D. A. Ridley, Q. Zhou, R. L. Miller, C. Zhao, C. L. Heald, D. S. Ward, S. Albani, and K. Haustein, 2017: Smaller desert dust cooling effect estimated from analysis of dust size and abundance. *Nature Geoscience*, **10 (4)**, 274–278, doi:10.1038/ngeo2912.

Korolev, A., 2007: Limitations of the Wegener–Bergeron–Findeisen mechanism in the evolution of mixed-phase clouds. *Journal of the Atmospheric Sciences*, **64 (9)**, 3372–3375, doi:10.1175/jas4035.1.

Kurosaki, Y., and M. Mikami, 2007: Threshold wind speed for dust emission in east Asia and its seasonal variations. *Journal of Geophysical Research*, **112 (D17)**, doi:10.1029/2006jd007988.

Lamjiri, M. A., M. D. Dettinger, F. M. Ralph, and B. Guan, 2017: Hourly storm characteristics along the U.S. West Coast: Role of Atmospheric Rivers in extreme precipitation. *Geophysical Research Letters*, **44 (13)**, 7020–7028, doi:10.1002/2017gl074193.

Lehahn, Y., I. Koren, E. Boss, Y. Ben-Ami, and O. Altaratz, 2010: Estimating the maritime component of aerosol optical depth and its dependency on surface wind speed using satellite data. *Atmospheric Chemistry and Physics*, **10 (14)**, 6711–6720, doi:10.5194/acp-10-6711-2010.

Levy, R. C., S. Mattoo, L. A. Munchak, L. A. Remer, A. M. Sayer, F. Patadia, and N. C. Hsu, 2013: The Collection 6 MODIS aerosol products over land and ocean. *Atmospheric Measurement Techniques*, **6 (11)**, 2989–3034, doi:10.5194/amt-6-2989-2013.

Levy, R. C., S. Mattoo, V. Sawyer, Y. Shi, P. R. Colarco, A. I. Lyapustin, Y. Wang, and L. A. Remer, 2018: Exploring systematic offsets between aerosol products from the two MODIS sensors. *Atmospheric Measurement Techniques*, **11 (7)**, 4073–4092, doi:10.5194/amt-11-4073-2018.

Lynn, B. H., A. P. Khain, J. W. Bao, S. A. Michelson, T. Yuan, G. Kelman, D. Rosenfeld, J. Shpund, and N. Benmoshe, 2016: The sensitivity of hurricane Irene to aerosols and ocean coupling: Simulations with WRF spectral bin microphysics. *Journal of the Atmospheric Sciences*, **73 (2)**, 467–486, doi:10.1175/jas-d-14-0150.1.

Mahowald, N., 2011: Aerosol indirect effect on biogeochemical cycles and climate. *Science*, **334 (6057)**, 794–796, doi:10.1126/science.1207374.

Malm, W. C., J. F. Sisler, D. Huffman, R. A. Eldred, and T. A. Cahill, 1994: Spatial and seasonal trends in particle concentration and optical extinction in the United States. *Journal of Geophysical Research*, **99 (D1)**, 1347, doi:10.1029/93jd02916.

Mani, M., and R. Pillai, 2010: Impact of dust on solar photovoltaic (PV) performance: Research status, challenges and recommendations. *Renewable and Sustainable Energy Reviews*, **14 (9)**, 3124–3131, doi:10.1016/j.rser.2010.07.065.

Mårtensson, E. M., E. D. Nilsson, G. de Leeuw, L. H. Cohen, and H.-C. Hansson, 2003: Laboratory simulations and parameterization of the primary marine aerosol production. *Journal of Geophysical Research: Atmospheres*, **108 (D9)**, n/a–n/a, doi:10.1029/2002jd002263.

Martin, A. C., G. Cornwell, C. M. Beall, F. Cannon, S. Reilly, B. Schaap, D. Lucero, J. Creamean, F. M. Ralph, H. T. Mix, and K. Prather, 2019: Contrasting local and long-range-transported warm ice-nucleating particles during an atmospheric river in coastal California, USA. *Atmospheric Chemistry and Physics*, **19 (7)**, 4193–4210, doi:10.5194/acp-19-4193-2019.

Micklin, P., 1988: Desiccation of the Aral Sea: a water management disaster in the Soviet Union. *Science*, **241**, 1170–1176.

Miller, R. L., and I. Tegen, 1998: Climate response to soil dust aerosols. *Journal of Climate*, **11 (12)**, 3247–3267, doi:10.1175/1520-0442(1998)011¡3247:crtsda¿2.0.co;2.

Miller, R. L., I. Tegen, and J. Perlwitz, 2004: Surface radiative forcing by soil dust aerosols and the hydrologic cycle. *Journal of Geophysical Research: Atmospheres*, **109 (D4)**, n/a–n/a, doi:10.1029/2003jd004085.

Moorthy, K. K., and S. K. Satheesh, 2000: Characteristics of aerosols over a remote island, Minicoy in the Arabian Sea: Optical properties and retrieved size characteristics. *Quarterly Journal of the Royal Meteorological Society*, **126 (562)**, 81–109, doi:10.1002/qj.49712656205.

Mulcahy, J. P., C. D. ODowd, S. G. Jennings, and D. Ceburnis, 2008: Significant enhancement of Aerosol Optical Depth in marine air under high wind conditions. *Geophysical Research Letters*, **35 (16)**, doi:10.1029/2008gl034303.

Naud, C. M., D. J. Posselt, and S. C. van den Heever, 2016: Aerosol optical depth distribution in extratropical cyclones over the northern hemisphere oceans. *Geophysical Research Letters*, **43 (19)**, 10,504–10,511, doi:10.1002/2016gl070953.

Neiman, P. J., F. M. Ralph, G. A. Wick, J. D. Lundquist, and M. D. Dettinger, 2008: Meteorological characteristics and overland precipitation impacts of Atmospheric Rivers affecting the west coast of North America based on eight years of SSM/i satellite observations. *Journal of Hydrometeorology*, **9 (1)**, 22–47, doi:10.1175/2007jhm855.1.

Norris, J. R., and A. T. Evan, 2015: Empirical removal of artifacts from the ISCCP and PATMOS-x satellite cloud records. *Journal of Atmospheric and Oceanic Technology*, **32 (4)**, 691–702, doi:10.1175/jtech-d-14-00058.1.

Notaro, M., F. Alkolibi, E. Fadda, and F. Bakhrjy, 2013: Trajectory analysis of Saudi Arabian dust storms. *Journal of Geophysical Research: Atmospheres*, **118 (12)**, 6028–6043, doi:10.1002/jgrd.50346.

ONeill, N. T., 2003: Spectral discrimination of coarse and fine mode optical depth. *Journal of Geophysical Research*, **108 (D17)**, doi:10.1029/2002jd002975.

Pandey, S. K., V. Vinoj, K. Landu, and S. S. Babu, 2017: Declining pre-monsoon dust loading over South Asia: Signature of a changing regional climate. *Scientific Reports*, **7 (1)**, doi:10.1038/s41598-017-16338-w.

Pinsky, M., A. Khain, D. Rosenfeld, and A. Pokrovsky, 1998: Comparison of collision velocity differences of drops and graupel particles in a very turbulent cloud. *Atmospheric Research*, **49 (2)**, 99–113, doi:10.1016/s0169-8095(98)00073-8.

Prospero, J. M., 1999: Long-range transport of mineral dust in the global atmosphere: Impact of African dust on the environment of the southeastern United States. *Proceedings of the National Academy of Sciences*, **96 (7)**, 3396–3403, doi:10.1073/pnas.96.7.3396.

Prospero, J. M., 2014: Characterizing the temporal and spatial variability of African dust over the Atlantic. *Past Global Changes Magazine*, **22 (2)**, 68–69, doi:10.22498/pages.22.2.68.

Prospero, J. M., and O. L. Mayol-Bracero, 2013: Understanding the transport and impact of African dust on the Caribbean Basin. *Bulletin of the American Meteorological Society*, **94 (9)**, 1329–1337, doi:10.1175/bams-d-12-00142.1.

Prospero, J. M., and R. T. Nees, 1986: Impact of the North African drought and el Niño on mineral dust in the Barbados trade winds. *Nature*, **320 (6064)**, 735–738, doi:10.1038/320735a0.

Prospero, J. M., K. Barrett, T. Church, F. Dentener, R. A. Duce, J. N. Galloway, H. Levy, J. Moody, and P. Quinn, 1996: Atmospheric deposition of nutrients to the North Atlantic basin. *Nitrogen Cycling in the North Atlantic Ocean and its Watersheds*, Springer Netherlands, 27–73, doi:10.1007/978-94-009-1776-7_2.

Pu, B., and P. Ginoux, 2016: The impact of the Pacific Decadal Oscillation on springtime dust activity in Syria. *Atmospheric Chemistry and Physics*, **16 (21)**, 13 431–13 448, doi:10.5194/acp-16-13431-2016.

Pu, B., and P. Ginoux, 2018a: Climatic factors contributing to long-term variations in surface fine dust concentration in the United States. *Atmospheric Chemistry and Physics*, **18 (6)**, 4201–4215, doi:10.5194/acp-18-4201-2018.

Pu, B., and P. Ginoux, 2018b: How reliable are CMIP5 models in simulating Dust Optical Depth? *Atmospheric Chemistry and Physics*, **18 (16)**, 12 491–12 510, doi:10.5194/acp-18-12491-2018.

Qian, W., L. Quan, and S. Shi, 2002: Variations of the dust storm in China and its climatic control. *Journal of Climate*, **15 (10)**, 1216–1229, doi:10.1175/1520-0442(2002)015¡1216:votdsi¿2.0.co;2.

Ralph, F., M. Dettinger, A. White, D. Reynolds, D. Cayan, T. Schneider, R. Cifelli, K. Redmond, M. Anderson, F. Gherke, J. Jones, K. Mahoney, L. Johnson, S. Gutman, V. Chandrasekar, J. Lundquist, N. Molotch, L. Brekke, R. Pulwarty, J. Horel, L. Schick, A. Edman, P. Mote, J. Abatzoglou, R. Pierce, and G. Wick, 2014: A vision for future observations for western U.S. extreme precipitation and flooding. *Journal of Contemporary Water Research & Education*, **153 (1)**, 16–32, doi:10.1111/j.1936-704x.2014.03176.x.

Ralph, F. M., M. D. Dettinger, M. M. Cairns, T. J. Galarneau, and J. Eylander, 2018: Defining "Atmospheric River": How the glossary of meteorology helped resolve a debate. *Bulletin of the American Meteorological Society*, **99 (4)**, 837–839, doi:10.1175/bams-d-17-0157.1.

Ralph, F. M., P. J. Neiman, and R. Rotunno, 2005: Dropsonde observations in low-level jets over the northeastern Pacific Ocean from CALJET-1998 and PACJET-2001: Mean vertical-profile and atmospheric-river characteristics. *Monthly Weather Review*, **133 (4)**, 889–910, doi:10.1175/mwr2896.1.

Ralph, F. M., P. J. Neiman, and G. A. Wick, 2004: Satellite and CALJET aircraft observations of atmospheric rivers over the eastern North Pacific Ocean during the winter of 1997/98. *Monthly Weather Review*, **132 (7)**, 1721–1745, doi:10.1175/1520-0493(2004)132¡1721:sacaoo¿2.0.co;2.

Ralph, F. M., P. J. Neiman, G. A. Wick, S. I. Gutman, M. D. Dettinger, D. R. Cayan, and A. B. White, 2006: Flooding on California's Russian River: Role of atmospheric rivers. *Geophysical Research Letters*, **33 (13)**, doi:10.1029/2006gl026689.

Ralph, F. M., K. A. Prather, D. Cayan, J. R. Spackman, P. DeMott, M. Dettinger, C. Fairall, R. Leung, D. Rosenfeld, S. Rutledge, D. Waliser, A. B. White, J. Cordeira, A. Martin, J. Helly, and J. Intrieri, 2016: CalWater field studies designed to quantify the roles of atmospheric rivers and aerosols in modulating U.S. west coast precipitation in a changing climate. *Bulletin of the American Meteorological Society*, **97 (7)**, 1209–1228, doi:10.1175/bams-d-14-00043.1.

Ralph, F. M., S. F. Iacobellis, P. J. Neiman, J. M. Cordeira, J. R. Spackman, D. E. Waliser, G. A. Wick, A. B. White, and C. Fairall, 2017: Dropsonde observations of total integrated water vapor transport within North Pacific atmospheric rivers. *Journal of Hydrometeorology*, **18 (9)**, 2577–2596, doi:10.1175/jhm-d-17-0036.1.

Remer, L. A., S. Mattoo, R. C. Levy, A. Heidinger, R. B. Pierce, and M. Chin, 2012: Retrieving aerosol in a cloudy environment: aerosol product availability as a function of spatial resolution. *Atmospheric Measurement Techniques*, **5 (7)**, 1823–1840, doi:10.5194/amt-5-1823-2012.

Remer, L. A., R. G. Kleidman, R. C. Levy, Y. J. Kaufman, D. Tanré, S. Mattoo, J. V. Martins, C. Ichoku, I. Koren, H. Yu, and B. N. Holben, 2008: Global aerosol climatology from the MODIS satellite sensors. *Journal of Geophysical Research*, **113 (D14)**, doi:10.1029/2007jd009661.

Ridley, D. A., C. L. Heald, J. F. Kok, and C. Zhao, 2016: An observationally constrained estimate of global Dust Aerosol Optical Depth. *Atmospheric Chemistry and Physics*, **16 (23)**, 15 097–15 117, doi:10.5194/acp-16-15097-2016.

Rosenfeld, D., Y. Rudich, and R. Lahav, 2001: Desert dust suppressing precipitation: A possible desertification feedback loop. *Proceedings of the National Academy of Sciences*, **98 (11)**, 5975–5980, doi:10.1073/pnas.101122798.

Rudeva, I., and S. K. Gulev, 2007: Climatology of cyclone size characteristics and their changes during the cyclone life cycle. *Monthly Weather Review*, **135 (7)**, 2568–2587, doi:10.1175/mwr3420.1.

Rutz, J. J., W. J. Steenburgh, and F. M. Ralph, 2014: Climatological characteristics of Atmospheric Rivers and their inland penetration over the western United States. *Monthly Weather Review*, **142 (2)**, 905–921, doi:10.1175/mwr-d-13-00168.1.

Ryder, C. L., E. J. Highwood, P. D. Rosenberg, J. Trembath, J. K. Brooke, M. Bart, A. Dean, J. Crosier, J. Dorsey, H. Brindley, J. Banks, J. H. Marsham, J. B. McQuaid, H. Sodemann, and R. Washington, 2013: Optical properties of Saharan dust aerosol and contribution from the coarse mode as measured during the Fennec 2011 aircraft campaign. *Atmospheric Chemistry and Physics*, **13 (1)**, 303–325, doi:10.5194/acp-13-303-2013.

Ryder, C. L., F. Marenco, J. K. Brooke, V. Estelles, R. Cotton, P. Formenti, J. B. McQuaid, H. C. Price, D. Liu, P. Ausset, P. Rosenberg, J. W. Taylor, T. Choularton, K. Bower, H. Coe, M. Gallagher, J. Crosier, G. Lloyd, E. J. Highwood, and B. J. Murray, 2018: Coarse mode mineral dust size distributions, composition and optical properties from AER-d aircraft measurements over the tropical Eastern Atlantic. *Atmospheric Chemistry and Physics Discussions*, 1–49, doi:10.5194/acp-2018-739.

Satheesh, S. K., J. Srinivasan, and K. K. Moorthy, 2006: Contribution of sea-salt to aerosol optical depth over the Arabian Sea derived from MODIS observations. *Geophysical Research Letters*, **33 (3)**, doi:10.1029/2005gl024856.

Sato, M., J. E. Hansen, M. P. McCormick, and J. B. Pollack, 1993: Stratospheric aerosol optical depths, 1850–1990. *Journal of Geophysical Research*, **98 (D12)**, 22 987, doi:10.1029/93jd02553.

Sayer, A. M., N. C. Hsu, C. Bettenhausen, and M.-J. Jeong, 2013: Validation and uncertainty estimates for MODIS Collection 6 "deep blue" aerosol data. *Journal of Geophysical Research: Atmospheres*, **118 (14)**, 7864–7872, doi:10.1002/jgrd.50600.

Sayer, A. M., N. C. Hsu, J. Lee, N. Carletta, S.-H. Chen, and A. Smirnov, 2017: Evaluation of NASA deep blue/SOAR aerosol retrieval algorithms applied to AVHRR measurements. *Journal of Geophysical Research: Atmospheres*, **122 (18)**, 9945–9967, doi:10.1002/2017jd026934.

Schmeisser, L., E. Andrews, J. A. Ogren, P. Sheridan, A. Jefferson, S. Sharma, J. E. Kim, J. P. Sherman, M. Sorribas, I. Kalapov, T. Arsov, C. Angelov, O. L. Mayol-Bracero, C. Labuschagne, S.-W. Kim, A. Hoffer, N.-H. Lin, H.-P. Chia, M. Bergin, J. Sun, P. Liu, and H. Wu, 2017: Classifying aerosol type using in situ surface spectral aerosol optical properties. *Atmospheric Chemistry and Physics*, **17 (19)**, 12 097–12 120, doi:10.5194/acp-17-12097-2017.

Shao, Y., 2008: *Physics and Modeling of Wind Erosion*. Springer Science and Business Media.

Smirnov, A., B. N. Holben, T. F. Eck, O. Dubovik, and I. Slutsker, 2003: Effect of wind speed on columnar aerosol optical properties at Midway Island. *Journal of Geophysical Research: Atmospheres*, **108 (D24)**, n/a–n/a, doi:10.1029/2003jd003879.

Stith, J. L., V. Ramanathan, W. A. Cooper, G. C. Roberts, P. J. DeMott, G. Carmichael, C. D. Hatch, B. Adhikary, C. H. Twohy, D. C. Rogers, D. Baumgardner, A. J. Prenni, T. Campos, R. Gao, J. Anderson, and Y. Feng, 2009: An overview of aircraft observations from the Pacific Dust Experiment campaign. *Journal of Geophysical Research*, **114 (D5)**, doi:10.1029/2008jd010924.

Strong, J. D. O., G. A. Vecchi, and P. Ginoux, 2018: The climatological effect of Saharan dust on global tropical cyclones in a fully coupled GCM. *Journal of Geophysical Research: Atmospheres*, **123 (10)**, 5538–5559, doi:10.1029/2017jd027808.

Sun, J., M. Zhang, and T. Liu, 2001: Spatial and temporal characteristics of dust storms in China and its surrounding regions, 1960-1999: Relations to source area and climate. *Journal of Geophysical Research: Atmospheres*, **106 (D10)**, 10 325–10 333, doi:10.1029/2000jd900665.

Swap, R., M. Garstang, S. Greco, R. Talbot, and P. Kallberg, 1992: Saharan dust in the Amazon Basin. *Tellus B*, **44 (2)**, 133–149, doi:10.1034/j.1600-0889.1992.t01-1-00005.x.

Textor, C., and Coauthors, 2006: Analysis and quantification of the diversities of aerosol life cycles within AeroCom. *Atmospheric Chemistry and Physics*, **6 (7)**, 1777–1813, doi:10.5194/acp-6-1777-2006.

Tong, D. Q., J. X. L. Wang, T. E. Gill, H. Lei, and B. Wang, 2017: Intensified dust storm activity and valley fever infection in the southwestern United States. *Geophysical Research Letters*, **44 (9)**, 4304–4312, doi:10.1002/2017gl073524.

Toth, T. D., J. Zhang, J. R. Campbell, E. J. Hyer, J. S. Reid, Y. Shi, and D. L. Westphal, 2014: Impact of data quality and surface-to-column representativeness on the PM1 / satellite AOD relationship for the contiguous United States. *Atmospheric Chemistry and Physics*, **14 (12)**, 6049–6062, doi:10.5194/acp-14-6049-2014.

Toth, T. D., J. Zhang, J. R. Campbell, J. S. Reid, and M. A. Vaughan, 2016: Temporal variability of Aerosol Optical Thickness vertical distribution observed from CALIOP. *Journal of Geophysical Research: Atmospheres*, **121 (15)**, 9117–9139, doi:10.1002/2015jd024668.

Toth, T. D., J. Zhang, J. R. Campbell, J. S. Reid, Y. Shi, R. S. Johnson, A. Smirnov, M. A. Vaughan, and D. M. Winker, 2013: Investigating enhanced Aqua MODIS Aerosol Optical Depth retrievals over the mid-to-high latitude Southern Oceans through intercomparison with co-located CALIOP, MAN, and AERONET data sets. *Journal of Geophysical Research: Atmospheres*, **118 (10)**, 4700–4714, doi:10.1002/jgrd.50311.

Twomey, S., 1977: The influence of pollution on the shortwave albedo of clouds. *Journal of the Atmospheric Sciences*, **34 (7)**, 1149–1152, doi:10.1175/1520-0469(1977)034¡1149:tiopot¿2.0.co;2.

Uematsu, M., R. A. Duce, J. M. Prospero, L. Chen, J. T. Merrill, and R. L. McDonald, 1983: Transport of mineral aerosol from Asia over the North Pacific ocean. *Journal of Geophysical Research: Oceans*, **88 (C9)**, 5343–5352, doi:10.1029/jc088ic09p05343.

VanCuren, R. A., 2002: Asian aerosols in North America: Frequency and concentration of fine dust. *Journal of Geophysical Research*, **107 (D24)**, doi:10.1029/2002jd002204.

Voss, K. K., and A. T. Evan, 2019: A new satellite-based global climatology of dust aerosol optical depth. *Journal of Applied Meteorology and Climatology*, doi:10.1175/JAMC-D-19-0194.1.

Voss, K. K., A. T. Evan, K. A. Prather, and M. F. Ralph, In Review: Dusty atmospheric rivers: Characteristics and origins. *Journal of Climate*.

Waliser, D., and B. Guan, 2017: Extreme winds and precipitation during landfall of atmospheric rivers. *Nature Geoscience*, **10 (3)**, 179–183, doi:10.1038/ngeo2894.

Winters, A. C., D. Keyser, and L. F. Bosart, 2019: The development of the North Pacific jet phase diagram as an objective tool to monitor the state and forecast skill of the upper-tropospheric flow pattern. *Weather and Forecasting*, **34 (1)**, 199–219, doi:10.1175/waf-d-18-0106.1.

Yu, H., L. A. Remer, M. Chin, H. Bian, Q. Tan, T. Yuan, and Y. Zhang, 2012: Aerosols from overseas rival domestic emissions over north america. *Science*, **337 (6094)**, 566–569, doi:10.1126/science.1217576.

Yu, Y., O. V. Kalashnikova, M. J. Garay, and M. Notaro, 2019: Climatology of asian dust activation and transport potential based on MISR satellite observations and trajectory analysis. *Atmospheric Chemistry and Physics*, **19 (1)**, 363–378, doi:10.5194/acp-19-363-2019.

Yumimoto, K., K. Eguchi, I. Uno, T. Takemura, Z. Liu, A. Shimizu, N. Sugimoto, and K. Strawbridge, 2010: Summertime trans-Pacific transport of Asian dust. *Geophysical Research Letters*, **37 (18)**, n/a–n/a, doi:10.1029/2010gl043995.

Zábori, J., R. Krejci, A. M. L. Ekman, E. M. Mårtensson, J. Strm, G. de Leeuw, and E. D. Nilsson, 2012: Wintertime arctic ocean sea water properties and primary marine aerosol concentrations. *Atmospheric Chemistry and Physics*, **12 (21)**, 10 405–10 421, doi:10.5194/acp-12-10405-2012.

Zhang, J., and J. S. Reid, 2009: An analysis of clear sky and contextual biases using an operational over ocean MODIS aerosol product. *Geophysical Research Letters*, **36 (15)**, n/a–n/a, doi:10.1029/2009gl038723.

Zhang, Z., F. M. Ralph, and M. Zheng, 2019: The relationship between extratropical cyclone strength and atmospheric river intensity and position. *Geophysical Research Letters*, **46 (3)**, 1814–1823, doi:10.1029/2018gl079071.

Zhao, T. X.-P., P. K. Chan, and A. K. Heidinger, 2013: A global survey of the effect of cloud contamination on the aerosol optical thickness and its long-term trend derived from operational AVHRR satellite observations. *Journal of Geophysical Research: Atmospheres*, **118 (7)**, 2849–2857, doi:10.1002/jgrd.50278.

Zhao, T. X.-P., I. Laszlo, W. Guo, A. Heidinger, C. Cao, A. Jelenak, D. Tarpley, and J. Sullivan, 2008: Study of long-term trend in Aerosol Optical Thickness observed from operational AVHRR satellite instrument. *Journal of Geophysical Research*, **113 (D7)**, doi:10.1029/2007jd009061.

Zhao, T. X.-P., L. L. Stowe, A. Smirnov, D. Crosby, J. Sapper, and C. R. McClain, 2002: Development of a global validation package for satellite oceanic Aerosol Optical Thickness retrieval based on AERONET observations and its application to NOAA/NESDIS operational aerosol retrievals. *Journal of the Atmospheric Sciences*, **59 (3)**, 294–312, doi:10.1175/1520-0469(2002)059¡0294:doagvp¿2.0.co;2.

Zhao, X., and N. C. Program, 2017: NOAA Climate Data Record (CDR) of AVHRR daily and monthly Aerosol Optical Thickness (AOT) over global oceans, Version 3.0. *NOAA National Centers for Environmental Information*, doi: 10.7289/V5SB43PD.

Zhu, Y., and R. E. Newell, 1998: A proposed algorithm for moisture fluxes from atmospheric rivers. *Monthly Weather Review*, **126 (3)**, 725–735, doi:10.1175/1520-0493(1998)126¡0725:apafmf¿2.0.co;2.